16th Annual

Alberta Biomedical Engineering Conference Program and Proceedings

November 6th – 8th, 2015
Banff Park Lodge
Banff, Alberta

Alberta BME

UNIVERSITY OF CALGARY

Biomedical Engineering Graduate Program

McCaig Institute for Bone and Joint Health

LIBIN CARDIOVASCULAR INSTITUTE of Alberta

HOTCHKISS BRAIN INSTITUTE

gFORCE tracker

SCHULICH School of Engineering

CBRE

Centre for Bioengineering Research and Education

SCHULICH School of Engineering

Schulich Student Activities Fund

ZEISS

We make it visible.

Alberta Health Services

SOCIÉTÉ CANADIENNE DE BIOMÉCANIQUE.

CANADIAN SOCIETY FOR BIOMECHANICS

Zymetrix

BOSE Biomaterial & Tissue Engineering Technology Development Centre

AMIF

SCHULICH School of Engineering

Advanced Micro/nanosystems Integration Facility

16th Alberta Biomedical Engineering Conference
Banff 2015

November 6-8, 2015
Banff Park Lodge
Banff, AB

PROGRAM COMMITTEE

CONFERENCE ORGANIZERS

Co-Chairs	Michael Kallos, University of Calgary Roman Krawetz, University of Calgary Christopher Dennison, University of Alberta
Student Co-Chairs	Brooklynn Knowles, University of Alberta Maria Engel, University of Calgary Warren Xu, University of Calgary Amanda Chan, University of Calgary

ABSTRACT REVIEWERS

University of Calgary
Carolyn Anglin Steven
Boyd Brent Edwards
Richard Frayne Walter
Herzog Roman Krawetz
Marc Lebel Tannin
Schmidt Nigel Shrive

University of Alberta
Samer Adeeb
Jason Carey Christopher
Dennison
Andrew Martin
Larry Unsworth Albert Vette

University of Saskatchewan
James Johnston
Sean Maw

AHS
Doug Hill

PODIUM JUDGES

Dr. Mary K. Cowman
Dr. Martin Ehrbar

POSTER JUDGES

University of Calgary	John Bertram, Coordinator Roman Krawetz Roberto Sotero Diaz	University of Saskatchewan	James Johnston Brian Eames
		University of Alberta	Christopher Dennison
		University of Campinas	Leticia Rittner

TRAINEE VOLUNTEERS

University of Calgary	Maria Engel	Student co-chair, student organizer, undergraduate funding, AV organization, volunteer recruitment, registration package assembly
	Warren Xu	Student organizer, volunteer recruitment, social event planning, registration package assembly, registration table
	Amanda Chan	Student organizer, Great challenge, Podium session chair, registration package assembly, registration table
	Scott Sibole	Fundraising, podium session chair
	Juliana Gomez	Fundraising, registration package assembly
	Issac Calvillo	Fundraising
	Erin Hildebrandt	Podium session chair, registration package assembly
	Colin Firminger	Podium session chair
	John Sevick	Podium session chair
	Andrew Michalski	Podium session chair
	Eng Kuan Moo	Podium session chair
	Sultan Khetani	Registration table, Registration package assembly,
	Karri Betram	Registration table
	Mehdi Jamshidi	Registration table
	Brodie Ritchie	Registration table
	Michael Purdy	Registration table
	Jennifer Bhatla	Registration package assembly
	Asmaa Affan	Registration package assembly
	Niloofar Korasgani	Registration package assembly
	Daniel Marquez	Registration package assembly
	Aleen Pangka	Registration package assembly
	Russell Mcwhae	Photographer
University of Alberta	Brooklynn Knowles	Student organizer, Podium session chair, Registration Table, Registration gifts

CONFERENCE EVENT COORDINATOR

University of Calgary **Elizabeth Mullaney**

A BIG THANK YOU TO ALL OF OUR VOLUNTEERS WHO HELPED WITH THE ORGANIZATION AND PLANNING OF OUR CONFERENCE THIS YEAR!

A SPECIAL THANK YOU TO
LISA MAYER FOR HER ONGOING SUPPORT
OF THE AB BME CONFERENCE.

PROGRAM

Podium sessions are in the Summit Assiniboine room.
Poster sessions are in the Castle and Alpine Meadows rooms.
You must wear your name badge in order to access all meals and conference events (podium, poster sessions, coffee breaks).

FRIDAY

4:30 - 8:30 pm	**REGISTRATION and CHECK-IN – Banff Park Lodge Lobby**
7:30 pm	**Opening Reception – Glacier Salon** **Welcome: Dr. Christopher Dennison, University of Alberta**

SATURDAY

7:00 – 8:00 am	**BREAKFAST – Glacier Chinook**
8:00 – 8:05 am	**Welcoming Remarks – Summit Assiniboine**
8:05 – 8:45 am	**Guest Speaker #1:** **Dr. Mary K. Cowman, NYU** **Macromolecular Crowding and Cell Signaling by Hyaluronan in the Biomatrix** **Session chairs: Amanda Chan, Brooklyn Knowles**
8:45 – 9:55 am	**Student Podium Presentation Session #1** **Session Chairs: Eng Kuan Moo, Erin Hildebrandt**

Andrew Michalski	01	Effects of CT Reconstruction Convolution Kernels on Bone Quality Quantification
Alina Benischek	02	Relationship between early language abilities and the underlying neural functional language network in preschoolers
Alyssa Morin	03	Effect of Hydrodynamic Shear on Proteoglycan 4 Synthesis and Secretion by Bovine Cartilage Explants
Reza Basiri	04	Advanced Quantitative Magnetic Resonance Imaging for Temporal Lobe Epilepsy
Charles Moore	05	Investigating Intersubject Variability in Pulsed Oxygen Delivery using Adult Nasal Airway Replicas
Brooklynn Knowles	06	Towards a Helmet Assessment Metric Considering both Focal and Concussive Injury

9:55 - 11:10 am

Poster Session #1 (ODD NUMBERED POSTERS)

COFFEE/BEVERAGE BREAK

Castle and Alpine Meadows

Judges: John Bertram, Coordinator, University of Calgary; Roman Krawetz, University of Calgary; James Johnston, University of Saskatchewan; Leticia Rittner, University of Campinas

Jessica Kupper	01	Determination of In-Vivo Human Dynamic Tibiofemoral Contact Mechanics
Erin Roberts	03	Expansion of Equine Cord Blood Derived Mesenchymal Stem Cells on Microcarriers
Brooklynn Knowles	05	Towards an Accurate Impact Assessment Sensor for Helmeted Impacts
Michael Purdy	07	Dissociated Sensory Neuron Culture of Adult Rats: A Protocol Comparison
David Garrett	09	Estimating Dielectric Properties of Biological Tissues at Microwave Frequencies
Aleen Pangka	11	Functional Measures of Muscle Loading and Strength and its Relation to Bone Volume
Brodie Ritchie	13	Determining In-Vivo Human Tibiofemoral Cartilage Stiffness Mechanics using High-Speed Dual-Fluoroscopy and Magnetic Resonance Imaging
Nedaa Aljezani	15	Dissociation of Synovial Membrane in Preparation for Single Cell Sorting
Majid Nazemi	17	Accounting for spatial variation of anisotropy does not improve finite element prediction of local stiffness at the proximal tibial subchondral surface
Daniel Comaduran Marquez	19	Optimization of a Monopolar Surface EMG Current-Amplifier
Abdullah Al-Ani	21	Micro-tissue engineering for Retinal Transplants
Norden Flaaten	23	An Increased Proportion of Weakly Bound Cross-bridges Contribute to the Age-related Maintenance of Eccentric Strength
Jessica Norman	25	LONG TERM *IN VIVO* KINEMATICS OF THE OVINE STIFLE JOINT FOLLOWING ANTERIOR CRUCIATE LIGAMENT TRANSECTION
Svetlana Kuzntsova	27	In Situ Chondrocyte Viscoelasticity Following Static and Dyanmic Compressions
Jingxuan Zhao	29	Factors Affecting Cell Viability and Recovery Under Shear Stress
Niloofar Ghazavi Khorasgani	31	Increasing serum 25(OH)D improves balance after one year: Pilot results
Ryan Plett	33	Finite element bone strength at the distal radius and tibia predict vertebral yield load
Jacob Kennard	35	EFFECT OF PEG COATING ON NANOPARTICLE DIFFUSION THROUGH TUMOR EXTRACELLULAR MATRIX
Alexander Sacher	37	Validating FE-derived internal bone strain using high resolution imaging and material testing
Medhi Shekarforoush	39	Changes in the relative velocity of joint following anterior cruciate ligament transection leading to osteoarthritis in a sheep model
Shefali Pandey	41	Multicomponent T2 Analysis of Glioblastoma in a Mouse Model
Kirsten Svidal	43	Development and Validation of New CAD/CAM System for Spinal Orthosis
Bryce Besler	45	An Investigation into the Feasibility of using Microwave Imaging to Monitor Bone Health
Thomas Johnson	47	Increased cerebral metabolic rate for oxygen in a mouse model of multiple sclerosis
Seung-hun Lee	49	Does the Treatment of Organophosphate Exposure Cause Physiological Changes in the Brain? An MRI Study
Mehrdad Hosseini	51	Validating finite element strain predictions using high resolution imaging and experimental testing
Nima Ashjaee	53	Bench-Testing a Novel Surgical Implant to Stabilize Distal Radial Fractures

11:10 – 12:30 pm

Student Podium Presentation Session #2

Session Chairs: Scott Sibole, John Sevick

Colin Firminger	07	THE INFLUENCE OF SHOE TYPE AND STRIDE LENGTH ON FOREFOOT LOADING AND FOOT STRIKE ANGLE DURING RUNNING
Karri Bertram	08	Inhibiting p21 using small molecules to promote chondrogenesis in MSCs
Myles Borthwick	09	DIET INDUCED OBESITY MAY AFFECT THE FORCE-VELOCITY RELATIONSHIP IN RAT SOLEUS
Fu You	10	Preliminary Study on Cell-laden Hydrogel Constructs for Cartilage Tissue Engineering
Julie Hunchak	11	Precision of bone properties and strength estimates in children
Jaqueline Lourdes Rios	12	Does high mileage running cause knee osteoarthritis in rats?
Daniel Korchinski	13	Detection of the mitochondrial enzyme cytochrome oxidase brain of a mouse model

12:30 – 1:45 pm **LUNCH – Glacier Chinook**

1:45 – 2:30 pm **Industry Panel Speakers:**

Lita McDonald, Carl Zeiss Canada
Zak Kemp, Striker
Ben Youn, Biomarin

2:30 – 2:35 pm **BREAK – Group Pictures**

2:35 - 3:50 pm

Poster Session #2 (EVEN NUMBERED POSTERS)
COFFEE/BEVERAGE BREAK

Judges: John Bertram, Coordinator, University of Calgary, Roberto Sotero Diaz, University of Calgary; Christopher Dennison, University of Alberta, Brian Eames, University of Saskatchewan

Anita Fung	02	VERIFICATION OF MESH SIZE AND MATERIAL PROPERTY ASSIGNMENT FOR FINITE ELEMENT MODELS OF THE HUMAN SECOND METATARSAL BONE
Negar Behzadi Fard	04	Monitoring LFCN Compression during Adolescent Idiopathic Scoliosis (AIS) Surgery: Is time or pressure the critical factor?
Fraz Anjum	06	Migration and proliferation of human skin-derived precursor (hSKP) cells in enzymatically crosslinked hrybrid hydrogels
Jolene Phelps	08	Chitosan/Decellularized Cartilage Microcarriers for Chondrogenic Stimulation of Synovial Fluid Derived Mesenchymal Stem Cells
Guomin Ren	10	Serum Cytokine Profiles are Distinct between Patients with Hip or Knee Osteoarthritis and Associated with Hip Pain
Max Hamilton	12	Pipeline for an Atlas-based Analysis of Mouse Brain MRI's Obtained with a Helium Cooled RF Coil
Lindsay Loundagin	14	THE INFLUENCE OF LOADING DURATION AND LOADING CYCLES ON COMPRESSIVE FATIGUE FAILURE OF BOVINE CORTICAL BONE
Jennifer Si	16	On the Mechanical Properties of 3D-Printed Scaffolds for Cartilage Tissue Engineering
Douglas Kondro	18	3D Printing's Application to Surgical Simulation and Animal Prosthetics
Dustin Eichhorn	20	Investigation of Toe Tip Necrosis Syndrome Using Biomechanical Testing and High Resolution Imaging
Shrushrita Sharma	22	Image Analysis Of Tissue Alignment For Assessing Injury and Repair in Multiple Sclerosis
Erin Hildebrandt	24	Calgary Vitamin D Trial 12 Month Pilot Data: Increased 25(OH)D is Associated with Improved Bone Density as Measured by HR-pQCT, but not DXA
Graham Macdonald	26	METABOLIC EFFECTS OF DIET INDUCE OBESITY
Roberto Souza	28	Analysis of the Watershed Tie-zone Influence on the Skull-stripping
Henry Yu	30	Evolution of Helmet Strain Energy in Linear Impacts with Helmet Accessories
Shuyue Liu	32	Is titin responsible for force enhancement in skeletal muscle?
Asmaa Affan	34	Hip Derived Synovial Mesenchymal Progenitor Cell Surface Markers *In Vivo* as Indicators for Differentiation Potential
Runze Yang	36	Developing 9.4T MRI to detect brain tumor treatment response with immuno-stimulating therapies
Adeola Olubamiji	38	Non-invasive characterization of degradation profile of 3D-printed hybrid constructs for cartilage tissue engineering using synchrotron-radiation-inline-phase-contrast CT
Mohsen Janmaleki	40	Cell Impedance Alteration: Promising Biomarker for Monitoring Neuronal Differentiation
Sultan Khetani	42	Surface modified screen printed graphene biosensor for electrochemically diagnosing and manage Spinal Cord Injury (SCI)
Mehdi Jamshidi	44	Evaluation mechanical properties of the bioabsorbable polymers as a material in designing flow-diverter stent

Amir Hamedzadeh	46	Damage Model for Biological Tissues
Matthew McDonald	48	Developing a Model to Predict Distal Radius Fracture During a Fall
Ryan Schoeder	50	Inertial sensors as a diagnostic tool: Biomedical engineering support of the 2015-16 veterinary independent research project
Leah Allen	52	Enhanced Chondrogenic Phenotype of Tissue Engineered Cartilage Constructs Generated in Stirred Suspension Bioreactors
Lei Lu	54	Controlled release of dexamethasone from in situ forming sulfobutyl ether β-cyclodextrin/self-assembling peptide hydrogel

3:50 – 5:10 pm **Student Podium Presentation Session #3**

Session Chairs: Colin Firminger, Andrew Michalski

Jennifer Bhatla	14	CaMos Youth Cohort 3D Image Registration
Craig Martis	15	Titin Hysteresis and Elasticity in Actively Stretched Muscle Myofibrils
Juliana Gomez	16	Nanoparticle localization in angiogenic vessels to regions of disturbed flow
Nabeela Nathoo	17	Hypoxia and reduced cerebral blood flow in multiple sclerosis are detected using combined MRI and near-infrared spectroscopy
Abhilash Hareendranathan	18	Machine Learning based Classification of Acetabular Shape for Diagnosis of Infant Hip Dysplasia (DDH) from 3DUS
Thomas Zhang	19	DISTAL AND PROXIMAL FASCICLE LENGTH CHANGES IN ACTIVE AND PASSIVE HUMAN GASTROCNEMIUS MEDIALIS MUSCLE
Ashley Dalrymple	20	Development of an Intraspinal Microstimulation Controller to Restore Walking after a Hemisection Spinal Cord Injury

6:00 – 7:00 pm **DINNER – Glacier Chinook**

7:00 pm **"THE GREAT CHALLENGE"**

8:00 pm **Social – Elk and Oarsman**
119 Banff Avenue (2nd Floor, Above The Ski Hub)

SUNDAY

7:15 – 8:15 am		**BREAKFAST – Glacier Chinook**
8:15 – 8:45 am		**Checkout**
8:45 – 9:25 am		**Guest Speaker #2: –** **Dr. Martin Ehrbar,** **University Hospital Zürich** **Cell-Instructive Hydrogels for 3D Tissue Models and Tissue Regeneration** **Session Chairs: Warren Xu, Erin Hildebrandt**
9:25 – 10:20 am		**Student Podium Presentation Session #4** Session Chairs: **Brooklynn Knowles, Eng Kuan Moo**
Christopher Duszynski	21	**Using frequency domain near-infrared spectroscopy to measure resting state functional activity**
Yang Yu	22	CHARACTERIAZING AND OPTIMIZING PSEUDOISLETS
Hanieh Arjmand	23	Evaluation of two transfixation cast constructs in horse forelimbs using finite element modeling
Johnathan Sevick	24	Biomechanical Effects of Re-Injury in a Rabbit Medial Collateral Ligament Model
Ehsan Shahrabi Farahani	25	Improving the Accuracy of fMRI Optical Neuritis Markers
10:20-10:40 am		**Poster Session #3 (FINALISTS ONLY)** **COFFEE/BEVERAGE BREAK; Activity from BMEG** **Judges**: John Bertram, Judge Coordinator, University of Calgary; Roman Krawetz, Roberto Sotero Diaz, University of Calgary; Christopher Dennison, University of Alberta; Leticia Rittner, University of Campinas; James Johnston, Brian Eames, University of Saskatchewan
10:40 – 11:35 am		**Student Podium Presentation Session #5** **Session Chairs: Scott Sibole, Amanda Chan**
Andres Kroker	26	A new method for quantitative assessment of the knee using high resolution peripheral quantitative computed tomography
Christopher O'Neill	27	Diffuse Grey Matter Susceptibility Changes for Detecting Smaller Microbleeds in Cerebral Amyloid Angiopathy
Kotaybah Hashlamoun	28	Fast Computational Scheme for Biological Tissues with Statistical Fibre Orientation
Christina Jablonski	29	Spontaneous articular cartilage regeneration after injury in p21 null mice
Raveena Dhaliwal	30	9.4T MRI Characterization of Experimental Demyelination and Remyelination of Mouse Spinal Cord Induced by Focal Injection of Lysolecithin

FINAL AWARD PRESENTATIONS

11:45 – 12:30 pm	**Final Award Presentations**
CLOSING REMARKS	**Amanda Chan, Warren Xu**

REMINDER :
Please return all name tags and judges' clipboards at end of conference.

We thank you for your cooperation.

THANK YOU EVERYONE!
WE HOPE YOU ENJOYED OUR EVENT!

MAP

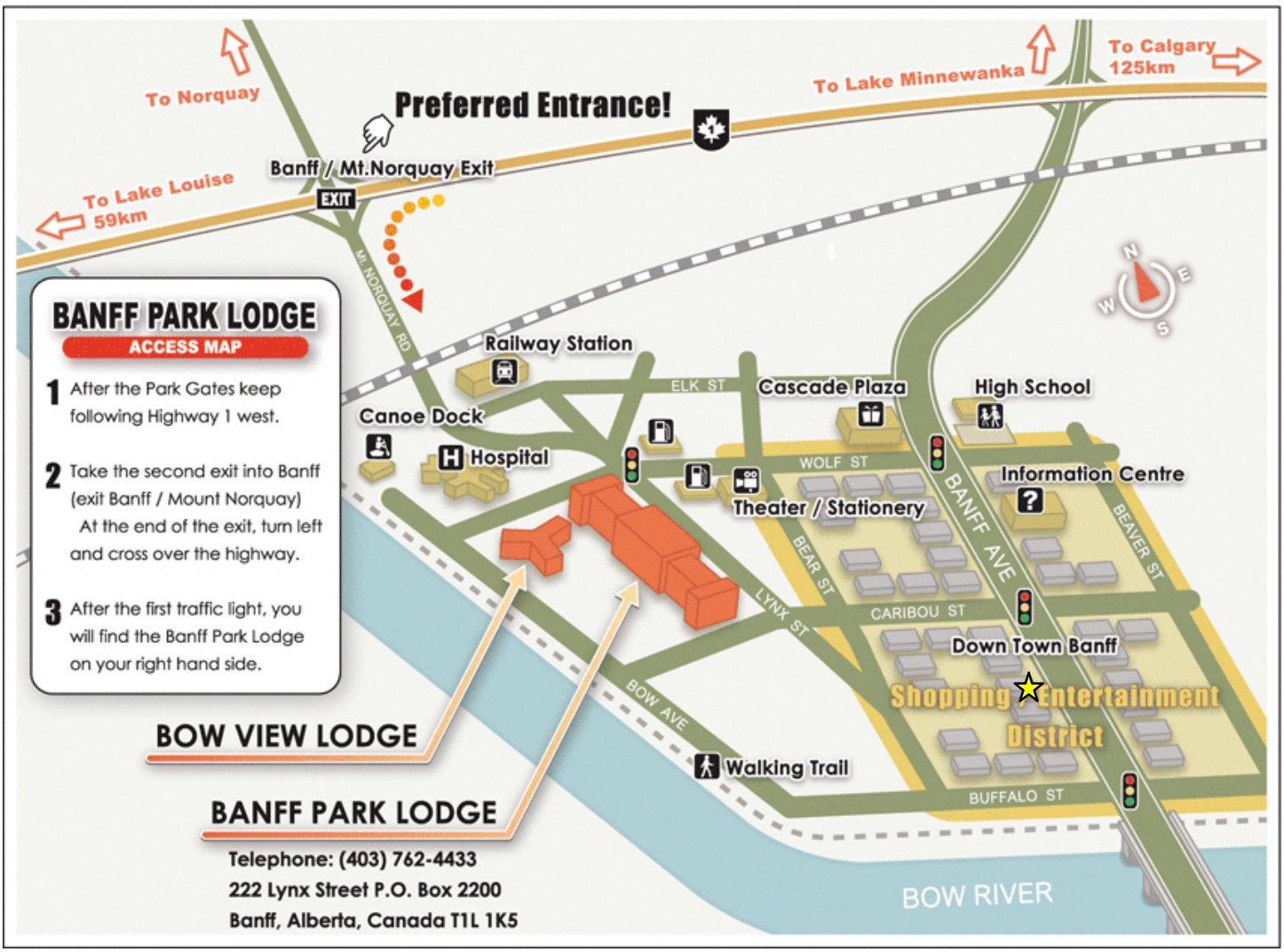

For Saturday night, the Elk and Oarsman (☆) is at 119 Banff Avenue (2nd Floor, Above The Ski Hub), just a few blocks from the hotel.

Directions – Walk to the right out of the main hotel entrance.

Turn left onto Caribou Street (first street).

Walk up to Banff Avenue (main street).

Turn right on Banff Ave until you see the Elk and Oarsman on your right (entrance is right next to Lululemon).

Please note: the Elk and Oarsman is on the second floor.

Biosketch

Dr. Mary K. Cowman received her Ph.D. in Chemistry at Case Western Reserve University. She did postdoctoral work in the Department of Biochemistry at Brandeis University and was an NIH Postdoctoral Fellow in the Department of Ophthalmology of the Columbia University College of Physicians and Surgeons. She continued there as a Research Associate faculty member for two years. Since 1982 she has been on the faculty of the Polytechnic School of Engineering of New York University, and was the recipient of the Distinguished Teacher Award in 2006. Dr. Cowman's scientific research is focused on the determination of structure, function, and medical properties of biomaterials, with special expertise in the extracellular matrix polysaccharide hyaluronan. She is a Founding Member and current President-Elect of the International Society for Hyaluronan Sciences. She holds three patents and has three pending patent applications for biomaterials, biotherapeutics, and diagnostic assays based on hyaluronan.

Macromolecular Crowding and Cell Signaling by Hyaluronan in the Biomatrix

The glycosaminoglycan hyaluronan (HA) is a key component of the microenvironment surrounding cells. In healthy tissues, HA molecules have extremely high molecular weight, and large hydrodynamic volumes. Tethered to the cell surface by receptor proteins, HA molecules crowd each other, as well as other macromolecular species.

This leads to severe non-ideality in physical properties of the biomatrix, because steric exclusion leads to an increase in effective concentration. In the Matsuoka and Cowman model for mutual crowding of polymers, the excluded volume depends on polymer concentration and hydrodynamic volume. For a high molecular weight species like HA, it leads to a viscoelastic medium with a high colloid osmotic pressure. Mechanical properties of the extracellular matrix, tissue hydration, and receptor-ligand interactions are strongly affected by the presence of HA.

In inflammation, reactive oxygen and nitrogen species fragment the HA chains. Depending on the rate of chain degradation relative to the rates of new synthesis and removal of damaged chains, short fragments of the HA molecules can be present at significant levels. Not only are the physical properties of the extracellular matrix affected, but the HA fragments act as endogenous danger signals. Analysis of the extent of HA fragmentation can be utilized in medical diagnostic tests. In addition, control of receptor interactions with HA fragments is leading to new therapeutic approaches to wound healing and cartilage repair without fibrosis.

Curriculum Vitae Dr. sc. nat. Martin Ehrbar

Affiliation: Department of Obstetrics
University Hospital Zürich
Schmelzbergstrasse 12,
8091 Zürich

E-mail: martin.ehrbar@usz.ch

Homepage: www.ehrbarlab.comScientific Career

07/09-present Head of Research, Department of Obstetrics, University Hospital Zurich, Zurich, Switzerland 07/07-07/09 Group Leader, Department of Cranio-Maxillofacial Surgery, University Hospital Zurich, Zurich,

Switzerland

07/04-06/06 Postdoc, Department of Cranio-Maxillofacial Surgery, University Hospital Zurich, Zurich, Switzerland

08/00-06/04 Ph.D. ETHZ, Institute for Biomedical Engineering, Department of Materials, Zurich, Switzerland 10/93-04/98 Diploma in Biology, ETHZ, Zurich, Switzerland

Honors

2004 Young Investigator Award, Keystone Symposium: Angiogenesis novel basic science insights and human therapy
2004 Young Investigator Awards, Biennial Meeting of the International Society for Applied Cardiovascular Biology (ISACB)

Research Interests

Matrix Engineering, Cell-Matrix Interactions, Growth Factor Delivery, Hydrogel Patterning, in vitro 3D Tissue Models, Fetal Membrane Repair, Bone Healing, Angiogenesis, Tissue Sealants, Stent-Blood Interactions, Adult Human Stem Cells

Abstract: Cell-Instructive Hydrogels for 3D Tissue Models and Tissue Regeneration

Defective or missing tissues, caused by inherent diseases, trauma or cancer, can have cosmetic to life threatening consequences for an affected patient. The ability to re-establish tissue structure and function(s) can be a significant achievement towards the treatment of large number of patients. A more thorough understanding of the dynamics of healthy, diseased and healing tissues will allow designing and engineering of next generation healing strategies or engineered tissues.
I intend to give a short introduction into tissue healing and discuss biological functions, which could be employed to modulate healing processes. I will present rationally designed biomaterials platforms, which can be tailored towards specific applications by tuning physical and biological properties. I will give examples of novel biomaterials as well as additive or preventive manufacturing strategies based three-dimensional tissue models. Finally I will show how this research can be employed to develop next generation tissue healing implants for bone, blood vessels, and fetal membranes.

INDUSTRY PANELIST PROFILE

Lita McDonald Profile

Lita has been the Account Manager for Carl Zeiss Microscopy in Alberta since 2012 and has been working in the microscopy industry since 2007. Lita didn't start out with a career in microscopy sales and support in mind, she had originally intended to take over her family's farm in central Alberta and raise purebred beef cattle after completing her BSc (Hon) in Molecular Genetics at the University of Alberta. With the collapse of beef prices in 2003 and the general high costs and low financial returns of farming, Lita decided to continue in academia and moved to Ottawa where she completed her MSc in Human and Medical Genetics at the University of Ottawa in 2006. From there she returned to Alberta, joining the Live Cell Imaging Facility at the University of Calgary then taking a position with Olympus Canada Inc in microscopy sales 2007 and moving to Edmonton yet again. Lita's background in cell and molecular biology from her formal education, exposure to mechanical systems and electronics as well as raising and selling purebred cattle on her family's farm have allowed her to succeed in her current role at Zeiss.

Carl Zeiss Canada Ltd Company Profile

Carl Zeiss Canada Ltd. was founded in 1963 with the scientific division selling and servicing, laboratory and surgical microscopes, and related products. Our National Headquarters is located in Toronto, Ontario, with over 80 sales and service staff servicing the country from coast-to- coast. In 1979, the optical division was added supplying lenses and eye glasses to the Canadian market. By 1992, the optical division had grown into a full service optical lab with lens surfacing and coating capabilities. With continued growth and customer support Carl Zeiss Canada continues to expand. In 2002, Carl Zeiss Canada expanded further by reintroducing the Carl Zeiss Meditec lines of surgical and ophthalmic equipment to its medical sales and service group.
Locally, our business units include Medical Systems, and Microscopy including Electron/Ion Microscopes, Vision Care (spectacle lens) and Sport Optics (binoculars, rifle and spotting scopes).

Biography:

Ben obtained his B.A.Sc. and M.A.Sc. in Chemical Engineering at the University of Waterloo, and his Ph.D. in Chemical Engineering at the University of Calgary. During his doctoral studies, he developed bioreactor processes for the expansion of mammary epithelial stem cells and breast cancer stem cells, which were recognized as one of the top 50 Canadian scientific and engineering discoveries in 2006 by NSERC. Upon graduating from U of C in 2008, he moved to San Francisco to find work as a cell culture scientist. Several months later, he was hired by BioMarin Pharmaceutical Inc. to pursue the career he's always dreamed of. Ben is still at BioMarin and is a Senior Scientist whose research now focuses on understanding the impact of large scale perfusion processes on the safety and efficacy of therapeutic enzymes used to treat children afflicted with rare genetic disorders.

Company Profile:

BioMarin is a world leader in providing therapies to treat patients with rare diseases. We have five products available to patients and one of the most diverse and exciting product pipelines in our industry. True to our origins as pioneers almost two decades ago, we continue to blaze scientific trails on behalf of children and adults with rare genetic diseases. Our clinical and commercial programs are supported by BioMarin's world-class manufacturing capabilities. We continue to build our manufacturing capacity both to meet the demand for our commercial products and the products in clinical trials. Due to our success and rapid growth, we are a very different company from what we were many years ago, yet we have remained true to our core – to make a big difference for small patient populations. We still know many of our patients by name and regularly spend time with them at patient gatherings or at events on our campus. We continue to be inspired by strong science, and when we see opportunities where the biology of the disease is well understood, we take calculated risks. The patients and families that we serve are extraordinary, and we appreciate their participation in the clinical trials required to provide approved treatments. The optimism, resiliency and thoughtfulness of our patients motivate us to deliver breakthrough therapies that will change the course of genetic diseases.

INDUSTRY PANELIST PROFILE

Zak Kemp
Associate Director of Procedural Innovation. Stryker Corporation
Kalamazoo, Michigan

Zak is a 17 year veteran of Stryker, prior to his current role in Procedural Innovation he held roles in Sales, Sales Management, Sales Training, Marketing and Advanced Product Development. Stryker is one of the world's leading technology companies in the medical Device space offering a variety of products ranging from: Robotics, Implants for Orthpedic, Spine and Cranialfacial procedures, Surgical Video, Biologics, Ultrasonics, Power tools, Sustainability Solutions, Communications, Surgical Navigation, as well as a wide selection of hospital Beds, Stretchers and Cots. Stryker has over 26,000 employees worldw ide offering Research and Development opportunities in over 10 countries and providing products to more than 100 countries worldwide.

ANNUAL SPONSORS

University of Calgary, Biomedical Graduate Program

University of Calgary, Centre for Bioengineering Research and Education

GOLD Level Sponsors
McCaig Institute

SILVER Level Sponsors
GForceTracker
Hotchkiss Brain Institute
Libin Cardiovascular Institute

BRONZE Level Sponsors
AMIF
Carl Zeiss Canada
Canadian Society for Biomechanics
Glenrose, AHS
Zymetrix

THANK YOU TO ALL OF OUR SPONSORS.
YOUR SUPPORT MAKES ALL THE DIFFERENCE!

McCaig Institute for Bone and Joint Health, Gold Sponsor

A healthy bone and joint system keeps us mobile, and thus plays a pivotal role in maintaining our overall health and well-being. The McCaig Institute is home to a multidisciplinary team of basic scientists, engineers, clinicians and health systems researchers from six faculties at the University of Calgary and four from the University of Alberta. These researchers have established high-level research programs to enhance the diagnosis, treatment and prevention of bone and joint conditions, in order to keep people moving. Much of the research is focused on osteoarthritis, rheumatoid arthritis and osteoporosis as these conditions pose some of the greatest threats to bone and joint health and rob people of their mobility and ability to live independently. The Institute is a pioneer in the multidisciplinary approach to tackling these critical conditions. Team members combine their diverse expertise to investigate questions related to all aspects of bone and joint health, from molecules to cells, to tissues, to joints, to patients, clinical populations and the way that healthcare is delivered.

McCaig Institute
for Bone and Joint Health

Institute members were recently successful in an application to the Canada Foundation for Innovation, raising a total of over $13 million to establish the Mobility and Joint Health Clinical Facility. This facility will create a unique capability in the province, to facilitate and accelerate the application of research findings into practice far more quickly than occurs currently (11 to 17 years). As shown in the figure, the McCaig Institute will be the research component of a triumvirate of units in the province related to bone and joint health. The clinical research facility completes the translation pipeline to enable the three units to work together seamlessly on bone and joint health issues. Members of the Strategic Clinical Network of Alberta Health Services will identify problems which need solutions: these will be conveyed to members of the McCaig Institute who will work together to formulate a solution – some problems will be short term and others involve much longer term research. The solution will be assessed by the independent Alberta Bone and Joint Health Institute, implemented by the network in a pilot fashion and assessed for efficacy, again by ABJHI. This will enable evidence-based best practice to be implemented across the network to the benefit of all Albertans.

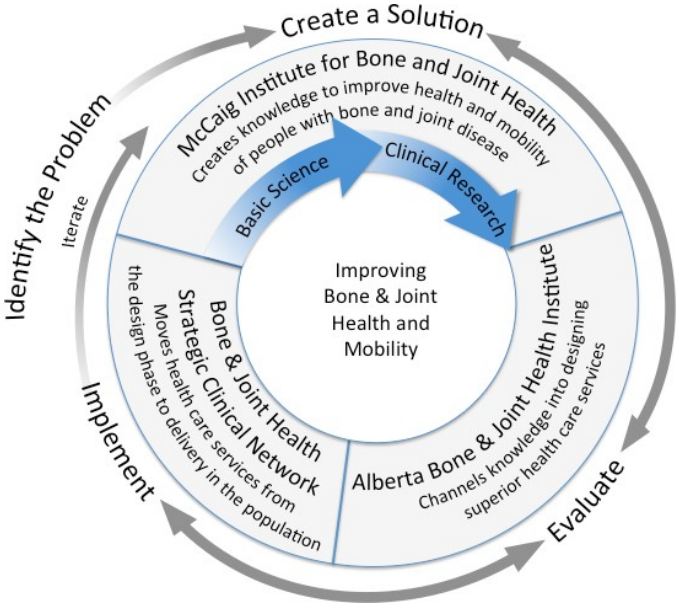

LIBIN CARDIOVASCULAR INSTITUTE of Alberta

The Libin Cardiovascular Institute of Alberta

The Libin Cardiovascular Institute of Alberta coordinates cardiovascular science research, education and patient care as an entity of both Alberta Health Services (Calgary) and the University of Calgary. It provides education and training of health-care professionals and offers world-class treatment using new technologies and access to cardiac services. There are more than 175 basic research, clinicians, and clinical research members who serve two million people in southern Alberta, Saskatchewan, and eastern British Columbia. The institute is committed to developing outstanding cardiovascular health promotion and disease prevention programs by translating innovative research into novel health-care solutions. For more information, visit LibinInstitute.org and @LibinInstitute on Twitter.

Hotchkiss Brain Institute

The Hotchkiss Brain Institute (HBI) at the University of Calgary consists of more than 125 scientists and clinician-scientists who are dedicated to advancing brain and mental health research and education. The Institute's research strengths, in the areas of Brain & Behaviour, Neural Injury & Repair and Healthy Brain Aging, are leading to new treatments for neurological and psychiatric disorders, aimed at improving quality of life and patient care. For more information, visit hbi.ucalgary.ca.

SPONSOR PROFILE

GForceTracker™ is an advanced athlete monitoring system that collects, measures and analyses head impacts & biometric performance data all in real time. MYTRAK™ technology enables three key elements; Impacts, Performance and rResearch. MYTRAK IMPACTS™ provides real time reporting of impact frequency and severity giving information required in real time to improve training, technique and maintain player safety. MYTRAK PERFORMANCE™ is a tool tailored to the individual player profile giving instant feedback on player activity, exertion and performance while MYTRAK RESEARCH™ enables researchers with detailed head kinematics that can be used to further improve the safety of sport. Please visit www.gforcetracker.com.

NOTES

PODIUM PRESENTATION ABSTRACTS

Effects of CT Reconstruction Convolution Kernels on Bone Quality Quantification

Andrew S. Michalski, W. Brent Edwards, Steven K. Boyd
University of Calgary, Calgary, Alberta

Introduction

Osteoporosis is a common musculoskeletal disorder that specifically affects the bones and is characterized by overall poor bone quality, bone fragility, and increased fracture risk [1]. Quantitative computed tomography (QCT) is an imaging modality for estimating bone mineral density (BMD), bone mineral content (BMC), and bone strength. QCT is often combined with finite element analysis (FEA) to predict failure strength and stiffness of bone. The material properties for the bone are derived from a density calibration phantom included in the image for the conversion of Hounsfield Units (HU) to density values. With each voxel converted to a density value, the total volumetric BMD (vBMD) can be calculated and a Young's modulus can be quantified for each voxel based on empirical equations in the literature [2]. The determination of the Young's modulus can be influenced by the QCT acquisition and reconstruction, leading to imprecise bone strength, stiffness, and fracture risk prediction [3].

There are multiple reconstruction convolution kernels used in the filtered back projection reconstruction method, and each kernel applies a different type of filter to the data during reconstruction. B30 is a medium smoothing kernel, which applies a small amount of blurring to the data and suppresses some noise [4]. B70 is a high sharpening kernel, which applies a high frequency filter to the data, increasing definition at edges in the data and increasing noise [4]. The B30 kernel is used for soft tissue viewing, while the B70 kernel is used for bone viewing, as depicted in Figure 1.

The purpose of this study was to determine the effects of reconstruction kernel on the quantitative assessment of bone quality. We hypothesize that the reconstruction kernel will affect the outcome measures of BMD, BMC, and bone strength.

Methods

Clinical QCT scans were obtained for the proximal femur. Each scan included a density calibration phantom in the field of view and was reconstructed using the B30 and B70 kernels. The femur in each scan was semi-manually segmented. HU were converted to density values based on a linear calibration curve derived from the phantom. vBMD and BMC values were determined for each femur. Young's moduli were calculated based on density values and empirical equations. Segmented femurs had FEA performed in a standard sideways fall loading configuration to estimate bone strength.

Results

Preliminary results show no difference in density calibration slopes with a B30 kernel slope of 4.5102 mgHA ccm^{-1} HU^{-1} and a B70 kernel slope of 4.4025 mgHA ccm^{-1} HU^{-1}. These data suggest there is not a significant effect of reconstruction kernel on BMD.

Conclusions

This work shows the effect of reconstruction algorithms on BMD estimates, and is an important input to QCT-based FEA models for osteoporosis and fracture risk prediction.

References

[1] Kleerekoper *et al.* (1985) *Calcif Tissue Int.*
[2] Courtney *et al.* (1994*) Calcif Tissue Int.*
[3] Dragomir-Daescu *et al.* (2015) *J Biomech.*
[4] Jang *et al.* (2011) *J Kor Phys Soc.*

Figures

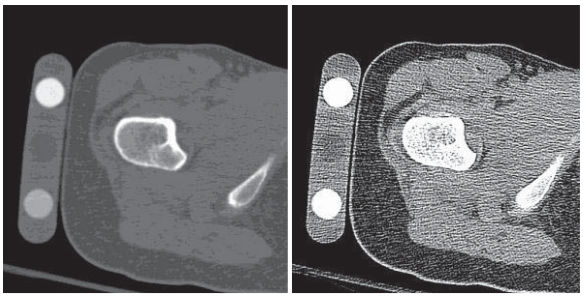

Figure 1: Left - Image reconstructed using B30 kernel. Right - Image reconstructed using B70 kernel.

Relationship between early language abilities and the underlying neural functional language network in preschoolers

Benischek, A., Dewey, D., Rohr, C., and Lebel, C.
University of Calgary, Calgary, Alberta

Introduction

Early childhood is a critical time for language development[1]. Language impairments that go untreated in the early years can result in decreased academic achievement and mental health concerns[2]. Therefore, early and effective language interventions are optimal for long-term benefits. Despite the importance of early language development, very little research has focused on the functional and structural brain changes in this critical time. Functional magnetic resonance imaging (fMRI) allows researchers to non-invasively study the relationship between functional neural networks and behaviour. MRI studies confirm that children with reading and writing difficulties show atypical structure and function in the language areas of the brain[3-4]. However, It still remains unclear how brain development is associated with language abilities in early childhood. ***The purpose of this study is to understand how variations in language abilities are functionally represented in the brain under development.***

Methods

The study includes 67 normally developing children aged 2.5 to 4.7 years (24 females and 38 males) who completed a language assessment (NEPSY-II Phonological Processing and Speeded Naming[5]) and underwent functional MRI scanning while watching a movie. The analysis in this abstract focuses on a preliminary analysis of 10 participants. These images were analyzed using FSL imaging software[6]. In the left-hemisphere, eleven language regions of interest were selected from a meta-analysis of reading[7] and two regions from expressive language task studies. Images were normalized to a high-resolution pediatric template optimized for ages 33- 44 months[8]. Whole-brain cross-sectional statistics were used to compare language scores to the brain's functional connectivity patterns, while controlling for confounding variables (age, sex, socioeconomic status).

Results

Language regions exhibited positive functional connections with adjacent areas, as well as homologous regions in the contralateral hemisphere (except for cerebellum). In contrast, negative functional correlations were found with more distant regions in the frontal, parietal, and occipital lobes. Phonological Processing language scores were positively correlated with the functional connections in the temporal-parietal junction, inferior occipital gyrus, fusiform gyrus and brain regions associated with language processing and comprehension ($p<0.05$). Speeded Naming language scores were positively correlated with the functional connections between the fusiform gyrus seed and the medial frontal gyrus and lateral occipital cortex ($p< 0.05$).

Conclusions

These results demonstrate that better language abilities in children are associated with stronger functional connections in brain regions associated with higher language abilities in adults. Performance on the Phonological Processing task showed stronger correlations with the functional connectivity among language regions in comparison to stronger positive correlations with executive functioning and sensory brain regions.

References

1. Berl, M. M., et al. 2014. Regional differences in the developmental trajectory of lateralization of the language network. Human Brain Mapping, *35*(1): 270-284.
2. Wilson, A.M., et al. 2009. The mental health of canadians with self-reported learning disabilities. Journal of Learning Disabilities *42*: 24. 2009.
3. Raschle, N. M., et al. 2011. Structural brain alterations associated with dyslexia predate reading onset. NeuroImage, *57*(3), 742-749.
4. Morken, F., et al. 2014. Children with dyslexia show cortical hyperactivation in response to increasing literacy processing demands. Frontiers in Psychology, *5*, 1491
5. Korkman, et al. 2007. NEPSY II, Clincal and interpretative manual. The Psychological Corporation, San Antonio TX.
6. Jenkinson, M., et al. 2012. FSL. NeuroImage, *62:*782 90.
7. Houde´O et al. (2010) Mapping numerical processing, reading, and executive functions in the developing brain: fMRI meta- analysis of 52 studies including 842 children. Dev Sci 13:876 – 885.
8. Fonov, V.S., et al. 2009. Unbiased nonlinear average age-appropriate brain templates from birth to adulthood NeuroImage, *47*(1): S102.

Effect of Hydrodynamic Shear on Proteoglycan 4 Synthesis and Secretion by Bovine Cartilage Explants

Alyssa A. Morin, Suresh C. Regmi, Tannin A. Schmidt
University of Calgary, Calgary, AB

Introduction

Proteoglycan 4 (PRG4) is a mucin-like glycoprotein that exists in synovial fluid as monomeric and disulfide-bonded multimeric forms[1], and is secreted by chondrocytes in bovine cartilage explants in vitro[2]. Dynamic shear stimulation of cartilage explant cultures has been shown to increase PRG4 mRNA expression levels[3], the quantity of high MW species, and overall PRG4 secretion[4] compared to unloaded controls. However, the effect of hydrodynamic shear on in vitro PRG4 synthesis and secretion remains unknown. Therefore, the objective of this study was to compare the quantity and immunoreactive size distribution of PRG4 products secreted into medium by chondrocytes in bovine cartilage explants from stirred bioreactor versus static T-flask cultures.

Methods

Cartilage discs were isolated from bovine stifle joints (N=5) and cultured in a stirred bioreactor (Shear +) or static T-flask with gentle nutation (Shear -) containing DMEM with 10ng/ml TGF-β1, at ~1ml/106cells/day for 27 days. Media was collected and replaced every three days. ***Quantity****:* Media aliquots were analyzed in duplicate for PRG4 by indirect ELISA[5] with mAb 4D6 (putative N terminal epitope)[6] using a standard of purified full-length rhPRG4[7]. ***Immunoreactive Size Distribution:*** PRG4 proteins in non-reduced (NR) and reduced (R) pooled Shear + and Shear – media were assessed by SDS-PAGE and 1.0% agarose gel electrophoresis (AGE) western blot using anti-PRG4 mAb 4D6 or mAb 9G3 (mucin domain epitope)[8]. ***Statistical Analysis:*** Data are presented as mean±SEM. A Mann-Whitney U-test was conducted for each collection point and over the culture duration, with Bonferroni correction.

Results

Quantity*:* The amount of PRG4 in Shear + media was significantly greater than Shear – media on days 16-18, 19-21, 22-24, 25-27 (all $p<0.05$), and over the culture duration ($p<0.001$) with mean values of 11.2±1.7 and 10.3±1.7ug/cm^2/day respectively (Fig.1). ***Immunoreactive Size Distribution*** *(data not shown):* Pooled Shear + and Shear - media contained a broad high MW mAb 4D6 immunoreactive species in NR samples, and a single ~460kDa monomeric[2] band in R samples when assessed by SDS-PAGE. Immunoreactivity to mAb 9G3 resulted in a broad high MW species in NR samples, and a less diffuse band with greater electrophoretic migration at ~460kDa in R samples. Similar immunoreactivity was observed in NR and R samples with mAb 4D6 when assessed by AGE.

Conclusions

Hydrodynamic shear through stirred bioreactor culture significantly up-regulates PRG4 secretion with no detectable difference in immunoreactive size distribution. These results contribute to the understanding of mechanical regulation of in vitro PRG4 synthesis and secretion. Additional study is required to further characterize the extent of hydrodynamic shear regulation on PRG4 secretion and the potentially confounding effect of TGF-β1.

References

[1]Schmidt+*BBA*'09, [2]Steele+*Trans ORS*'12, [3]Grad+*Tissue Eng*'06, [4]Nugent+*A&R*'06, [5]Schmidt+*A&R*'04, [6]Chawla+*ActaBiomat*'10, [7]Samsom+*Exp Eye Res*'*14*, [8]Jay+*A&R*'*12*

Figures

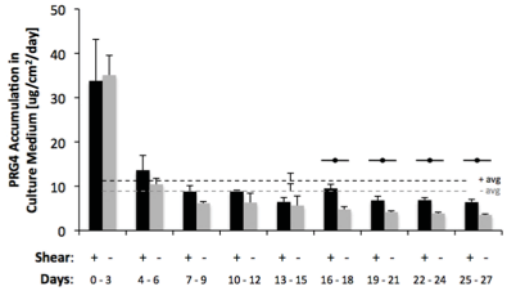

Figure 1: PRG4 accumulation [ug/cm^2/day] in Shear + and Shear – media over 27 day culture duration. Values are mean±SEM of 4 experiments, • $P < 0.05$.

Advanced Quantitative Magnetic Resonance Imaging for Temporal Lobe Epilepsy

Reza Basiri; Paolo Federico; R. Marc Lebel
Biomedical Engineering, University of Calgary
E-mail: rbasiri@ucalgary.ca

Introduction

Epilepsy is one of the major neurobiological diseases in Canada and worldwide. Approximately 1% of Canadians suffer from epilepsy and in less than 50% of these patients seizure cure is achieved mostly by surgical removal of the seizure focus[1].

Standard clinical magnetic resonance images (MRI) exams are able to detect large abnormalities but small foci are often not seen. Transverse relaxometry, a quantitative MRI technique that measures the signal decay time (T_2), has shown promise in detection of subtle abnormalities in temporal lobe epilepsy (TLE)[2]. Historically, this technique has produced inconsistent results, due primarily to sub-optimal data fitting. A recently proposed fitting method, called stimulated echo correction (SEC)[3], estimates major confounds associated with fitting errors in the transmit field and returns less biased results. SEC is a one-step least square method in which 3 parameters are used for fitting. Our aim is to develop and employ an improved SEC (iSEC) technique to reduce inconsistencies associated with T_2 estimation, leading to better identification of the seizure focus in TLE patients.

Methods

iSEC is a two-step method in which pre-estimated transmit field (B_1) values are used in the second step of fitting with only 2 parameters. Therefore reducing one degree of freedom and increasing precision. We compared and investigated validity and reliability between our iSEC and the standard SEC fitting methods by using simulated and *in-vivo* data.

Simulated data was generated with the extended phase graph algorithm assuming nominal acquisition and tissue parameters: 16 echoes, 10 ms echo spacing, T_1/T_2 of 3000/100 ms, and B_1 reduced to 0.75 of its ideal value. Gaussian noise ($10<SNR<100$) was added to mimic real MRI data. T_2 values were estimated using the original SEC and our proposed iSEC algorithm. Furthermore, to investigate our iSEC success rate in real MRIs, we examined 10 sequentially repeated scans in one volunteer. T_2 maps generated with both methods were evaluated based on variance across trials.

Results

Using simulated data, T_2 values estimated with the proposed iSEC method had ~25% less variance than with the original SEC method, Fig. 1. iSEC was found to be particularly beneficial in low SNR regions (<35). Overall, according to both simulated results and repeated real MRIs, the iSEC method is ~25% more precise than the standard SEC method.

Conclusions

Simulations and repeated MRIs indicate that precision in T_2 estimations has been considerably improved by using iSEC method. This is expected to translate into more reliable T_2 maps than can currently be generated, which may provide reliable detection of pathology in epilepsy and other neurological disorders. We anticipate achieving similar results when employing our proposed iSEC method to TLE patients. This work may provide tools to better understand the causal relationship between structural abnormalities and clinical symptoms and response to treatment in TLE.

References

1. Chang, B., & Lowenstein, D. (2003). Epilepsy. *The New England Journal of Medicine*, 349, 1257-266.
2. Sumar, I., Kosior, R., Frayne, R., & Federico, P. (2011). Hippocampal T2 abnormalities in healthy adults. *Epilepsy Research*, 273-276.
3. Lebel, R., & Wilman, A. (2010). Transverse relaxometry with stimulated echo compensation. *Magnetic Resonance in Medicine*, 1005-1014.

Figure

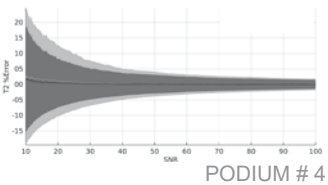

Figure 1) T_2 percent errors using SEC (grey) and iSEC (dark) over SNR range of 10-100.

Investigating Intersubject Variability in Pulsed Oxygen Delivery using Adult Nasal Airway Replicas

Charles P. Moore, Warren H. Finlay, and Andrew R. Martin
Department of Mechanical Engineering, University of Alberta, Edmonton AB, Canada

Introduction

Oxygen-conserving devices are frequently used in the administration of long-term supplemental oxygen to patients with persistent hypoxemia resulting from chronic obstructive pulmonary disease (COPD). To maintain patient quality of life, small portable sources of oxygen (O_2) that provide sufficient O_2 for short-term use outside the home, are highly desirable. A key aspect of many such systems is the administration of short O_2 pulses, or boli, timed to coincide with inspiration. The present work was performed to investigate the influence of intersubject variability in nasal airway geometry on the efficiency of pulsed O_2 delivery through nasal cannulas.

Methods

O_2 pulses were delivered through nasal cannula into five adult nasal airway replicas, extending from the nares to the trachea. These replicas were printed in acrylic plastic, based on airway geometries segmented from MR images of healthy subjects[1]. A mass flow controller (Alicat Scientific Inc., AZ) was used to deliver O_2 pulses with approximate volume of 50 ml, pulse half-width of 150 ms, and peak flow rate of 16 L/min. Tracheal O_2 concentration was measured over time using a laser diode oxygen analyzer (Oxigraf Inc., CA) for inhalation flow rates ranging from 10 to 40 L/min, and corrected for time response[2]. From this signal tracheal delivery efficiency, and dispersion of O_2 pulses through the nasal airways were determined. In addition, triggering pressure monitored at the nasal cannula supply tubing was measured.

Results

Intersubject variability in tracheal delivery efficiency and O_2 pulse dispersion was significant, but differences between airway replicas tended to be smaller than differences due to inhalation flow rate. Tracheal delivery efficiency for all five airway replicas is shown in figure 1, increasing on average from 0.54 ± 0.05 (average ± propagated error; n=5) at 10 L/min to 0.82 ± 0.08 at 40 L/min. Intersubject variability in triggering pressure was considerable, ranging from 0.02 to 0.06 cm H_2O at 10 L/min and from 0.18 to 0.56 cm H_2O at 40 L/min.

Conclusions

Significant inefficiencies were measured for pulsed oxygen delivery through nasal cannulas, especially at low inhalation flow rates. Pressure signals monitored at nasal cannula tubing varied considerably with flow rate and between airway replicas, and in several cases were below triggering sensitivities typical of commercial O_2-conserving devices.

References

1. Golshahi, L., Noga, M. L., Thompson, R. B., Finlay W. H. (2011). *In vitro* deposition measurements of inhaled micrometer sized particles in extrathoracic airways of children and adolescents during nose breathing. *Journal of Aerosol Science*, 42(7), 474-488

2. Langer, A. W., Hutcheson, S., Charlton, J. D., McCubbin, J. A., Obrist, P. A., Stoney, C. M. (1985). On-Line minicomputerized measurements of cardiopulmonary function on a breath-by-breath basis. *Phychophysiology*. 22(1), 50-58

3. Chatburn, R. L., Williams, T. J. (2010). Performance comparison of 4 portable oxygen concentrators. *Respiratory care*, 55(4), 433-442

Figures

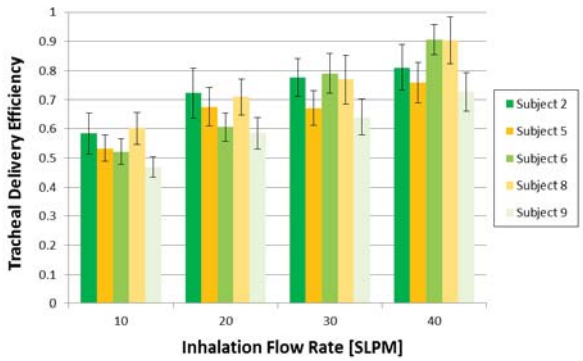

Figure 1: Tracheal delivery efficiency for all subjects at various supply flow rates

Towards a helmet assessment metric considering both focal head and diffuse brain injury

Brooklynn M. Knowles[1], James A. Newman[2], and Christopher R. Dennison[1]
[1]Biomedical Instrumentation Lab, Department of Mechanical Engineering, University of Alberta; [2]Newman Biomechanical Engineering Consulting Inc., Edmonton AB

Introduction

Contemporary certified helmets (e.g. CSA, ASTM) are considered to give adequate protection if they limit peak headform acceleration during a drop test to less than 300g. Helmets meeting the 300g criterion are credited with all-but eliminating focal injury to the head including contusion and hematoma (sometimes concomitant with more severe injury like skull fracture). In many sports with mandated helmet use mild diffuse brain injury (including concussion) is widespread. Angular head kinematics are known to cause diffuse brain injury [1]. There is no helmet standard that prescribes pass/fail thresholds for these angular kinematics. It is widely recognized that linear acceleration is a poor metric for head injuries associated with angular head motion, including diffuse brain injury of which concussion is an example. Therefore, there is much debate centered upon what metrics can be used to certify helmets relative to diffuse injury, while also retaining linear acceleration measures that have resulted in helmets that effectively prevent focal injuries. Our objective is to develop a New Injury Criterion, NIC, to be the first metric capable of simultaneously quantifying helmet performance relative to both fatal focal and rotationally induced diffuse injury.

Methods

We impacted a helmeted HybridIII head at 1.5 m/s to 4.2 m/s using the UofA helmet test bed (n=59 presented here). Peak linear acceleration (a_m) and angular velocity (ω) were used to develop several candidate NIC. Kinematics were input to the Simulated Injury Monitor (SIMon [2]) brain FE model and the Cumulative Strain Damage Measure (CSDM) was computed. CSDM represents brain tissue strain and is arguably the best metric for diffuse brain injury prediction. Regressions relative to CSDM convey which form of NIC was the most predictive of diffuse brain injury (R^2 closest to unity).

Fig.1: (top) test-bed; (bottom) FE

Results

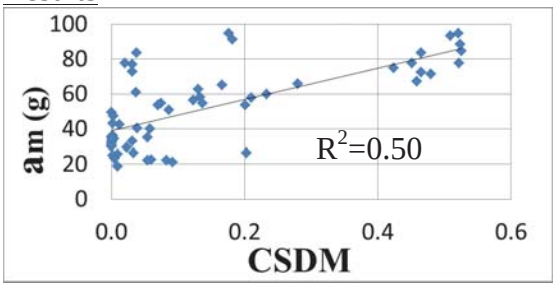

Figure 2: scatter plot of a_m and CSDM

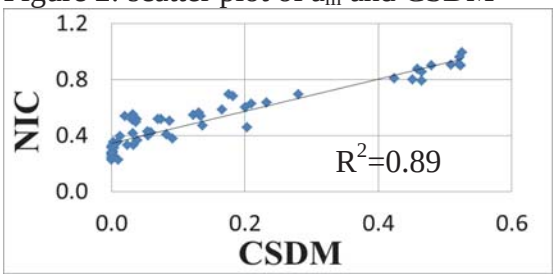

Figure 3: scatter plot of NIC and CSDM

Discussion and Conclusions

For NIC to be an advanced pass/fail criterion, it must scale linearly with CSDM (or diffuse injury risk). The current pass/fail criterion, a_m, is a poor linear predictor of CSDM (Figure 2). However, one of our NIC that incorporates both a_m and angular kinematics exhibits an R^2 of 0.89, indicating that it could be a good predictor of diffuse injury (including concussion) risk (Figure 3). NIC incorporates a_m, making it a good predictor of helmet performance relative to focal head injury. NIC also scales linearly with CSDM, making it a good predictor of helmet performance relative to diffuse and concussive injury as well. With continued validation and development of threshold approaches leading to pass/fail values, NIC could be the first pass/fail criterion for helmet testing uniting variables relevant to both focal and diffuse brain injury risk.

References

[1] Takhounts et al., STAPP v.57 (2013); [2] Takhounts et al., STAPP v.43 (2003)

THE INFLUENCE OF SHOE TYPE AND STRIDE LENGTH ON FOREFOOT LOADING AND FOOT STRIKE ANGLE DURING RUNNING

Colin Firminger[1], Ian Matthews[2], W. Brent Edwards[2]
[1]Biomedical Engineering Graduate Program, University of Calgary, [2]Faculty of Kinesiology, University of Calgary

Introduction

Repetitive loading, such as that seen in running, can cause a build-up of small cracks in bone. If loading cycles continue and the bone does not have adequate time to heal, cracks may accumulate, resulting in fatigue fracture[1]. Some 19% of all fatigue fractures occur in the metatarsals[2]. Fatigue fracture is highly dependent on load magnitude[3], and two potential mechanisms of load reduction include increased shoe cushioning and decreased stride length. The purpose of this study was to investigate the effects of shoe cushioning and stride length on metatarsal loads and foot strike angle during running.

Methods

Eleven male recreational runners (26 ± 4.5 years, 178.5 ± 5.5 cm, 76.2 ± 6.1 kg) with a rear-foot strike pattern and no prior experience running in minimalist footwear participated in this study. The data collection session consisted of four overground running conditions, each with ten trials, where participants ran approximately 20 metres per trial at their preferred running speed (±5%). The four conditions were: (1) control shoe at preferred stride length (PSL); (2) control shoe at 90% PSL; (3) minimalist shoe at PSL; (4) minimalist shoe at 90% PSL. The control shoe was a New Balance 890v5, weighing 8.6 oz with a 19.0 mm heel profile and 11.0 mm toe profile. The New Balance Minimus Zero v2 was selected for the minimalist shoe, weighing 5.9 oz with a 12.8 mm heel and 12.0 mm forefoot. PSL was manipulated using tape adhered to the floor. Nineteen markers were placed on each subject's pelvis and right lower extremity and motion capture data were recorded at 240 Hz (Motion Analysis Corporation; Santa Rosa, CA, USA). Plantar pressure data were recorded concurrently at 200 Hz using a Pedar-X pressure sensing insole (Novel; Minneapolis, MN, USA). Pressure data was sectioned into ten arrays (heel, midfoot, metatarsals 1, 2, 3, 4, 5, and toes 1, 2, 3-5) and maximum force during stance was obtained for each array. A 2 x 2 repeated measures ANOVA was used to compare trial-averaged forces and foot strike angles among the four conditions ($\alpha = 0.05$).

Results

Maximum loads at all metatarsals were significantly greater when running in the minimalist shoe ($p \leq 0.004$, Figure 1); no effects of stride length were observed ($p \geq 0.086$). Foot strike angle (FSA) was significantly greater for the control shoe (29.9 ± 2.7°) compared to the minimalist shoe (23.7 ± 5.9°). FSA was also significantly greater for PSL (28.3 ± 3.0°) compared to 90% PSL (25.2 ± 5.5°), suggesting that participants contacted the ground with a more dorsiflexed foot when running at PSL and in the control shoe.

Conclusions

Findings illustrate that metatarsal bones experience higher loads when running in minimalist shoes, suggesting a potential increased risk for metatarsal fatigue fracture. Reductions in stride length do not appear to decrease metatarsal loads during running.

References

[1] Harrast (2010). Clin Sports Med. 29:399-416.
[2] Gray (1974). J Biomech. 7:287-292.
[3] Orava (1980). Br J Sports Med. 14:40-44.

Figures

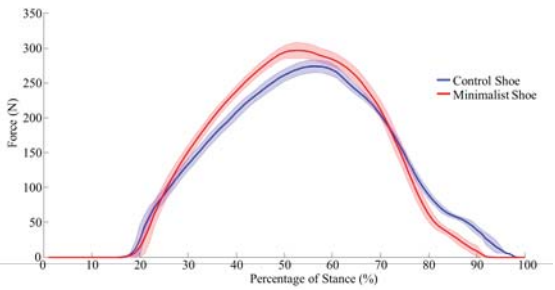

Figure 1: Ensemble average 2nd metatarsal force for a representative subject running at PSL. Force is larger in the minimalist shoe and occurs earlier in the stance phase compared to the control shoe.

Inhibiting p21 using small molecules to promote chondrogenesis in MSCs

Karri L Bertram[1], Roman J Krawetz[2]
[1]Biomedical Engineering Graduate Program, [2]Department of Cell Biology and Anatomy
University of Calgary, Calgary AB

Introduction

Osteoarthritis (OA) currently affects 1 in 8 Canadians and the number is expected to rise significantly [1]. Cartilage degeneration causes significant pain in OA patients yet cartilage has a very limited intrinsic healing ability. Mesenchymal stem cells (MSCs) found in the synovium of joints are thought to contribute to the repair of cartilage in healthy joints[2]. There are and increased number of MPCs in OA joints, however they have a decreased ability to differentiate into chondrocytes.. Mice lacking p21, a cell cycle inhibitor, have an increased repair response in many adult tissues, including cartilage[3]. However, sustained ubiquitous suppression of p21 leads to autoimmune disorders and cancer. Temporarily and locally inhibiting p21 in MSCs derived from the synovium may have the potential to increase their chondrogenic potential, leading to a novel treatment of cartilage defects and OA. This project is aimed at identifying p21 inhibitors and characterizing their effect on MSCs during chondrogenesis.

Methods

OA MSCs were extracted from synovial membrane tissue donated by patients of Dr. Jim Powell during reconstructive surgery.

Normal MPCs were extracted from synovial membrane tissue from the Southern Alberta Tissue Donation Program. Cells derived from the synovial membrane (normal and OA) were purified for CD90, an MSC marker.

Chondrogenesis: Cells were pelleted at 50,000 cells and cultured in 1 ml of chondrogenic media for 21 days.

Compound Screening: Xman NanoLuc are genetically modified to produce luciferase when p21 is expressed. Luciferase was detected using a luminescence assay and Victor plate reader.

RT-PCR: RNA was extracted from samples using RNA Easy Mini Kit. RNA was converted to cDNA using a High Capacity cDNA Reverse Transcriptase Kit. RT-PCR was run on the samples using TaqMan Universal PCR Mastermix. 18S was used as a housekeeping control.

Results

Using Xman NanoLuc cells, five compounds were identified as putative p21 inhibitors during a screening of 170 compounds targeting the complete spectrum of kinases implicated in cancer cell growth and survival. Under normal culture conditions each compound decreases the expression of p21 in MSCs with a different profile over the course of 8 days of exposure. The viability of human OA and normal MSCs was not diminished when exposed to each of these compounds at concentrations lower than 1μM for 48hrs. Chondrogenesis was undertaken with each compound, and a correlation with p21 and SOX9 (chondrogenic marker) expression was observed (Figure 1). In particular, compound 102 increased the chondrogenic potential compared to the control.

Conclusions

This project aims to characterize the effect of p21 inhibition on OA and normal MSCs with the goal of identifying a novel pharmacological intervention for treating cartilage pathologies such as OA.

References

[1] Arthritis Alliance of Canada, "Arthritis Alliance of Canada, The Impact of Arthritis in Canada: Today and Over the Next 30 Years." [Online].

[2] Hunziker et al., "Repair of Partial-Thickness Defects in Articular Cartilage: Cell Recruitment from the Synovial Membrane". *J Bone Joint Surg Am,* vol. 78, no 5. p. 721-33, May 1996.

[3] L. M. Arthur and E. Heber-Katz, "The role of p21 in regulating mammalian regeneration.," *Stem Cell Res. Ther.*, vol. 2, no. 3, p. 30, Jan. 2011.

Figures

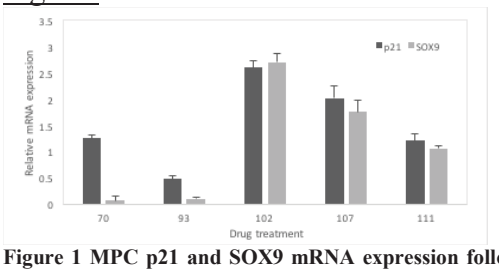

Figure 1 MPC p21 and SOX9 mRNA expression following 21 days of chondrogenesis.

DIET INDUCED OBESITY MAY AFFECT THE FORCE-VELOCITY RELATIONSHIP IN RAT SOLEUS

Myles J. Borthwick[1], Kelsey H. Collins[1,2], Andrew J. Sawatsky[1], Sudeepta Aurka[1], Ian C. Smith[1], Walter Herzog[1,2]
[1]Human Performance Laboratory, University of Calgary, [2] Biomedical Engineering, University of Calgary
Myles.borthwick@ucalgary.ca

INTRODUCTION

Obesity is associated with chronic, low-grade inflammation that has been shown to affect several musculoskeletal tissues [1]. Previously, we observed that diet induced obesity (DIO) using a high-fat, high sugar diet results in molecular and morphological alterations in muscles, including an increase in intramuscular fat. However, it remains unclear if these alterations affect muscle function, as few studies have characterized the functional properties of muscles in obese individuals [2]. Arguably, one of the most important functional properties of skeletal muscle is the force-velocity relationship (FVR). As fat infiltration reduces the contractile material and structure of obese muscles, the functional properties of muscles, specifically the FVR may be affected. Therefore**, the purpose** of this study was to characterize the FVR in rat soleus muscles obtained from obese and normal rats. We hypothesized that soleus muscles of obese rats would produce lower absolute and relative forces at any given shortening velocity compared with muscles from control animals.

METHODS

Outbred, individually housed male Sprague-Dawley rats, aged 10-12 weeks, were randomized to a high fat, high sugar diet (DIO) or a standard chow diet for 12 weeks. Prior to surgery, animals were sedated, weighed, and body composition was quantified using dual energy X-ray absorptiometry. The right soleus muscle was exposed and a custom cuff-type electrode was implanted on the tibial nerve. The soleus tendon was isolated from the Achilles with the calcaneus attached and fixed to a motor along the muscle's natural alignment. The muscle was then stretched to its optimum length and electrically stimulated at 35Hz at 2.5x the motor unit threshold [3]. An isometric force reading was acquired over 2.5 s stimulation. The soleus was then stretched past its optimum length and shortened at increasing velocities, a force reading was collected at optimal length using Windaq Software. Data were collected at 1000Hz. Forces during shortening were measured at the same length and time point as the isometric reference force. This process was repeated for shortening velocities increasing from 2 mm/s to 70 mm/s. Instantaneous forces were normalized to the peak isometric force for each animal. Comparisons were made using a Student's t-tests, α=0.05.

RESULTS

On average, DIO animals had higher body mass and body fat compared to the control rats ($p<0.001$). Soleus mass was similar between DIO animals and chow ($p=0.321$), as was peak active isometric force (DIO: 2.48±0.10 N, chow: 2.08±0.33 $p=0.183$). FVR relationships were statistically different at shortening velocities between 3 and 35 mm/s (DIO > Chow at each given velocity; $p<0.05$, Fig. 1).

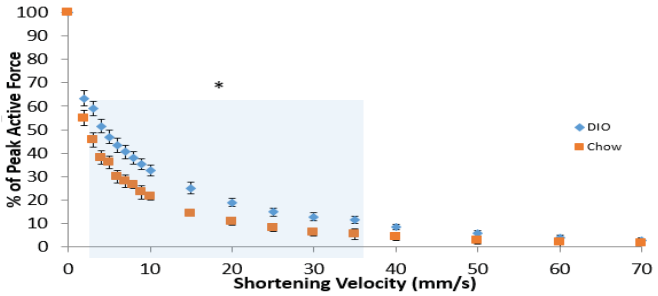

Figure 1. *Normalized forces were higher in DIO soleus than chow soleus across most velocities evaluated.* Values are mean ± standard error of the mean, * indicates $p<0.05$.

DISCUSSION

The results opposed the expected outcomes of this study and, therefore, the hypothesis was not satisfied. These findings could be due to a higher proportion of fast twitch fibers in the DIO or longer fascicle lengths in the DIO rats, but these speculations remain to be tested. Future work will examine other structural levels and muscle contractile proteins to understand these preliminary findings.

REFERENCES

1. Collins KH *et al. Osteoarthritis Cartilage.* In press 2015.
2. Ciapaite J *et al. J Nutr Biochem.* **26**:155-164, 2015.
3. Hisey B *et al. J Biomech.* **42**:1488-1492, 2009.

Preliminary Study on Cell-laden Hydrogel Constructs for Cartilage Tissue Engineering

Fu You[1], Xia Wu[1], Xiongbiao Chen[1], Brian F. Eames[2]
[1] Division of Biomedical Engineering, College of Engineering, University of Saskatchewan; [2] Department of Anatomy and Cell Biology, College of Medicine, University of Saskatchewan

Introduction

Hydrogels are particularly attractive as materials to incorporate living cells in cartilage tissue engineering. However, the development of such cell-laden hydrogel constructs based on the 3D printing techniques remains challenging due to the issues related to cell functions and structure integrity. Previous studies [1,2] showed the feasibility of printing Schwann cell-laden alginate/ hyaluronic acid hydrogel scaffolds for nerve tissue engineering. Inspired by this, our study was aimed to apply the 3D printing techniques to fabricate chondrogenic cell-laden hydrogel constructs for cartilage tissue engineering. This abstract presents the preliminary results of our study.

Methods

ATDC5 cells and alginate solution (2 w/v%) were homogenously mixed at a density of 5×10^6cells/ml. The obtained mixture was then dispensed through a needle with an internal diameter of 200 μm of the 3D Bioplotter (Envision) into the crosslinking medium in a tissue culture plate, forming the cell-laden hydrogel construct with a 0°/90° layer structure (i.e., the strands of one layer were perpendicular to those of the adjacent layers). The crosslinking medium was of 100 mM calcium chloride with 0.1%w/v PEI and 1.05%w/v PVA; and the tissue culture plate was pre-treated with 0.1 w/v% PEI in PBS overnight at 37℃ for improved structure integrity [1, 2]. To characterize the cell-laden hydrogel constructs, the cell viability was examined by using a live/dead viability kit, and the expression of sulfated glycosaminoglycan (sGAG) and type II collagen was detected by Alcian Blue staining and immunofluorescent staining, respectively, at Day 14 of cell culture.

Results

Fig. 1(a) shows the fabricated hydrogel scaffolds. Fig. 1(b) shows cell-laden hydrogel constructs at Day 14 of cell culture. The examination of cell viability showed that most cells incorporated into the constructs were alive at Day 14 (Fig. 1c and d). The results from Alcian Blue staining and immunofluorescent staining demonstrated the formation of cartilage ECM including sGAG and type II collagen expressed by the ATDC5 cells at Day 14 (Fig. 1e and f).

Conclusions

Based on the 3D printing technique, porous cell-laden hydrogel constructs were successfully fabricated with the illustrated structure integrity. Post the 14 days of cell culture of the constructs, the cell viability and functions were examined with the results of high viability and ECM formation. This preliminary study illustrates the promise of the cell-laden hydrogel constructs in cartilage tissue engineering.

References

[1] Rajaram A, et al. *J. Biomater. Sci., Polym. Ed.,* 2015. [2] Rajaram A, et al. *3D Printing and Additive Manufacturing,* 2014.

Figures

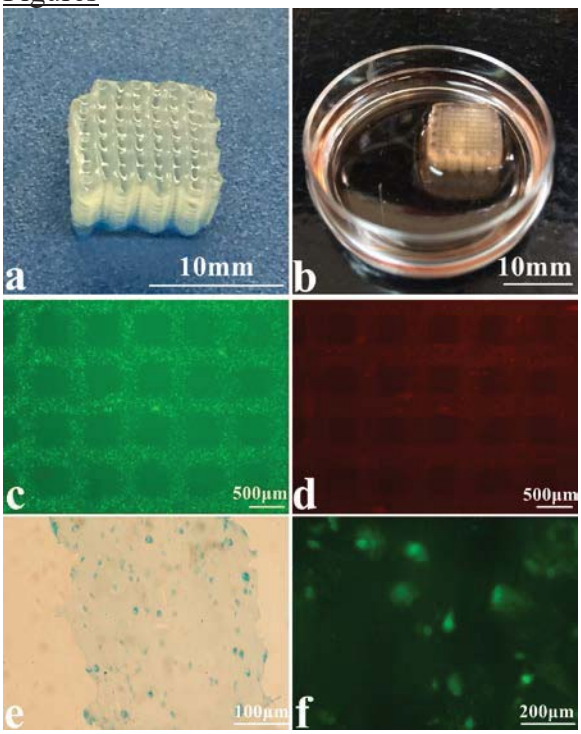

Figure 1 (a) hydrogel scaffolds; (b) cell-laden hydrogel constructs at Day 14 of culture, fluorescent images (c, d) of the cell-laden hydrogel constructs showing live (green) and dead (red) cells; expression of sGAG (e) and type II collagen (f); all (c)- (f) were examined at Day 14.

Precision of bone properties and strength estimates in children

Hunchak J.B.[1], Kawalilak C.E.[1], Björkman K.M.[2], Duff W.R. [2], Federow C.W.[2], Johnston J.D.[1], Kontulainen S.A.[2]
[1] Department of Mechanical Engineering; University of Saskatchewan; Saskatoon, SK, Canada
[2] College of Kinesiology; University of Saskatchewan; Saskatoon, SK, Canada

Introduction

Precise measurements of bone strength development in children are fundamental when investigating factors underpinning pediatric fractures and antecedents of osteoporosis. Peripheral quantitative computed tomography (pQCT) is commonly used in pediatric research to monitor skeletal development in the arm and leg bones. However, lack of standardized methodology for image acquisition and analysis makes the interpretation of and comparison between studies challenging. Further, the precision errors in children have not yet been reported. Our objective was to compare the precision and mean outcomes of pQCT-derived bone properties and strength indices across commonly reported analysis methods at the tibia shaft in children **[1, 2, 3]**.

Methods

Tibia shafts of 35 healthy children (mean age: 10.5 ± 1.7 years) were scanned twice using pQCT (Stratec XCT2000). The images were analyzed using five threshold values defining outer and inner bone boundaries (200, 280, 480, 540, and 710 mg/cm^3) using ImageJ open source software with the BoneJ plugin **[4]**. We determined precision errors ($CV\%_{rms}$) **[5]** and means for: total bone area (ToA); cortical area (CoA), density (CoD) and content (CoC); cross-sectional area moments of inertia (I_{min}, I_{max}, I_p); density-weighted cross-sectional area moments of inertia (dwI_{min}, dwI_{max}, dwI_p); and density-weighted section moduli (SSI_{min}, SSI_{max}, SSI_p). We compared log transformed precision errors (CV%) and means using MANOVA with Bonferroni adjustment for multiple comparisons. Significance was accepted with $P<0.05$.

Results

On average, the threshold of 710 mg/cm^3 resulted in 8-37% higher precision errors relative to the lower thresholds for all outcomes, except CoD (**Fig 1**). Overall, bone properties and strength indices were most precise when obtained with the 480 mg/cm^3 threshold (**Fig 1**). The 710 mg/cm^3 threshold resulted in 16-79% lower bone outcomes (except for CoD) compared to the other thresholds (**Fig 2**).

Conclusion

The most precise analysis of tibia bone properties and strength indices in children was obtained by using the threshold of 480 mg/cm^3. The commonly used cortical bone threshold of 710 mg/cm^3 was least repeatable, possibly due to an underestimation of cortical bone size. As such, 710 mg/cm^3 is not recommended for analysis of tibia shaft pQCT images in children, apart from measures of cortical bone density.

References

[1] Adams et al (2014) Journal of Clinical Densitometry; **[2]** Ashby et al. (2011) Osteoporosis International; **[3]** Macdonald et al (2006) Bone; **[4]** Rantalainen et al. (2011) Journal of Musculoskeletal and Neuronal Interactions; **[5]** Glüer et al. (1995) Osteoporosis International

Figures

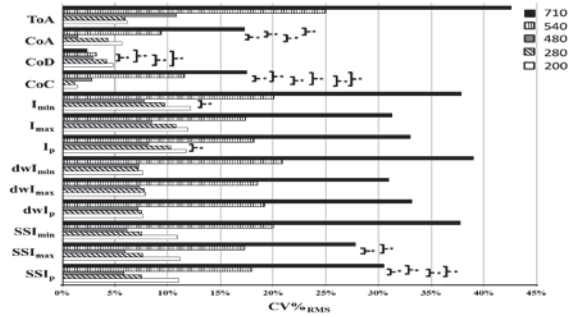

Figure 1: Precision errors ($CV\%_{rms}$) across five analysis thresholds. * Significance at $P<0.05$.

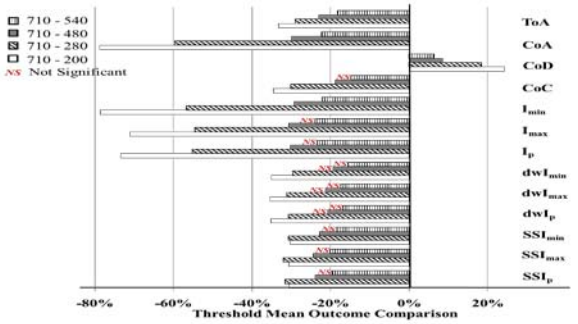

Figure 2: Comparing 710 threshold mean outcomes to 200, 280, 480, and 540 threshold mean outcomes.

Does high mileage running cause knee osteoarthritis in rats?

Jaqueline Lourdes Rios[1,2], Kevin Boldt[1], Ruth-Anne Seerattan[1], Walter Herzog[1]
[1]University of Calgary, [2]Coordination for Higher Education Improvement (CAPES)

Introduction

Osteoarthritis (OA) is the most common form of arthritis and is associated with chronic pain and loss of mobility. There is evidence suggesting that mechanical overloading causes knee OA. Running is known to put high mechanical loads on the knee, and thus running has been thought to be a good model to test the hypothesis that mechanical overloading causes knee OA in an otherwise healthy joint. The purpose of this study was to use increasing running loads and test the hypothesis that moderate running will produce positive anabolic responses while high mileage running will cause negative catabolic responses in the rat knee.

Methods

Three-month-old male Sprague-Dawley rats were randomized into four groups: no exercise (control) group (n=5), moderate running (MD, n=6), high duration running (HD, n=6), and extra high duration running (EHD, n=6). The training consisted of an 11 week progressive treadmill running program (Table 1). Body mass was recorded each week, and rats were euthanized and tissue harvested immediately following the 11 week training program. Histologic serial sections of the knee articular cartilage were cut at 10 μm thickness and stained. Two independent graders assessed all sections in a blinded manner using an adapted Mankin (1) histology scoring system. Kruskal-Wallis testing was used to test differences in knee joint between groups and across nine knee joint locations (α=0.05).

Results

Body mass increased consistently for all groups except for the EHD group, which increased body mass until week 9 (coinciding with a steep increase in running duration), and then lost 10% mass over the final three weeks. No changes in cartilage integrity were found between groups or between joint locations (Figure 1).

Conclusions

The results of this study led to the conclusion that there is no relationship between OA and running in rats, even after 11 weeks of running up to 4 hours per day. Analysis of possible adaptive responses to the running intervention is currently performed. We conclude that excessive running is not detrimental to rat knee joints.

References

1. Mankin HJ, et al. J Bone Joint Surg Am. 1971.

Tables and Figures

Table 1. Eleven weeks treadmill training protocol.

Week	MD	HD	EHD
1-8	30 min/day, 5 days/week	60 min/day, 5 days/week	60 min/day, 7 days/week
9	30 min/day, 5 days/week	60 min/day, 5 days/week	2h/day, 7 days/week
10	30 min/day, 5 days/week	60 min/day, 5 days/week	3h/day, 7 days/week
11	30 min/day, 5 days/week	60 min/day, 5 days/week	4h/day, 7 days/week

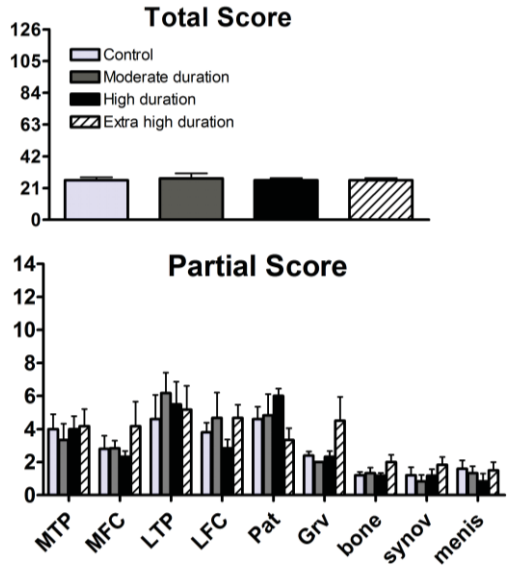

Figure 1. Adapted Mankin Score. MTP = medial tibial plateau, MFC = medial femoral condyle, LTP = lateral tibial plateau, LFC = lateral femoral condyle, Pat = patella, Grv = femoral grove, synov = synovia, and menis = menisci.

Detection of the mitochondrial enzyme cytochrome oxidase brain of a mouse model

Daniel Korchinski, Thomas Johnson, Dr. Jeff Dun
Experimental Imaging Centre, basement level P2, TRW Building, 3280 Hospital Dr NW, Calgary

Introduction

Mitochondrial dysfunction appears to be causally involved in a variety of neurological diseases, including multiple sclerosis, Alzheimer's, Parkinson's, birth asphyxia, traumatic brain injury, and post-surgical neurological dysfunction[1,2]. Non-invasive methods to track mitochondrial function would be useful for both patients suffering and researchers. While there are well developed animal models for these diseases, we lack non-destructive means to quantify mitochondrial function. Near Infrared Spectroscopy (NIRS) may be able to do so, as cytochrome c oxidase (COX) has significant absorption in this band. COX is significant, as its redox state is dependent upon electron flow through the mitochondrial electron transport chain.

While typical NIRS systems capable of tracking COX can only measure changes in COX concentration, one aim of this project was to make absolute concentration measurements. This was accomplished by adopting a second differential algorithm typically used in measurements of hemoglobin to account for unknown tissue geometry and scattering effects[3].

Methods

Mice (n=11) were anaesthetized by spontaneous ventilation of 3% isoflurane, 30% O_2 and 67% N_2. After baseline NIRS measurements were taken, mice were subjected to a 1 minute anoxia pulse.

NIRS data was collected with a cooled Andor CCD camera and Shamrock SR303i to quantify absorption of broadband light in the 712-985nm band at 1Hz. Light was transmitted and collected through two fiber optics placed on the dorsal skull.

Data was processed with an in-house Matlab implementation of the second differential algorithm and with COX spectral data from bovine heart.

Results

Baseline concentrations of oxidized COX (oxCOX) and reduced COX (reCOX) were obtained [tCOX] = 12.5uM (Fig. 1), about twice that reported for rats. A significant decrease (-3.35uM, $p<.001$) in [oxCOX] was observed in response to anoxia. [reCOX] did not increase.

Conclusions

It is encouraging that the measured [tCOX] was somewhat higher than in a rat because it is likely that mitochondria density is higher. It is also encouraging that [oxCOX] decreases with anoxia as expected. The analysis for [reCOX] suggests a lack of sensitivity to the relatively featureless absorption spectrum of reCOX or crosstalk with deoxyhemoglobin. Improvements in signal to noise or in processing might aid in recovering the reduced COX signal. NIRS promises to be a valuable non-invasive tool for assessing mitochondrial function.

References

1. Lin, M.T. & Beal, M.F. Mitochondrial dysfunction and oxidative stress in neurodegenerative diseases. *Nature* **443**, 787-795 (2006).
2. Nollert, G., *et al.* Postoperative Neuropsychological Dysfunction and Cerebral Oxygenation During Cardiac Surgery. *Thorac cardiovasc Surg* **43**, 260-264 (1995).
3. Matcher, S. & Cooper, C. Absolute quantification of deoxyhaemoglobin concentration in tissue near infrared spectroscopy. *Physics in medicine and biology* **39**, 1295 (1994).

Figures

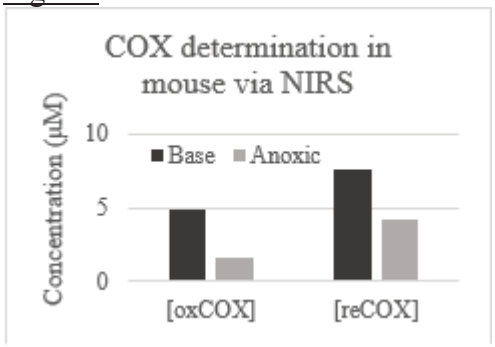

Figure 1. [COX] in mice during anoxia and rest, as measured via NIRS.

CaMos Youth Cohort 3D Image Registration

Jennifer L Bhatla[1,2], Sarah L Manske[1,2], Lauren A Burt[1,2], Steven K Boyd[1,2]
[1]McCaig Institute for Bone and Joint Health; [2]Department of Radiology, University of Calgary

Introduction

Osteoporosis is a degenerative bone disease[1] being studied using high resolution peripheral quantitative computed tomography scanners (HR-pQCT, XtremeCT, Scanco Medical). HR-pQCT assesses bone microarchitecture providing various applications in osteoporosis research. When performing comparison or follow-up studies, such as the Canadian Multicenter Osteoporosis Study (CaMos), it becomes necessary to register images obtained at different times. The CaMos project is a prospective study-assessing aging and bone loss across Canada. The Calgary youth cohort[2] (age 16-24, N = ~150) was scanned once to determine a baseline and again two to three years later to obtain a follow-up. The images need to be registered to analyze the same region of interest for accurate assessment of changes.

Methods

Performing automated 3D image registration for subsequent quantitative analysis of the registered data is being done using IPL software (Image Processing Language, Scanco Medical). The image registration script uses the baseline and original aims and periosteal masks in order to register the images using linear interpolation. Registration determines the transformation that maps the follow-up image onto the baseline by iterating to find transformations and rotations that maximize the correlation coefficient. The initial guess is determined using mass center and moment of inertia. This is done at low resolution to obtain the first approximate registration and then at increasing resolutions to refine the registration. The output is a text file of this transformation matrix. This is used to transform the follow-up segmented image into the segmented baseline image space and create a registered image showing the common region in purple, the regions unique to the baseline in red, and regions unique to the follow-up region in green (Fig 1), to confirm successful registration.

Once the transform matrix has been obtained, it is used to generate common region periosteal, trabecular, and cortical masks to identify regions of interest within the bone. The baseline common region masks are created by transforming the follow-up image into the baseline image space. Images are concatenated and thresholded so that only the common region remains. The image is then cut with the baseline periosteal and trabecular masks to create common masks. Cortical masks are generated by subtracting common region trabecular masks from the periosteal masks. The same process is done to create follow-up common region masks.

Successful registration can be confirmed visually by examining 3D registered images. A common mask superimposed on a 2D slice can also be used to visually verify that an appropriate common region has been determined. Successful registration can be assessed quantitatively by calculating percent volume overlap by comparing volumes of the periosteal masks for the common region on each scan. The volume of the masks should be similar, differing slightly due to bone growth.

Results

To date we have successfully registered 48 sets of baseline and follow-up scans. The average percent overlap is 96% with all but one sample over 85% overlap. The remaining sample has very little overlapping scanned region giving a 41% percent overlap. This indicates that calculations accurately identify poorly scanned or registered samples.

Conclusions

This method will allow the change in a patient's bone microarchitecture, density and strength over time to be more accurately determined by using the common regions which will lead to a better understanding of osteoporosis and the factors that influence it. The method is currently being applied the Calgary CaMos Youth cohort but will be applied to the full Calgary CaMos cohort (N = ~800) spanning a larger age range as well as other projects that require image registration.

References

[1] Kanis J.A. et al, Osteoporosis Int. 2002
[2] Burt L. A. et al, Arch Osteoporos. 2014

Figures

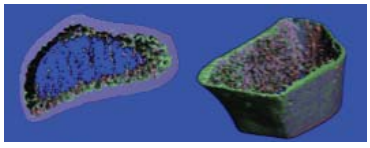

Fig 1: Registered tibia (cross sectional and 3D views). Purple indicates common region, red baseline, green follow-up.

Titin Hysteresis and Elasticity in Actively Stretched Muscle Myofibrils

Craig Martis[1], Kaleena Johnston[2], Azim Jinha[2], Tim Leonard[2], & Walter Herzog[1, 2]
Human Performance Laboratory, Faculties of Engineering[1] and Kinesiology[2], University of Calgary

Introduction

Titin is a protein that spans the length of a half sarcomere in myofibrils. It behaves like a molecular spring, playing a role in stabilizing sarcomeres and regulating passive force [1, 2]. Isolated titin has been shown to be essentially elastic if immunoglobulin (Ig) domain unfolding-refolding is prevented [3]. In its native, sarcomeric environment, it has been suggested that stretching and holding a myofibril at long lengths produces a time-dependent unfolding of all Ig domains, thus, allowing titin's elastic behavior to be exhibited [4]. Experiments on active myofibrils showed a decrease in force and a persistent hysteresis throughout a stretch-shortening (SS) protocol, suggesting a time-dependent unfolding of Ig domains [5]. We hypothesized that holding active myofibrils at long lengths prior to SS cycles should allow most Ig domains to unfold, thus eliminating force loss and hysteresis to reveal titin's expected elastic properties.

Methods

Isolated rabbit psoas muscle myofibrils (n = 5) were attached at one end to a glass needle (to control length) and at the other end to a nanolever (to quantify force). Myofibrils were activated at an average sarcomere length of 2.7 μm, and then stretched to 5.2 μm, where they were held for 2 min. Myofibrils then underwent a SS protocol with amplitude of ± 0.25 μm (10 cycles) before being shortened to their original length. Myofibril length, area, and force were quantified. Myofibril stress was calculated as force/area. Hystereses were calculated as the area enclosed by the loading and unloading curves, normalized (%) to the area under the loading curves of the force-length plots obtained for each SS cycle

Results

Peak stress throughout the 10 cycles remained approximately constant, averaging 101 ± 6 % relative to the first cycle (Fig 1a). Hystereses did not follow a trend throughout the 10 SS cycles and averaged 17 ± 8 % (Fig 1b).

Conclusions

The "constant" stress across the SS cycles is characteristic of an elastic response; however, the persistent and non-negligible hysteresis is indicative of viscous properties. Since stress remained relatively constant, we conclude that all Ig domains were unfolded prior to the start of the SS cycles, as expected. Therefore, we suspect that the hystereses must originate from a source other than Ig domain unfolding/refolding. At this point, any explanation for the remnant hysteresis is highly speculative but might be associated with continuous titin binding-unbinding to another structural (titin) or contractile (actin) protein, as has been suggested in previous work [4].

References

[1] Herzog JA et al. *J Biomech*. **45**: 1893-1899, 2012.
[2] Herzog JA et al. *Mol Cell Biom*. **11**: 1-17, 2014.
[3] Kellermayer MSZ et al. *Science*. **276**: 1112-1116, 1997.
[4] Herzog JA et al. *Biophysical Society Annual Meeting* (poster), 2014
[5] Herzog, JA, et al., *Biophysical Society Annual Meeting* (poster), 2015

Figures

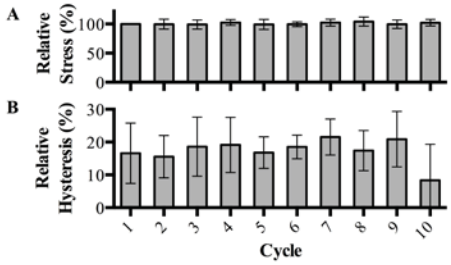

Figure 1. Data from each of the 10 cycles, averaged over the 5 experiments, with standard deviation error bars. **A** Peak stress relative to the stress of the first cycle. **B** Hysteresis relative to the loading energy of each cycle.

Nanoparticle localization in angiogenic vessels to regions of disturbed flow

Juliana Gomez[1], Hagar Labouta[1], Bahareh Vafadar[2], Amber L. Dorion[1,3], David T. Cramb[4], Sarah J. Childs[5], Kristina D. Rinker[1,3,6]

[1]Cellular and Molecular Bioengineering Research Lab, [2]Zymetrix Bose Biomaterial & Tissue Engineering Technology Development Centre, [3] Department of Chemical and Petroleum Engineering, University of Calgary, [4]Department of Chemistry, [5] Department of Biochemistry and Molecular Biology, [6] Centre for Bioengineering Research and Education

Introduction

The development of nanoparticles that can be used in the biomedical field as drug delivery or imaging systems provide great opportunities to treat and diagnose diseases more efficiently. Since the majority of these nanoparticles require vascular administration, understanding nanoparticle localization in a physiologically-relevant flow environment is important for determining toxicity risk profiles and efficacy.

Nanoparticle intravascular distribution is affected by vessel dimensions, vascular branching architecture and blood flow patterns[1]. Endothelial cells lining the blood vessels are exposed to fluid forces such as shear stress. Studies have shown that nanoparticle accumulation depends on shear stress and in general, lower shear stress results in higher accumulation[2]. Since nanoparticle accumulation changes with shear stress, we hypothesized that it also differs in regions of disturbed flow where shear stress gradients are high compared to straight segments experiencing laminar flow. Regions of disturbed flow are usually present in angiogenic tissues, where physical barriers arise from an increase in vessel curvature, intersections and branching points.

In this study, we evaluated the effect of vascular flow on nanoparticle distribution *in vivo* using zebrafish embryos with highly angiogenic tissues and *in vitro* using cultured human endothelial cells exposed to physiologically relevant shear stress conditions. Computational fluid dynamics was used to determine flow pattern and shear stress profiles in the zebrafish vessels.

Methods

Transgenic zebrafish embryos, expressing green fluorescent protein in endothelial cells, were injected with 2-4nL of 2% (w/v) 200 nm carboxylate-coated FluoSpheres nanoparticle solution. Confocal images of zebrafish dorsal plexus vasculature were collected to develop the 3D model of the vessels using Simpleware®. Line scans were also obtained for each vessel to determine the blood flow velocity. For this, a cross-correlation particle image velocimetry technique was employed to determine the red blood cells displacements. Flow inside the vessels was simulated using computational fluid dynamics software Ansys Fluent. The profiles for shear stress and velocity, as well as the streamlines were obtained. For the *in vitro* experiments, cultured human umbilical vein endothelial cells were exposed to nanoparticle FluoSpheres using a parallel plate flow chamber with a step and flow conditions that mimic the *in vivo* shear stress. Nanoparticle accumulation for both *in vivo* and *in vitro* models was assessed using confocal laser scanning microscopy.

Results

Nanoparticle accumulation was higher in the caudal tail plexus than in the dorsal aorta. The dorsal aorta is a straight vessel with laminar flow of average velocity 1024±245μm/s (n≥3 fish). The caudal tail plexus is a system of venous vessels with high branching areas, large gradients of shear stress and flow disturbances. Average blood flow velocity for the caudal vein was 517±229 μm/s. Highest nanoparticle localization was observed in areas of disturbed flow such as branch points where flow is disturbed due to splitting or merging of streams, and immediately downstream of bumps and curves in the vessel. *In vitro* experiments also showed variations of nanoparticle accumulation with shear stress and disturbed flow.

Conclusions

The localization of nanoparticles in the bloodstream is affected by fluid flow profiles and shear stress forces. Regions with disturbed flow and low shear stress had a higher accumulation of FluoSpheres. Understanding the effect of vascular flow on nanoparticle distribution is important for the prediction of drug delivery efficacy and toxicity.

References:

[1]Fukumura et al. *Microcirculation* 17.3 (2010): 206–225.

[2]Samuel et al. *Int.J. of Nanomedicine* 7 (2012): 2943–2956

Hypoxia and reduced cerebral blood flow in multiple sclerosis are detected using combined MRI and near-infrared spectroscopy

Nabeela Nathoo*, Runze Yang*, Filomeno Cortese, Scott E. Jarvis, Jeff F. Dunn
Cumming School of Medicine, University of Calgary, 3330 Hospital Drive NW, Calgary, Alberta, T2N 4N1
*These authors contributed equally

Introduction

Multiple sclerosis (MS) is a neurological condition characterized by chronic inflammation, demyelination and axonal loss. The prevalence of MS in Alberta is one of the highest in the world, with 1 in every 300 people being afflicted with the disease. Many factors contribute to the pathophysiology of MS, including hypoxia. Near-infrared spectroscopy (NIRS) is a non-invasive method that uses the near-infrared region of the electromagnetic spectrum (~700nm to 2500nm). NIRS can used to measure oxyhemoglobin and deoxyhemoglobin, thereby providing a way of estimating brain oxygenation. In this study, we combined magnetic resonance imaging (MRI) (to assess cerebral blood flow, CBF) with NIRS (to assess microvascular oxygen saturation) simultaneously in MS patients and controls. We hypothesized that CBF and oxygen saturation would be reduced in MS patients due to hypoxia.

Methods

MS patients (four relapsing-remitting, one secondary-progressive, one primary-progressive, one progressive-relapsing) and six healthy controls underwent simultaneous MRI-NIRS. MRI was carried out with a 3T GE Discovery MR750 console and an HNS head coil. Left frontal cortical CBF was measured using pulsed continuous arterial spin labeling [1] (TR=4813ms, TE=11.1ms, FA=111, FOV=128x128, slice thickness=5mm). NIRS data was collected using a frequency domain system (ISS) which quantified hemoglobin concentrations and subsequently, absolute microvascular brain tissue oxygenation. Vitamin E capsules were placed besides the source and detector on the NIRS probe to indicate the brain area that NIRS was measuring. Groups were compared using t-tests with significance set at $p<0.05$.

Results

Of note, the NIRS probe was not found to interfere with the MRI. When all MS patients were combined into one group (n=7), oxygen saturation was not significantly reduced in MS compared to healthy controls ($p=0.12$). However, when comparing only RRMS patients (n=4) with healthy controls, it was found that RRMS patients had significantly decreased oxygen saturation compared to healthy controls ($p<0.01$). Oxygen saturation for other subtypes of MS (n=3) was not significantly reduced compared to healthy controls ($p=1.00$). CBF was not significantly reduced in all MS patients combined (n=7) compared to healthy controls ($p=0.06$) nor for only RRMS patients (n=4) ($p=0.27$). However, the other subtypes of MS (n=3), when grouped together, showed significantly reduced CBF compared to healthy controls ($p<0.05$).

Conclusions

In healthy individuals with intact neurovascular coupling, as CBF increases, blood oxygenation should increase as well [2]; this is consistent with what we observed for healthy controls in our study. However, in MS patients, the relationship between CBF and blood oxygenation is unclear and suggestive of impaired neurovascular coupling, which has been reported by others [3]. Combining MRI with NIRS enables for measuring the cerebral metabolic rate of oxygen ($CMRO_2$). As MRI and NIRS are non-invasive and do not use ionizing radiation, they can be used repeatedly in subjects. In summary, MRI and NIRS can be used to study abnormal neurovascular coupling in MS.

References

[1] Dai W *et al*. *MRM*. 2008; 60(6): 1488-1497.
[2] Leithner C, Royl G. *JCBFM* 2014; 34(1): 19-29.
[3] Ge Y *et al*. *Proc ISMRM* 2012; abstract 43.

Machine Learning based Classification of Acetabular Shape for Diagnosis of Infant Hip Dysplasia (DDH) from 3DUS

Abhilash Rakkunedeth Hareendranathan*, Dornoosh Zonoobi, Myles Mabee, Chad Diederichs, Kumaradevan Punithakumar, Michelle Noga and Jacob L. Jaremko
Servier Virtual Cardiac Centre, Mazankowski Alberta Heart Institute, Department of Radiology and Diagnostic Imaging, University of Alberta, Edmonton, Canada (correspondence e-mail: hareendr@ualberta.ca)

Introduction

Developmental dysplasia of the hip (DDH) is a congenital deformity which in severe cases leads to hip dislocation. Image aided diagnosis of DDH is partly based on Graf classification which quantifies the acetabular shape seen at two-dimensional ultrasound (2DUS). This approach relies upon 2D images to quantify a 3D structure (the acetabulum in this case), which leads to high inter-scan variance. 3DUS is a promising alternative for more reliable DDH diagnosis. However, manual quantification of acetabular shape from 3DUS is tedious. Here we use a semi-automated segmentation algorithm to generate 3D acetabular surface models and classify acetabular shape using machine learning (ML) based on geometric features derived from segmented 3D surface models.

Methods

We performed semi-automated segmentation [1] using graph search to produce 3D acetabular surface models and calculated geometric features including the Automatic Alpha Angle (AA), Acetabular Contact Angle (ACA), Kurtosis (K), Skewness (S) and Convexity (C). We tested the proposed technique on a dataset of 79 3DUS infant hip recordings (36 normal, 16 borderline, 27 dysplastic based on orthopedic surgeon assessment at time of scan).

Results

Surface models were generated rapidly (user time 46.2 seconds) via semi-automated segmentation, and visually closely correlated with the actual acetabular contour (as shown in Fig 1) with RMS error of less than 2 mm. A paired t-test on of feature values in normal, borderline and dysplastic categories showed statistically significant variation (p-value < 0.001) for Alpha Angle, Acetabular Contact Angle and Convexity. The Random forest classifier was 100% specific and 97.2% sensitive in classifying normal vs. dysplastic hips.

Conclusions

With semi-automated segmentation and geometric feature based classification, dysplastic hips can be rapidly and accurately detected from 3D ultrasound. The features calculated from the segmented model quantify two distinct aspects of dysplasia namely hip geometry and rounding. The proposed technique reduces the subjectivity of image aided DDH diagnosis and could be useful in clinical practice.

References

[1] R. H. Abhilash, M. Mabee, K. Punithakumar, M. Noga and J. L. Jaremko, "A Technique for Semi-Automatic Segmentation of Echogenic Structures in 3D Ultrasound, Applied to Infant Hip Dysplasia," International Journal of Computer Assisted Radiology and Surgery, 2015.

Figures

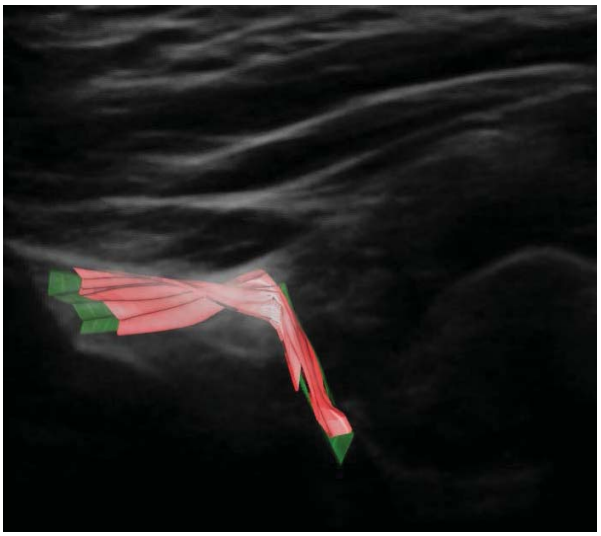

Fig 1: Automatically segmented (green) and manually segmented (red) acetabulum

DISTAL AND PROXIMAL FASCICLE LENGTH CHANGES IN ACTIVE AND PASSIVE HUMAN GASTROCNEMIUS MEDIALIS MUSCLE

Thomas Zhang[1], Rafael Fortuna[2], Walter Herzog[2]
[1]Biomedical Engineering Program, [2]Faculty of Kinesiology, University of Calgary

Introduction

Muscle fascicles define the overall muscle architecture. Because architecture is specific to individual muscles, knowing fascicle length changes for different contractile conditions is essential for understanding muscle function and force production. Ultrasound imaging allows for in vivo studies of fascicle lengths.

Muscle architecture is thought to vary along a given muscle [1]. However, fascicle lengths are typically measured at mid-belly and are assumed constant for a given muscle. The objective of this study was to test this assumption by measuring human gastrocnemius fascicle lengths at different locations along the muscle.

Methods

Fifteen healthy male subjects were tested (age: 25±4yrs; height: 177±7cm; weight: 69±9kg). Each subject was positioned in an isokinetic dynamometer with the right knee joint at full extension. The ankle joint was fixed at -10º dorsiflexion and 0, 10º, 20º, 30º, and 40º plantar flexion. Ankle torque and fascicle length were measured at rest (passive) and for maximum voluntary isometric plantar flexion (active) contractions, with an ultrasound probe close to the myotendinous junction of the gastrocnemius (distal). All testing was then repeated with the probe positioned close to the knee joint (proximal).

A three way ANOVA was used to assess fascicle length with the main factors: torque (passive and active), location (distal and proximal), and ankle joint angle (-10º, 0, 10º, 20°, 30º, 40º) at a level of significance of α=0.05. Bonferroni post-hoc testing was performed when indicated.

Results

Passive fascicle length was greater in more dorsiflexed positions than plantarflexed positions at distal and proximal locations ($P<0.001$). Fascicles shortened from passive to active states ($P<0.001$). Passive fascicle lengths were greater at 0º, 10º, and 20º plantar flexion at the distal compared to the proximal location ($P<0.05$; Fig. 1). Distal and proximal active fascicle lengths were the same at all ankle angles. (Fig 1)

Conclusions

Active fascicle lengths were the same at distal and proximal locations across all ankle angles. Passive fascicle lengths were longer distally compared to proximally, suggesting that the relative fascicle shortening from passive to active states depends on location along the muscle. Therefore, absolute sarcomere lengths must differ between distal and proximal fascicles, at least for some ankle angles. This result brings into question the long-held belief that sarcomere lengths in a given muscle are the same at all locations and independent of the instantaneous contractile conditions. Careful analysis is required for generalization of the current results across other muscles.

References

1. Kawakami et al. *J Appl Physiol.* **85**:398-404, 1998.

Figures

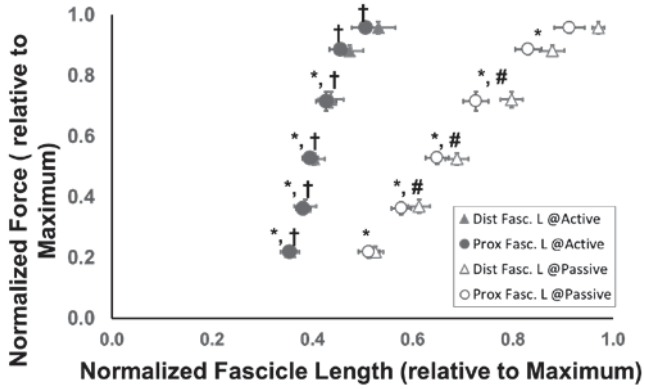

Figure 1: Mean (±1 SE) normalized force vs. normalized fascicle length for passive (filled) and active (empty); proximal (o) and distal (Δ) locations across ankle joint angles. Lengths at passive were given the same force as active to show shortening. '*': compares to-10º joint angle. '†': compares passive to active. '#': compares proximal and distal values.

Acknowledgments: NSERC of Canada, CRC Programme, The Killam Foundation, CIHR

Development of an Intraspinal Microstimulation Controller to Restore Walking after a Hemisection Spinal Cord Injury

Ashley N. Dalrymple, Dirk G. Everaert and Vivian K. Mushahwar
Neuroscience and Mental Health Institute, Division of Physical Medicine and Rehabilitation, Department of Medicine, Faculty of Medicine and Dentistry, University of Alberta, Edmonton, AB

Introduction

The overall goal of this project is to develop an intervention to improve mobility after neural injury or disease. Specifically, this work employs instraspinal microstimulation (ISMS) in an incomplete spinal cord injury (SCI) model. ISMS entails the implantation of ultrafine electrodes into the ventral horns of the lumbosacral enlargement of the spinal cord. The electrodes target specific motoneuron pools to achieve coordinated synergistic activations of flexor and extensor muscles of the legs [1,2]. ISMS produced stable walking in anaesthetized and completely spinalized cats [2,3], suggesting that it may be a viable clinical method for restoring walking in people with paralysis. The focus of this work is to develop adaptable control strategies to accommodate variable residual motor function after an incomplete SCI. The initial controller is tested in a hemisection SCI model, which results in motor loss in one limb, leaving the contralateral limb motor-intact.

Methods

Four pilot experiments were conducted to test the efficacy of the controller designed for a hemisection SCI. To achieve rigorous testing of the control strategies developed for this model, the cats had an intact spinal cord, and the stimulation was applied under anaesthesia. The motor-intact limb after a hemisection injury is replicated by an experimenter manually moving one hind-limb through the states of the gait cycle over a moving treadmill belt. Force and angular velocity information is acquired using external sensors. This information is relayed to the controller in real time and compared to experimenter-determined threshold values in order to distinguish the states of the gait cycle (F, E1, E2, E3). Once the controller determines the limb's current state in the gait cycle, it sends stimulation commands such that the other hind-limb (representing the limb affected by the hemisection SCI) is in the opposite state of the gait cycle. This type of oppositional limb movements is the foundation for walking.

Results

Preliminary results show that the controller successfully detects the individual states of the gait cycle based on sensor information and thresholds. Oppositional movements were successfully achieved based on this real-time sensory feedback, and was adaptable to different walking speeds. Improvement in setting threshold values is needed to more accurately detect the onsets of the states and ensure sufficient ground reaction forces are achieved to retain body-weight support. Safety rules were also implemented to test the controller's ability to adapt to fatigue and loss of weight support due to hyper-extension of the limb. These rules were successfully detected by the controller using the sensor information, and the controller adapted the stimulation amplitude accordingly. Minor adjustments are needed to improve the responses to the triggering of the safety rules.

Conclusions

This work demonstrates that the states of the gait cycle can be successfully detected using as little as two sensors in order to restore walking in a hemisection SCI model. The walking achieved can also be improved in real-time using safety rules. Future work includes testing this controller in an animal with a chronic hemisection SCI.

References

[1]V. K. Mushahwar and K. W. Horch, "Muscle recruitment through electrical stimulation of the lumbo-sacral spinal cord", *IEEE Trans on Rehab Engg*, vol.8, pp.22-29, 2000.

[2]R. Saigal, C. Renzi, and V. K. Mushahwar, "Intraspinal microstimulation generates functional movements after spinal cord injury", *IEEE Trans on Neural Syst and Rehab Engg*,vol.12,pp.430-40, 2004.

[3]B. J. Holinski, K. A. Mazurek, D. G. Everaert, R. B. Stein, and V. K. Mushahwar, "Restoring stepping after spinal cord injury using intraspinal microstimulation and novel control strategies", *Conf. Proc. IEEE Engg in Med and Bio Soc.* ,pp. 5798-5801, 2011.

Using frequency domain near-infrared spectroscopy to measure resting state functional activity

Duszynski, C.[1,2,3,4], Sewell, L.[1,2,3,4], and J.F. Dunn[1,2,3,4]
[1]Department of Neuroscience, [2]Hotchkiss Brain Institute, [3]Cummings School of Medicine, [4]University of Calgary

Introduction

The current diagnostic protocol for mild Traumatic Brain Injury (mTBI) is primarily symptom-based expert consensus with a lack of quantifiable measures of concussion symptoms. Functional MRI (fMRI) and Diffuse Tensor Imaging (DTI) have proven to be useful in diagnosing Traumatic Brain Injury (TBI), however, these techniques are often too expensive and inaccessible to be an effective diagnostic modality for concussion.

Functional Near-Infrared Spectroscopy (fNIRS) is a relatively inexpensive, easily accessible, and non-invasive optical imaging technique capable of detecting levels of oxy-hemoglobin (HbO) and deoxy-hemoglobin (HbR) at the cortical surface of the brain[1]. Neuronal activation is accompanied by an increase in localized HbO that can be measured using fNIRS[2], making fNIRS a possible alternative to fMRI for assessment of brain injury.

We showed previously that regional functional communication was impaired in patients with long-term symptoms of concussion[3].

This mapping system is also too large for regular use. Smaller NIRS systems tend to be limited to low rates of data acquisition. Previously we reported that there were changes in low frequency (in the range of 0.04-.10Hz) coherence between the left and right side of the brain[3]. It is possible to measure such low frequencies with many types of NIRS systems.

This study applies a low frequency NIRS system to determine if it can be used to detect functional interhemispheric connectivity in normal controls.

Methods

We used the ISS OxiplexTS Frequency Domain Near-Infrared Tissue Oximeter (fdNIRS) model 99200 to record data from 6 healthy adult controls. A probe was placed on either side of the subjects' forehead, centered approximately 5 cm lateral of midline and 3 cm superior to the supraorbital process. Control subjects were asked to rest and remain still for 5 minutes while baseline measures were recorded. Coherence analysis of left/right prefrontal cortex was done using in house software[4].

Results

The fdNIRS system can quantify absolute values for oxy- deoxy and total Hb. Coherence data are being analyzed and will be presented.

	[HbO]	[HbR]
Left Hemisphere	37.2 ± 6.6	18.6 ± 3.7
Right Hemisphere	43.2 ± 3.6	19.4 ± 4.0

Table 1. Oxy- and deoxy-hemoglobin concentrations *fdNIRS measured values from healthy controls. (means±S.D., n=6)*

Discussion and Conclusions

A decrease in interhemispheric cortical communication in concussed patients during motor activation has been reported from our lab[3]. This abstract will discuss different types of NIRS measurement systems for application to human studies, and will determine if the ISS oxyplex, a small portable fdNIRS system, can be used to detect interhemispheric communication.

References

1. Scholkmann, F., et al., Neuroimage, 2014. **85 Pt 1**
2. Leon-Carrion, J., et al., Behav Brain Res, 2008. **193**(2)
3. Urban, K.J., et al., J Neurotrauma, 2015. **32**(11)
4. Varshney, V.P., et al., J Europ Opt Soc Rap Public, 2012. **7**

CHARACTERIAZING AND OPTIMIZING PSEUDOISLETS

Yang Yu, PhD Candidate, Biomedical Engineering Graduate Program, University of Calgary
3330 Hospital Dr. NW, Calgary

Introduction

Islets transplantation is a promising approach to the treatment of Type I Diabetes[1]. However, a major clinical limitation for current islet transplantation is the inefficient survival and engraftment in the immediate post-transplant period.[2] One reason is likely that the size of the native islets is too large for sufficient oxygen and nutrition delivery in avascular condition immediately after transplant. Quantitative modeling of oxygen delivery within islets shows significant benefits to smaller islets[3], and consistent with this concept, smaller human islets have been reported to perform better than larger ones in a clinical setting[4]. Based on our previous experience in microtissue formation, I hypothesize that there exists an optimal aggregate size, at which islet cell aggregates will exhibit significantly improved viability and insulin secretion capacity, due at least in part to improved oxygen transport properties. I further hypothesize that the pseudoislet formation process can be modulated by soluble signals allowing further increases in viability and function. Subsequently, the optimal outcome from in vitro experiments will be validated in vivo. I hypothesize that in vitro results will be generally predictive of and consistent with in vivo survival and function.

Methods

The Aggrewell system is used to re-aggregate the native islets to form smaller pseudoislets and centrifugation is employed to accelerate aggregation and enhance viability. Re-aggregated islet cells were cultured in supplemented CMRL-1066 for 48hrs in order to form pseudoislets. Insulin production capacity is tested in Glucose Stimulated Insulin Secretion (GSIS) assay at multiple time points. Design of experiments (DoE) is used for design and analysis of in vitro optimization.

Results

In the recent preliminary results, I successfully re-aggregated the native islet cells to formed pseudoislets in our centrifugation-aided microwell system by using neonatal porcine islets(NPI) and human donor islets respectively. The direct comparison showed that the pseudoislets significantly outperformed the native islets after 48-hour incubation, exhibiting a 2.8 fold increase in terms of insulin secretion per input cell basis ($p<0.02$). This effect is further improved by an additional 1.6- and 2.5-fold increase when performing the experiment in the presence of a ROCK inhibitor Y27632, or the apoptosis inhibitor Emricasan ($p<0.05$; $p<0.01$). In another independent experiment, direct comparison with native islets shows a 2.7- and 3.7-fold increase in ER ($p<0.003$) with Emricasan or Emricasan plus Y27632. The RSM model generated from a two-factorial (size and ibuprofen concentration) pilot experiment recently gives a R-square of 0.897, wich also indicating a relatively good fit.

Conclusions

Overall the new approach to the generation of pseudoislets is feasible. If consistent results are obtained in vivo this would result in at least a 3.7-fold increase in the number of patients treatable from the current limited supply of donor islets. Moreover, as approximately 50% of islet isolations yield quantities that are insufficient for therapeutic applications, a successful clinical translation of the proposed research would also effectively expand the human islet donor pool, mitigating the current critical islet shortage for patients awaiting transplantation.

References

1.The prevalence and costs of diabetes facts. (2015).
2.Effect of intensive diabetes treatment on the development and progression of long-term complications in adolescents with insulin-dependent diabetes mellitus: Diabetes Control and Complications Trial. DCCT Group. *J. Pediatr.* 125, 177–188 (1994).
3. Oxygen consumption and diffusion in assemblages of respiring spheres: Performance enhancement of a bioartificial pancreas. Johnson, A. S. *et al. Chemical Engineering Science* 64, 4470–4487 (2009).
4. FEM-based oxygen consumption and cell viability models for avascular pancreatic islets. Buchwald, P. *Theoretical Biology and Medical Modelling* 6, 5 (2009).

Evaluation of two transfixation cast constructs in horse forelimbs using finite element modeling

Arjmand H[1], Thomas K[3], Burnett W[2], Carmalt JL[3], Johnston, JD[1,2]
[1] Department of Mechanical Engineering, University of Saskatchewan, Saskatoon, SK, Canada
[2] Division of Biomedical Engineering, University of Saskatchewan, Saskatoon, SK, Canada
[3] Western College of Veterinary Medicine, University of Saskatchewan, Saskatoon, SK, Canada

Introduction: Pin loosening, secondary infection, and necrosis at the bone-pin-interface are complications related to equine transfixation cast surgery. Using a finite element (FE) model validated against experimental results, the objective of this study was to evaluate load transfer, displacement, and bone strain at the bone-pin-interface and adjacent to the fracture site in a 2-pin and 4-pin transfixation cast construct.

Methods: *Model Geometry*: CT images of a cast horse forelimb were used to derive simplified circular geometry representing the (pinned) cannon bone and cast. Pins (2x6.3mm diameter (2-pin construct), 4x4.8mm diameter (4-pin construct)) were added as per established surgical approaches.

Material Properties: Isotropic, linearly-elastic materials were used for modeling cortical bone (E=20GPa, ν=0.3), cast (E=3.4GPa, ν=0.3), and pins (E=190GPa, ν=0.305). A single 'effective' E was used to model the structures distal to the fetlock joint (E=500MPa, ν=0.3), derived iteratively until FE strain matched experimental strain.

Loading: A 7.5kN load was applied to the proximal cannon bone, mimicking walking.

Results: The 2-pin construct had more load transferred to the bone (+6.4%), higher displacement (lower stiffness; +9.5%), higher strain at the bone-pin-interface (+15%) and higher strain adjacent to the fracture site (+22%). For both constructs, strain adjacent to the fracture site was in the physiological range.

Conclusion: The 4-pin construct appears to be more effective at off-loading the fractured bone, reducing pain and accelerating healing. High displacement and strain with the 2-pin construct could explain observed bone necrosis.

Biomechanical Effects of Re-Injury in a Rabbit Medial Collateral Ligament Model

Johnathan L. Sevick[1,3], Bryan J. Heard[3], Cyril B. Frank[3], Nigel G. Shrive[2,3], Gail M. Thornton[2,3]
[1]Biomedical Engineering Graduate Program; [2]Civil Engineering, Schulich School of Engineering; [3]McCaig Institute for Bone and Joint Health; University of Calgary

Introduction

Re-injury to ligaments of the knee is a prevalent clinical problem in athletic populations [1]. While significant effort has been devoted to understanding the healing process and the mechanical behaviour of ligaments sustaining a single injury, little effort has been made to understand the effect of re-injury on the mechanical properties of the healing ligament. The objective of this study was to partially fill this knowledge gap by comparing the biomechanics of re-injured to injured ligaments. Evaluating noninferiority, the null hypothesis was that re-injured ligaments would be mechanically inferior to injured ligaments.

Methods

The medial collateral ligaments (MCLs) of 2 groups of rabbits (each n=4) were used. For both Group A and B, the MCLs of right hindlimbs were transected surgically and left hindlimbs underwent sham surgery. One week after this first surgery, the left MCLs in both Group A and B were transected; the right MCLs in Group A were transected a second time; and the right MCLs in Group B underwent gap surgery. After a 5-6 week healing period, the re-injured (right) and injured (left) MCLs were tested mechanically. MCL cross-sectional areas (CSA) and lengths were measured. The ligaments were subjected to cyclic creep testing (3600 cycles at 1 Hz from 0.1 N to 20 N) followed by recovery before being elongated to failure (20 mm/min).

Equivalence/noninferiority tests comparing re-injured to injured MCLs (difference between right and left) were performed to establish the effect of re-injury on cyclic creep strain, failure load, CSA and failure stress. The equivalence margins were based on published data [2].

Results

The failure loads of Group A and B ligaments were determined to be statistically equivalent. Non-inferiority was established in Group A for cyclic creep strain, CSA and failure stress (Fig. 1) (comparing transection re-injury to transection injury). In Group B, cyclic creep strain and failure stress (Fig. 1) were shown to be potentially inferior (comparing gap re-injury to transection injury). CSA for Group B did not yield an interpretable result.

Conclusions

For the specific re-injury model of Group A (early dual transection), re-injured MCLs were not mechanically inferior to their singly injured counterparts. Group B re-injured MCLs, on the other hand, were potentially mechanically inferior.

The initial healing resulting from the first transection injury may not have been erased by the second transection re-injury, giving these ligaments the resources to heal more effectively than those being transected for the first time. Conversely, gap surgery likely eliminated a significant portion of initial healing products in re-injured ligaments, thereby reducing their capacity for healing and accounting for the potential inferiority observed in Group B. Further research is required to elucidate the characteristics responsible for the outcomes.

References

[1] Price, RJ et al., Br J Sports Med 2004, 38:466–471.
[2] Majima, T et al., J Orthop Sci 2006, 11:272–277.

Figures

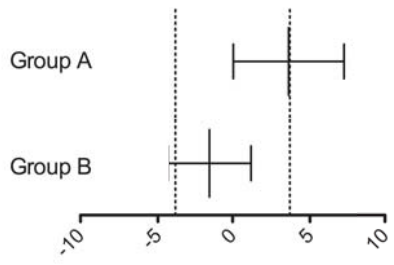

Fig. 1 Failure stress equivalence/noninferiority test. Difference between right (re-injured) and left (injured) shown on the x-axis (MPa). Data shown as mean +/- 90% confidence interval. Dashed lines indicate equivalence margin.

Improving the Accuracy of fMRI Optical Neuritis Markers

E. Shahrabi Farahani[1], P. Adibpour[1] and M. R. Smith[1,2]
[1]Electrical and Computer Engineering, [2]Radiology, University of Calgary, Alberta, Canada

Introduction

Optical Neuritis (ON) impacts the properties of pathways between regions of interest (ROI) in the brain. We generated markers to diagnosis ON progression from a time series of functional magnetic resonance images (fMRI) [1]. fMRI's temporal resolution is obtained by performing a discrete Fourier transform (DFT) reconstruction on truncated (finite length) k-space data sets. Low-pass filtering is needed to remove ringing produced by k-space truncation leading to lower fMRI spatial resolution and an undesirable loss in ON marker accuracy. We present a new DFT reconstruction approach that removes the truncation artifacts without the resolution destroying low-pass filtering.

Methods

Fig. A represents cross-sections of a 1024 x 1024 high resolution (HR) DFT reconstruction of narrow anatomical features placed near broad anatomical features. Fig. B is a low resolution image from DFT reconstruction of a truncated 64 x 64 k-space data set typical of fMRI. The truncation artifacts in Fig. B can be removed by low-pass filtering resulting in blurring, Fig. C.

Re-examination of Fig. B shows that the lower image was unnecessarily blurred when image-wide low-pass filtering was applied to remove ringing. We have identified that the field of view (FOV) position of a narrow feature determines whether its truncation distortions impact the accuracy of the ON markers evaluated from nearby ROI. The Fourier shift property (FSP) states "*A k-space signal multiplied by a complex sinusoid will cause a image position shift*". Our Fourier shift manipulated (FSM) DFT mathematically modifies the FOV position to a non-artifact producing position.

Results

Application of a low-pass k-space filter, Fig. C, to remove the artifacts in the upper cross-section in Fig. B unnecessarily destroys the available spatial resolution present in the lower cross-section. Our preliminary FSM approach involves a (1) row-by-row examination of an fMRI image to determine the presence of truncation artifacts. (2) A series of FSP operations are then applied to generate multiple images where k-space manipulation places HR features in a FOV position that does not produce image artifacts. (3) The undistorted rows from the various images are then combined to produce a FSM-DFT reconstruction, Fig. D..

Our current FSM-DFT method involves pixel duplicating each image row followed by shifting to compensate for the effective FOV changes displayed by the FSM image series. We are currently investigating whether ON marker accuracy increases or decreases following smoothing of the "jagged edges", Fig. D, that FSM-DFT reconstruction shares with other display methods involving pixel duplication.

Conclusions

We have shown how Fourier Shift Modulation can promote the resolution level of fMRI images from truncated k-space data. An automated FSM process is required to handle rows with multiple HR features.

References

1) S. H. Choudry et al. 2014 Joint ACTRIMS – ECTRIMS Meeting, Boston, U. S. A, 2014

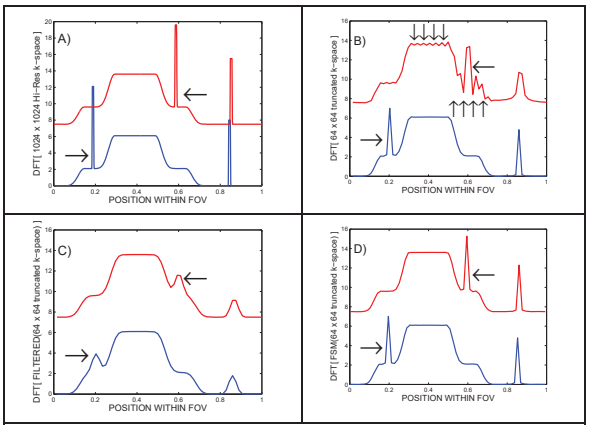

Fig. DFT reconstructions from (A) High resolution, (B) Truncated, (C) Filtered, (D) Fourier Shift Modulated k-space data

A new method for quantitative assessment of the knee using high resolution peripheral quantitative computed tomography

Andres Kroker [12], Sarah Manske [12], Ying Zhu [12], Rhamona Barber [3], Nicholas Mohtadi [3], Steven Boyd [12]
1 Department of Radiology, Cumming School of Medicine, 2 McCaig Institute for Bone of Joint Health, 3 Acute Knee Injury Clinic, Sport Medicine Centre, Faculty of Kinesiology, University of Calgary

Introduction

Anterior cruciate ligament (ACL) tears are a common knee injury, particularly for sports such as skiing, that increase the risk of developing osteoarthritis (OA). While the sequence of events leading to OA is poorly understood, evidence suggests that rapid changes in bone mineral density (BMD) in the subchondral bone in the injured knee after the ACL tear may play a role. However, how these changes affect the bone microarchitecture, and thus the bone biomechanics, is not understood, largely because clinical imaging modalities lack the required resolution. High resolution peripheral quantitative computer tomography (HR-pQCT), a novel human *in vivo* micro computed tomography system, is able to measure bone microarchitecture. This study aims to develop an approach to use HR-pQCT to assess microarchitecture of the bones in the human knee for the first time.

Methods

Thirty-five subjects with reconstructed ACL tears that occurred five years prior were imaged with HR-pQCT at a resolution of 61 µm. Approximately 6 cm (1008 slices) of the knee were acquired around the joint gap, with two cm of the proximal tibia and four cm of the distal femur being covered. The weight bearing regions of both tibia and femur were analyzed. Each bone was divided into a medial and lateral plateau/condyle. The subchondral bone plate in that region was isolated and its thickness, porosity, and BMD were measured. The trabecular bone in each compartment was analyzed in three different depth layers (0-2.5mm, 2.5-5mm, 5-7.5mm) and trabecular number, thickness, and separation were measured as well as BMD of the bone layer. The scanner was not designed for scanning the knee, thus customization of a protocol, including the design and manufacture of a custom supporting brace was required.

Results

The knee stabilizing cast centered the knee in the scanner reliably for all 35 subjects scanned. Maximal knee circumference fitting into the scanner was 44cm. Scans took approximately 22 minutes per knee, but the new knee cast minimized the occurrence of motion artifacts. BMD of the subchondral bone plate was higher than the trabecular bone further from the joint surface, and decreased with depth.

Conclusions

We performed the first *in vivo* high resolution bone microarchitecture measurements of the knee. Are protocol permits trabecular and cortical bone microarchitectural parameters to be measured at a range of depths from the joint surface at the distal femur and proximal tibia. Ongoing work includes measuring the differences between lateral and medial bone compartments in the cohort, comparing ACL deficient and healthy control knees. We expect these findings to provide insight into bone changes that may lead to increased risk of developing OA.

References

1. Lohmander 2004; 2. Øiestad 2009; 3. Lui 2012; 4. Sievanen 1994; 5. Rittweger 2006; 6 Johnston 2009.

Figures

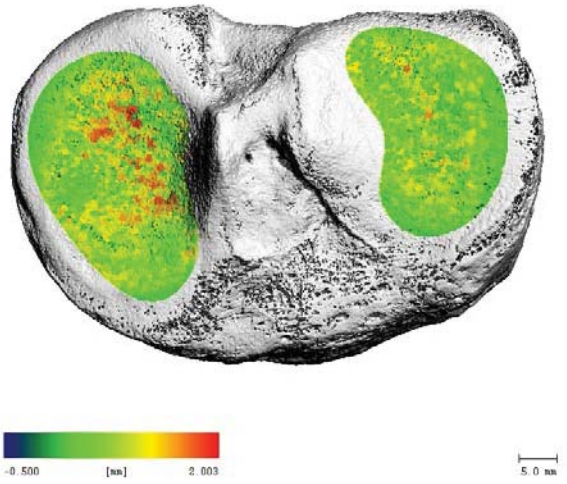

Figure 1: Proximal tibia (left knee) with subchondral bone thickness of the medial and lateral tibial plateau.

Diffuse Grey Matter Susceptibility Changes for Detecting Smaller Microbleeds in Cerebral Amyloid Angiopathy

Christopher M O'Neill, Cheryl R McCreary, PhD; Eric E Smith, MD, MPH; Richard Frayne, PhD
Seaman Family MR Research Centre, Departments of Radiology and Clinical Neurosciences, Hotchkiss Brain Institute, University of Calgary, Calgary, AB, CANADA

Introduction

Cerebral amyloid angiopathy (CAA) is characterized by the deposition of β-amyloid protein in the small arteries and arterioles of the brain, resulting in damage to the blood brain barrier and greater potential for hemorrhage (Rensink *et al.,* 2003). Cerebral microbleeds are localized hemorrhages, which result in the eventual breakdown of the red blood cells into deposits of hemosiderin and ferritin protein (Walker *et al.*, 2004). Iron-sensitive magnetic resonance (MR) imaging sequences detect these deposits, typically, as small signal hypointensities, and have been widely used for identifying suspected cerebral microbleeds. Autopsy-based pathological studies have found microbleeds as small as 0.05 mm (Cullen *et al.*, 2005); smaller than can be resolved with standard MR sequences. Given the current spatial resolution limitations of MR imaging, we attempted to determine if it is possible to use an indirect method based on normalized signal intensity in susceptibility-weighted MR images to detect the presence of smaller microbleeds.

Methods

This study used data collected as part of an ongoing cohort study, Functional Assessment of Vascular Reactivity (FAVR). Subjects were diagnosed as probable CAA according to the validated Boston Criteria (Knudson *et al.,* 2001). Twenty-eight CAA (mean age ± SE: 74.1 ± 1.3 years) and 24 younger healthy control (HC) participants (63.1 ± 2.1 years, $p<0.01$) were imaged on a 3 T MR scanner (MR750, GE Healthcare, Waukesha, WI). T1-weighted structural images, T2*-weighted and susceptibility-weighted, phase filtered images were acquired. The Montreal Neurological Institute 152 1-mm brain atlas and FSL (Jenkinson *et al*., 2012) was used to segment brain regions and measure the signal intensity of normal appearing grey matter in the frontal, parietal, temporal, and occipital lobes. Overt microbleeds were excluded from the four lobe-specific regional cortical masks (Figure 1). These regions were then normalized to the signal of the CSF in the lateral ventricles of the brain, to enable comparisons between subjects. Histograms for the whole brain and each region were analyzed, and compared between CAA and control subjects. Multivariate analysis of variance with age as a covariate, was used to compare the regional normalized signal intensities of the normal appearing grey matter between CAA and HC groups. Significance was set at $p<0.05$.

Results

Over the whole brain there were no significant differences in the mean between CAA and control subjects ($p=0.35$). Comparisons within specific regions found no significant difference between CAA and control subjects ($p>0.10$) A visual inspection of the histograms suggested no differences between groups. Analysis of the skew and kurtosis of the distributions yielded no significant results ($p>0.5$).

Conclusions

Given the moderate sample size, it seems unlikely that this indirect method is able to detect the presence of smaller microbleeds that are not directly visible on MR imaging. A larger study with better age-matched controls is needed to confirm this finding.

References

Cullen K.M., Kocsi Z., Stone J. (2005). *JCBFM*. 1656–1667.

Jenkinson M., Beckmann C.F., Behrens T.E., Woolrich M.W., Smith S.M. (2012). *NeuroImage*. 62:782-90.

Knudsen K.A., Rosand J., Karluk D., Greenberg S.M. (2001). *Neurology*. 56(4); 537-539.

Rensink A.A.M., Waal R.M.W., Kremer B., Verbeek M.M. (2003). *BRR*. 43; 207-223.

Walker D.A., Broderick D.F., Kotsenas A.L., Rubino F.A. (2004). *AJR*. 182; 1547-1550.

Figures

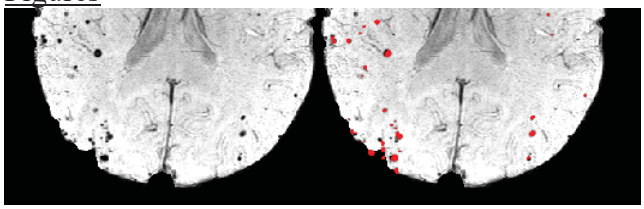

Figure 1: Mask overlay illustrating exclusion of overt microbleeds.

Fast Computational Scheme for Biological Tissues with Statistical Fibre Orientation

Kotaybah Hashamoun[1], Alfio Grillo[2], Salvatore Federico[3]
[1] Graduate Programme in Mechanical Engineering, The University of Calgary, Canada
[2] DiSMA "G. Lagrange", Politecnico di Torino, Italy
[3] Department of Mechanical and Manufacturing Engineering, The University of Calgary, Canada

Introduction

Biological tissues are highly non-linear, multi-phasic, inhomogeneous, anisotropic composite materials, and a good part of their complexity can be ascribed to the presence and spatial arrangement of the collagen fibres, which has in general a statistical nature. The contribution of the fibres to the overall tissue properties can be estimated by taking the directional average of the effect of the fibres over the set of all possible directions in space [1]. Except for the particular case of fibre constitutive functions that are polynomial in the structure tensor $\boldsymbol{A} = \boldsymbol{M} \otimes \boldsymbol{M}$ ($\boldsymbol{M}$ is the fibre direction), the averaging integrals have to be numerically evaluated at each deformation increment, which has a high computational cost.
We propose to approximate a fibre constitutive function by exploiting the fact that polynomials are integrable "once-and-for-all", so that only a single integration is required. We propose two methods based on Taylor expansion, and one generalising the method proposed by Gasser et al. [2]. Here, we confine ourselves to the case of elasticity, in which the elastic potential and the stress need to be approximated.

Methods

We propose three methods:
STEX: Taylor expansion in the structure tensor $\boldsymbol{A} = \boldsymbol{M} \otimes \boldsymbol{M}$, about a value $\boldsymbol{A}^* = \boldsymbol{M}^* \otimes \boldsymbol{M}^*$, with $\boldsymbol{M}^*$ a given direction;
INEX: Taylor expansion in the fourth invariant of the deformation, $I_4 = \boldsymbol{C} : \boldsymbol{A}$, where $\boldsymbol{C}$ is the right Cauchy-Green deformation, about the value $I_{40} = 1$, which is independent of direction;
PARG: integration of the outermost polynomial argument, in a potential that is given by a certain function f of a polynomial in the structure tensor $\boldsymbol{A} = \boldsymbol{M} \otimes \boldsymbol{M}$.

Results

We consider biaxial tensile test experimental setting, in which a square, bi-dimensional soft tissue sample is stretched in two orthogonal directions. An exponential elastic potential is used, and a von-Mises distribution function describes the fibre orientation. We compare our three methods with that of [2] (GOH method) and the step-by-step integration with spherical designs (FESD method). In the figure below, the normalised stretch-strain curve in direction 1 is plotted for an initially isotropic fibre distribution.

Conclusions

A convenient method to approximate the contribution of statistically oriented fibres should be independent of the particular fibre arrangement. Our INEX method, which is invariant-based rather than direction-based, gave by far the most accurate approximation of the "exact" results obtained by means of an integration performed at each increment of deformation.

References

[1] Federico S, Herzog W, 2008, *J. Biomech.*, 41:3309-3313
[2] Gasser TC, Ogden RW, Holzapfel G, 2006. *J. Roy. Soc. Interface*, 3:15-35

Figure

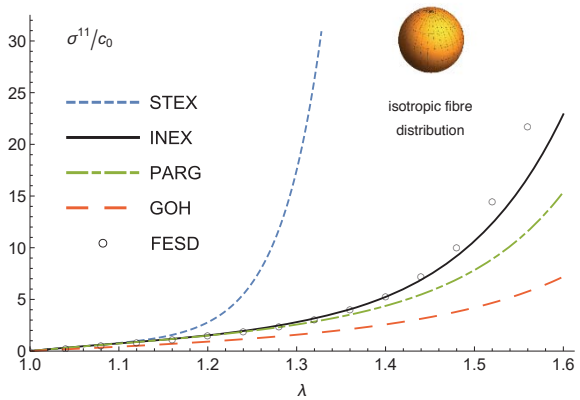

Spontaneous articular cartilage regeneration after injury in p21 null mice

Jablonski CL[1], Leonard C[2], Tailor P[2], Stevens K[3], Colarusso P[3], Krawetz RJ[2]
[1]Faculty of Biomedical Engineering, University of Calgary, Canada [2]Faculty of Medicine, University of Calgary, Canada, [3]Live Cell Imaging Facility, Snyder Institute for Chronic Diseases, University of Calgary, Canada

Introduction

The inability of articular cartilage to undergo endogenous repair is partially attributed to the avascularity of cartilage tissue, which prevents the influx of stem/progenitor cells to the site of injury [1–3]. Mesenchymal stem cells (MSCs) are unique in their ability to self-renew or differentiate into chondrocytes (ie. cartilage cells) and migrate to injury sites [1]. Previous studies on C57BL/6 (control) and MRL/MpJ ("super-healer") mice have shown spontaneous articular cartilage regeneration in the "super-healer" mice [4,5] and further studies have determined that a mutation in the p21 gene – a major cell cycle regulator - is partly responsible for the resulting cartilage regeneration [6]. While the synovium (i.e. joint lining) and bone marrow are known to originate from a shared pool of progenitor cells during development [7], it is unknown if synovial MSCs contribute to cartilage repair in $p21^{-/-}$ mice. Since macrophages have also been demonstrated to play a significant role in the pathogenesis of OA [8], I will also examine if their recruitment to injured cartilage is modified in $p21^{-/-}$ mice.

Methods

Skeletally mature C57BL/6 and $p21^{-/-}$ mice will be used for all experiments. Histology/multi-color immunohistochemistry and multiphoton confocal imaging techniques will be used to (1) identify/quantify the cell type(s) involved in cartilage repair, and (2) characterize synovium inflammation. Data will be collected in both mouse strains before injury and 2 and 4 weeks after injury. In addition, flow cytometry and qPCR techniques will be used to isolate MSCs from the bone marrow and synovium for determining chondrogenic potential and cell cycle activity.

Preliminary Results

At 1hr post injury, MSCs are already present in/around defect area in MRL mice but not control mice (Figs. 1-2). Histology data indicates MRL mice are better than controls at restoring proteoglycan content after injury (Fig. 3). Multiphoton confocal imaging shows feasibility of tracking cells in real-time while visualizing AC and collagen within the bone (Fig. 4).

Conclusions

Multi-color immunohistochemistry demonstrates changes inMSCs and macrophages (data not shown) after injury in MRL 'super-healer' mice. This provides rationale to determine if p21 plays a role in the recruitment and activation of MSCs in this rare example of endogenous cartilage repair in mammals.

References

1. Ahmed N et al. (2007) Skeletal Radiol 36: 909–912. 2. Hunziker EB (2000) Biorheology 37: 163–164. 3. Kinner B et al. (2005) Adv Biochem Eng Biotechnol 94: 91–123. 4. Ward BD et al. (2008) Arth Rheum 58: 744–753. 5. Fitzgerald J et al. (2008) OA Cart 16: 1319–1326. 6. Bedelbaeva K et al. (2010) Proc Natl Acad Sci USA 107: 5845–5850. 7. Pacifici M et al. (2000) Connect Tissue Res 41: 175–184.

Figures

1. C57BL/6, 1hr post injury, stem cells

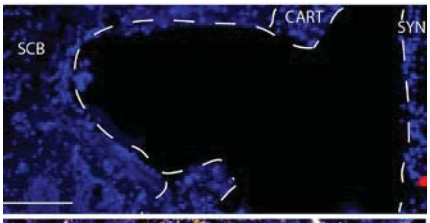

2. MRL/MpJ, 1hr post injury, stem cells

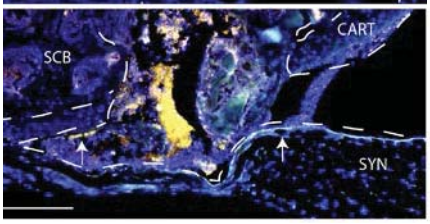

3.

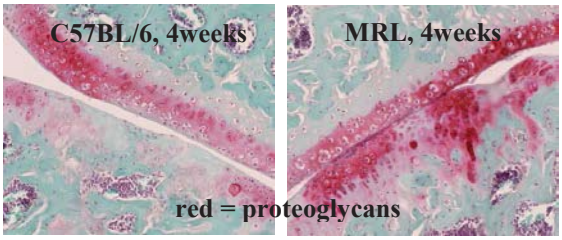

4. Multi-photon confocal image, C57BL/6, green = chondrocytes

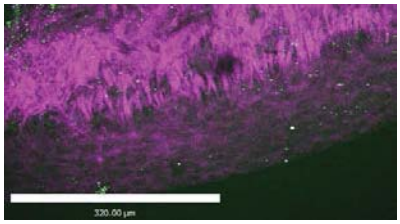

9.4T MRI Characterization of Experimental Demyelination and Remyelination of Mouse Spinal Cord Induced by Focal Injection of Lysolecithin

Dhaliwal R[1,2,3,4], Jenson S[1,3,4], Yong V.W.[1,3,4], Dunn JF [1,2,3,4]
[1]Hotchkiss Brain Institute, [2]Department of Radiology, [3]Cumming School of Medicine, [4]U. of Calgary

Introduction

Multiple Sclerosis (MS) is a chronic inflammatory and demyelinating disease of the central nervous system [1]. The next generation of therapeutics for MS will focus on combining immunomodulation with promotion of repair mechanisms to reduce demyelination and promote remyelination [2]. Sensitive and specific imaging methods are needed to detect response in animal models. One model involves direct injection of lysolecithin into the spinal cord white matter [3] causing demyelination followed by spontaneous remyelination. This project will use the ventral lysolecithin model to combine MRI methods sensitive to myelin and compare with histological results.

Methods

Female C57Bl/6 mice underwent a lysolecithin injection in the left ventral thoracic spinal cord [3]. Lysolecithin mice were perfusion fixed at days 7 and 14 (peak demyelination and partial remyelination respectively) post injection. Imaging was done ex-vivo with a 9.4T Bruker MRI and a homogeneous 35mm volume coil. FLASH and RARE – T2w scouts were used to locate lesions. Lesions were characterized using CPMG (multicomponent T2), diffusion weighted MRI, FLASH with off-resonance pulses (for quantitative magnetization transfer or qMT), and RARE-Variable TR sequences (for T1) were collected. Analysis included neurite orientation dispersion and density index (NODDI) [4]. Regions of interest (ROIs) around the lesion and contralateral to the lesion were used for demyelination and control data.

Results

7 days post lysolecithin injection lesions were clearly visible in the ventral white matter of spinal cord FLASH and RARE-T2 weighted images (Fig. 1). The mean T1 of the lesion site was significantly higher than the contralateral side ($p<0.05$). Preliminary qMT and multicomponent T2 data shows a trend towards a lower bound pool fraction (f) ($p=0.18$), longitudinal relaxation rate of the free pool ($p=0.09$), and myelin water fraction (MWF; $p=0.14$) at the lesion.

Conclusions

The increase in T1 at the lesion site indicates the loss of myelinated axons. T1 has previously been shown to have a strong negative correlation with the myelinated axon fraction [5]. The f from qMT is one of the strongest indicators for the loss of myelin [5] and MWF (T2) is known to correlate with myelin content [6]. A previous study using the dorsal spinal cord model of lysolecithin injury showed that MWF was not significantly changed at day 7 [7], likely due to myelin debris at the injury site [6, 7]. This is the first study combining a NODDI analysis with both qT2 and qMT. We will have an increased sample size to present, add additional time points, and will discuss the implications of each method for the detection of de- and remyelination.

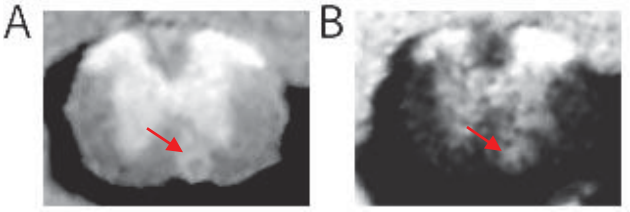

Fig. 1. High resolution FLASH (A) and RARE T2-weighted (B) image of mouse spinal cord 7 days post Lysolecithin injection. Lesion indicated by red arrows.

References

[1] Nathoo N, Yong VW, Dunn JF. *Neuroimage Clin.* **4**, 743-56 (2014)
[2] Keough MB, Yong VW. *Neurotherapeutics.* **10**, 44-45 (2013)
[3] Keough MB, Jenson SK, Yong VW. *JOVE.* (2015)
[4] Zhang H. et al. *NeuroImage*. **61**, 1000-16. (2012)
[5] Thiessen J et al. *NMR Biomed.* **26**, 1562-81. (2013)
[6] Kozlowski P. et al. *J Neurotrama*. **25**, 653-676 (2008)
[7] McCreary CR. et al. *NeuroImage.* **45** 1173-1182. (2009)

POSTER PRESENTATION ABSTRACTS

Determination of In-Vivo Human Dynamic Tibiofemoral Contact Mechanics

Jessica Küpper, Gregor Kuntze, Jillian Beveridge, Emily Been, Brodie Ritchie, Gulshan Sharma, Janet Ronsky
Mechanical and Manufacturing Engineering, University of Calgary, Calgary, AB, Canada

Introduction

Altered dynamic tibiofemoral (TF) cartilage contact mechanics are theorized to contribute to the high risk of post-traumatic osteoarthritis (PTOA) [1]. Combined high-speed Dual Fluoroscopy (DF) and 3T Magnetic Resonance (MR) imaging allows for non-invasive, in-vivo estimation of cartilage contact mechanics with high accuracy and precision. The goal of this PhD research is to advance understanding of what resultant contact mechanics estimates reveal about the interactions of aberrant movement / loading patterns, altered material properties and progressive cartilage damage. Accurate and precise determination of dynamic cartilage surface mechanics is critical. This pilot work quantified the sensitivity of a weighted centroid approach for cartilage-cartilage contact location determination on alterations of cartilage surface model type and density. The aim was to identify the minimum model complexities required for accurate centroid determination.

Methods

One 37-year-old anterior cruciate ligament deficient male volunteered for this ethics approved study. 3D models of the femur, tibia and TF cartilages were created in Amira (VSG, Germany) using MR images. Bone kinematics during walking (first 50% of stance) were recorded using DF (120Hz). 3D bone kinematics were reconstructed (Autoscoper, Brown University, USA) using undistorted and calibrated DF images. Cartilage contact mechanics were computed using apposing surface proximities. Bone transformations were applied to co-registered cartilage models. Cartilage deformation was quantified as the change in median proximity of all model faces within 4mm of the apposing surface. Contact location was quantified using a weighted centroid approach [2]. The sensitivity of contact mechanics to mesh density was tested using irregular and isotropic meshes. Face numbers were reduced at 10% increments. Median proximity and weighted centroid locations were calculated for every kinematics frame and compared to the same output computed using the original non-simplified model. A difference in computed contact mechanics of 0.05mm, the minimal detectible difference in displacement of this DF system [3], was deemed acceptable.

Results

Results of surface sensitivities are summarized in Table 1.

Conclusions

In-vivo contact mechanics estimates obtained using DF/MR were sensitive to both surface mesh type and complexity. Isometric meshes provided consistently lower errors and allowed for greater simplification compared to irregular sized triangle meshes. These results must be taken into consideration when modeling dynamic cartilage surface contact mechanics. Further work on the effects of cartilage model parameters will be conducted to assess changes in surface interactions throughout the support phase of gait to assess the effects of kinematics and kinetics abnormality on the morphology and biology of cartilage in health and PTOA.

References

1. Andriacchi et al. 2004 Ann Biomed Eng. 2. Beveridge et al. 2013, CMBBE. 3. Sharma et al. 2015 J Biomech.

Figures

Table 1. Surface model parameters resulting in proximity differences ≤ 0.05mm (minimal detectible difference of DF system).

	Tibia		Femur	
	MTP	LTP	MFC	LFC
Relative increase in mean triangle size (%)				
Irregular	20.1	17.6	21.0	31.1
Isometric	21.2	30.0	26.5	87.1
Tringle Size (mm)				
Irregular	0.49	0.49	0.48	0.52
Isometric	0.46	0.50	0.46	0.68

MTP/LTP: Medial/Lateral Tibial Plateau. MFC/LFC: Medial/Lateral Femoral Condyle.

VERIFICATION OF MESH SIZE AND MATERIAL PROPERTY ASSIGNMENT FOR FINITE ELEMENT MODELS OF THE HUMAN SECOND METATARSAL BONE

Anita Fung[1], Colin Firminger[1], Ian Matthews[2], and W. Brent Edwards[2]
[1]Biomedical Engineering Graduate Program, University of Calgary, [2]Faculty of Kinesiology, University of Calgary

Introduction

Metatarsal stress fractures are common injuries in athletic and military populations [1], and are believed to be associated with excessive bone strain [2]. As *in vivo* techniques for directly measuring bone strain are difficult and invasive [1, 3], finite element models have become important tools for strain estimation. The purpose of this study was to determine the proper element size and material property assignment for finite element models of the human second metatarsal bone.

Methods

CT images were acquired for the foot of a young adult male using a Discovery 610 CT scanner (General Electric Healthcare; Wauwatosa, USA) with acquisition parameters of 220 mA, 120 kVp, pitch=1, in-plane resolution 0.39 mm, and between-plane resolution 0.625 mm. A calibration phantom was used to convert CT Hounsfield units to bone apparent density. Metatarsals were first segmented, then meshed with quadratic tetrahedral elements using the Mimics Innovation Suite (Materialise, Leuven, Belgium). Seven different mesh densities were examined with maximum element edge lengths ranging from 2 to 8 mm. Elements were assigned inhomogeneous linear-elastic material properties based on bone apparent density. Two density-elasticity relationships were examined; one spanned the entire density range, the other was a piecewise relationship with different equations for trabecular and cortical bone [4]. Translational constraints were applied to the proximal end of each metatarsal. Loads calculated from plantar pressure data and a geometric forefoot model were applied to the inferior side of the metatarsal head. All models were solved using ABAQUS Standard v6.1 (ABAQUS Inc., Providence, USA).

The optimal mesh density was selected according to a convergence criteria of 5% of the resulting maximum and minimum principal stresses and strains. To test the effects of the material property assignment, strains on the dorsal surface of the 2nd metatarsal were compared to previously reported *in vivo* measurements [1, 3].

Results

The model with a maximum element edge length of 3 mm fulfilled the mesh density convergence criteria. At this mesh density, the model was solved in under 20 seconds. The equation that spanned the full density range (Figure 1) resulted in strains that were within one standard deviation of the literature values [1, 3]. The piecewise relationship had overestimated cortical moduli, thus resulting in strains that were within 1.5 standard deviations of literature values [1, 3].

Conclusions

This project determined the optimal mesh density and material property assignment for a finite element metatarsal model. These parameters will serve as a basis for future *in vitro* work for a rigorous validation study. The ultimate goal is to use this modeling approach to examine bone strain under a variety of running conditions in an attempt to reduce the likelihood of stress fracture.

References

[1] Arndt (2002). J. Biomech. 35:621-28.
[2] Pattin (1996). J Biomech. 29:69-79.
[3] Milgrom (2002). Foot Ankle Int. 23:230-35.
[4] Rho (1995). Med. Eng. Phys. 17:347-55.

Figures

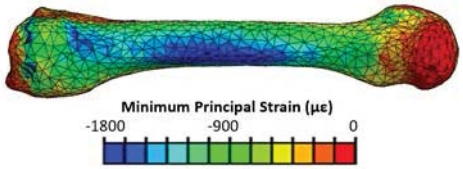

Figure 1: Minimum principal strain distribution on the dorsal surface of the second metatarsal. Material properties were calculated using the equation $E=6.57\rho_{app}^{1.37}$, where E is the elastic modulus in GPa, and ρ_{app} is the apparent density in g/cm^3 [4].

Expansion of Equine Cord Blood Derived Mesenchymal Stem Cells on Microcarriers

Erin Roberts[1], Tylor Walsh[1], Thomas Koch[2], Michael Kallos[1]
[1]Pharmaceutical Production Research Facility (PPRF), Schulich School of Engineering, University of Calgary
[2]Ontario Veterinary College, University of Guelph

Introduction

With nearly a million domestic horses in Canada, the horse industry contributes $19 billion annually to the Canadian economy [1]. However, $259 million is spent annually in Canada on veterinary services [1], with injuries to tendon, ligaments and joint cartilage as the leading cause of loss of performance in horses [2]. Mesenchymal Stem Cells (MSCs) have shown promise for the treatment of joint injuries in horses, however, static expansion of these cells for clinical use has limited potential due to the large numbers of cells that are required for treatment [3]. Expansion of cells in bioreactors using microcarriers as a scaffold has the potential to generate a large number of cells, using a significantly smaller space, under highly controlled conditions, with reducing time, labour, and monetary requirements.

The objective of this study was to test equine cord blood mesenchymal stem cells (eCB-MSCs) attachment and expansion ability on different microcarriers within bioreactors.

Methods

Two different microcarriers were inoculated with eCB-MSCs at a density of 3000 cells/cm^2 in 125mL bioreactors. The medium consisted of DMEM, 30% FBS, 1% L-glutamine, and 1% antibiotic/antimycotic. The bioreactors were run at 40rpm at 37ºC and 5% CO_2. Attached cells were counted daily using nuclei release assay method.

Results

The attachment efficiency of the cells was about 55% on both microcarriers. As seen in Figure 1, the attached cell density on both Microcarriers 1 and 2 was very similar for Days 1 through 7, achieving around 15,000 cells/cm^2 on Day 7, a 9 fold increase from the initial attached cell density. After Day 7, the cells on Microcarrier 1 began to detach and die, and the attached cell density decreased. However, the cells on Microcarrier 2 continued to grow until Day 9, when a maximum attached cell density of 23,000 cells/cm^2 was achieved, a 17 fold increase from the initial attached cell density.

Conclusions

Both microcarriers were suitable platforms for cell attachment and growth within bioreactors, however Microcarrier 1 had a lower maximum attached cell density than Microcarrier 2. Further investigation is required to determine ideal bioreactor operating conditions such as agitation rate and medium replacement regime.

References

[1] Equine Canada. (2010). 2010 Canadian Horse Industry Profile Study. Retrieved from http://equinecanada.ca/industry/index.php?option=coc_content&view=section&id=103&Itemid=559&lanl=en

[2] Koch, T. G., Heerkens, T., Thomsen, P. D., & Betts, D. H. (2007). "Isolation of mesenchymal stem cells from equine umbilical cord blood." *BMC Biotechnology*, *7*, *26.*

[3] Fortier, L. a, & Travis, A. J. (2011). "Stem cells in veterinary medicine". *Stem Cell Research & Therapy*, *2*(1), 9.

Figures

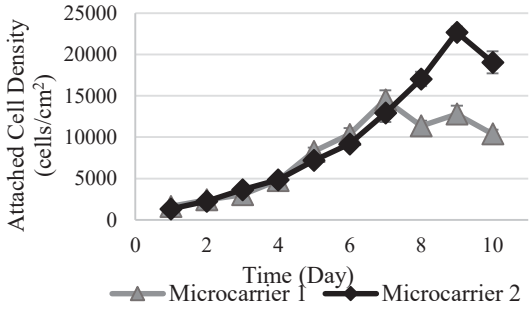

Figure 1: Attachment of eCB-MSC's on two different microcarriers in 125mL bioreactors. Error bars represent standard error of the mean of duplicate reactors counted twice.

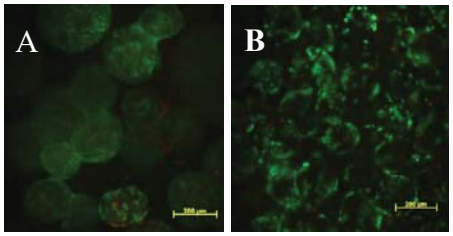

Figure 2: eCB-MSC's attached to Microcarrier 1 (A) and Microcarrier 2 (B) at Day 10, stained with Calcein-AM/Ethidium Homodimer 1

Monitoring LFCN Compression during Adolescent Idiopathic Scoliosis (AIS) Surgery: Is time or pressure the critical factor?

Negar Behzadi Fard, Kajsa Duke
University of Alberta

Introduction

For 20% of patients having scoliosis surgery, problems as tingling, numbness and redness on the hip after the surgery is reported (1). It is assumed that the intraoperative pressure can affect the LFCN injury during AIS surgery. In this study, the intraoperative pressure during the AIS surgery is measured using Force Sensing Array (FSA) pressure mapping system (Vista medical, Winnipeg).

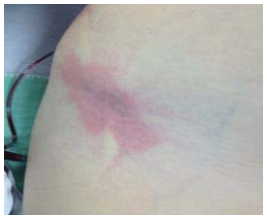

Figure 1: Redness after surgery

Material and Methods: Based on the surgeon's decision to have either a chest bar or two cushions on the frame, a set of three or four pressure mats (FSA, Vista Medical, Winnipeg) were placed on the Jackson frame before positioning the patient. Two types of FSA pressure mats were used: soft ones under the chest with max pressure of 310 mmHg and hard ones under the hips with maximum pressure of 517 mmHg. Data was collected continuously during the operation. The duration of surgery varied between 2 to 7 hours. A patient follow up sheet was prepared to ask patients if they have any numbness or tingling in their thighs with a light touch sensation testing performed. Moreover, the appearances of the redness of the front iliac crests are documented to be compared to the thigh condition.

Results: Data has been collected for 23 patients to date. This is done continuously except the times for electro-cautery as a result of noise. Maximum and average pressure for each case was calculated. Other factors like traction, body mass index and duration of the surgery were also compared to see if the pressure is the most significant factor or not. Overall 11 patients (48%) had problems such as redness and blister on their hip after the surgery. 2 patients (9%) had redness on their left hip, 3 (13%) had redness on right hip after surgery and during their stay on hospital and 6 (26%) patients had redness on both sides. Results show that the patients with redness or blister on their hip did not have much higher pressure than others. Moreover, the traction is not a significant factor in LFCN injury. Based on results, the duration of surgery is an important factor since patients with surgeries longer than 5 hours had redness and LFCN problems. Figure 2 shows the filtered data over time

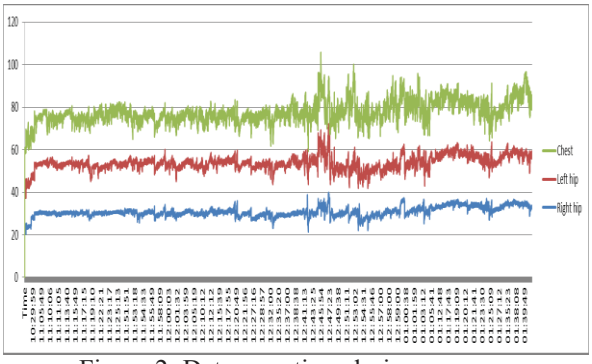

Figure 2: Data over time during surgery

Conclusion

It is understood from results to date that intraoperative pressure is not the only factor causing LFCN compression. Investigating all factors which could have an effect on LFCN compression injury show that duration of surgery and BMI may also affect LFCN injury during AIS surgery.

References:

1) Mirovsky Y, Neuwirth M. Injuries to the lateral femoral cutaneous nerve during spine surgery. Spine, 2000 May 15; 25(10):1266-9

Towards an Accurate Impact Assessment Sensor for Helmeted Impacts

Brooklynn Knowles[1] and Christopher R. Dennison[1]
[1]Biomedical Instrumentation Lab, Department of Mechanical Engineering, University of Alberta

Introduction

The GForce Tracker (GFT) records head kinematics during contact sports. The GFT is designed to alert the helmet wearer when kinematic thresholds on injury risk are exceeded. Assuming kinematic thresholds are sound, the ability of the GFT to estimate injury risk relies solely on its ability to measure the kinematics of the helmeted head. GFT measures linear acceleration and angular velocity during impact. Imperfect coupling between the human head and helmet can cause differences in measures between the kinematics of the helmet (GFT) and the head. Quantifying these differences is an important step required to understand the accuracy of GFT measures. The objective of this work is to quantify the GFT ability to measure peak linear acceleration (peak g) and maximum change in angular velocity (ω), and, as expanded upon below, ability of GFT measures to predict concussion risk.

Figure 1: GFT location a) inside the back of the helmet and b) outside at the apex

Methods

We simulated head impacts with a standard hockey helmet (Bauer 4500) using the UofA helmet test bed to achieve peak accelerations ranging from 10g-100g (N=900). Linear acceleration and angular velocity from the GFT and Hybrid III were measured and input to the Simulated Injury Monitor (SIMon) brain FE model and the Cumulative Strain Damage Measure (CSDM) was computed (n=17). CSDM is arguably the best metric for concussive injury prediction [1]. Linear regression was used to evaluate agreement between peak kinematic measures (peak g and ω) of GFT and Hybrid III as well as GFT ability to predict CSDM.

Results

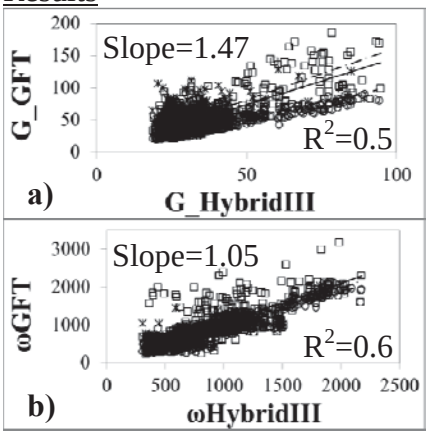

Figure 2: GFT vs Hybrid III for a) peak g and b) change in ω (degs/s)

Discussion and Conclusions

Peak g measured by the GFT was on average 47% greater than Hybrid III peak g (Figure 2a)). Studies have shown, however, that helmet acceleration can greatly exceed head acceleration in impact [2]. Over-estimations can be corrected using calibration factors. Angular velocity, on the other hand, showed low systematic error, agreeing with Hybrid III measures to within 5% on average (Figure 2b)). Impact data, where agreement between angular kinematics of the GFT and Hybrid III was within 10%, was used to compute and compare CSDM. On average, GFT kinematics gave CSDM values 54% greater than Hybrid III kinematics; however, there was good correlation (R^2=0.7) between CSDM predictions of each system (Figure 3). This suggests that GFT can accurately measure kinematics related to concussive injury, and identify concussive injury risk.

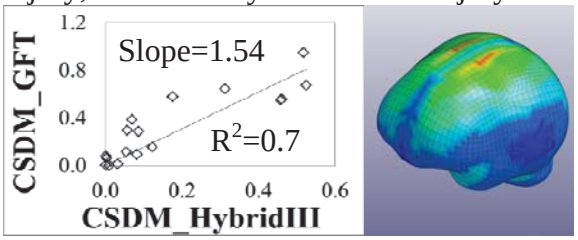

Figure 3: (left) scatter plot of GFT vs Hybrid III CSDM values; (right) brain FE model

References

[1] Takhounts et al., STAPP V.57 (2013); [2] Manoogian et. al., Biomed. Sci. Instrum (2006)

Migration and proliferation of human skin-derived precursor (hSKP) cells in enzymatically crosslinked hybrid hydrogels

Fraz Anjum[1], Philipp Lienemann[2], Martin Ehrbar[2], Jeff Biernaskie[3], Michael S Kallos[1]
[1] Pharmaceutical Production Research Facility, University of Calgary, 2500 University Dr. Calgary AB T2N 1N4 Canada
[2] University Hospital Zürich, Rämistrasse 100, 8006 Zürich, Switzerland
[3] Department of Comparative Biology and Experimental Medicine, Faculty of Veterinary Medicine, University of Calgary 3330 Hospital Dr. Calgary, AB, T2N 4N1 Canada

Introduction

Chondroitin sulfate (CS), a glycosaminoglycan component of the extracellular matrix (ECM) has been shown to be centrally involved in the regulation of differentiation and maintenance of various stem cells [1, 2]. Based on its active role during tissue formation and homeostasis [3], CS is a promising starting material for the engineering of biomaterials with tunable physico-chemical and biological properties such as matrix stiffness or growth factor binding. Herein we describe the formation of a novel enzymatically cross-linked hybrid hydrogel consisting of CS and poly(ethylene glycol) (PEG) for establishment of skin constructs for dermal regeneration based on hSKPs.

Methods

CS was functionalized with a matrix metalloproteinase (MPP) degradable lysine donor substrate, Lys-MMP-peptide and 8-arm PEG-VS (PEG-vinyl sulfone) was functionalized with FXIII recognizable peptide (NQEQVSPL). Hydrogels are formed by mixing two gel precursors in the presence of FXIII under physiologic buffer conditions. Swelling behavior, storage moduli and fluorescence recovery after photobleaching (FRAP) of hydrogels were done to characterize the network architecture. hSKPs (single cells vs. spheres) were encapsulated in PEG-CS hydrogels at a density of 30,000 cell/gel. Migration of hSKPs and spheres within 3D hydrogels was studied via time-lapse confocal microscopy.

Results

The results showed that network properties of hydrogels depend on the degree of substitution of CS-Lys, concentration of gel precursors and the stoichiometric ratio between the two components of the hydrogel system. Matrix stiffness, crosslink density and degree of swelling also influence cell viability, proliferation, differentiation and migration. We showed that hSKPs remain viable and can proliferate upon encapsulation into CS-PEG hybrid hydrogels (Fig. 1). Time-lapse microscopy showed that human dermal progenitors also exhibit robust emigration from encapsulated colonies within 3D hydrogels.

Conclusions

The modular design of the PEG/CS hydrogels allows for the incorporation of Gln-tagged bio-functional molecules, including RGD peptides or growth factor affinity domains on demand. hSKPs undergo MMP-mediated migration and proliferation within hydrogels and suggesting they may serve as a potential tool for cell delivery.

References

1. Hayes AJ, J Histochem Cytochem 2008
2. Volpi N, Chem Biol Interact 1997
3. Strehin I, Biomaterials 2010

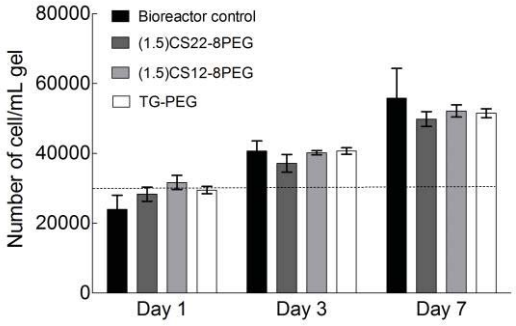

Figure 1: SKPs cell proliferation in hybrid hydrogels. The dotted line represents the initial cell density at day 0.

Dissociated Sensory Neuron Culture of Adult Rats: A Protocol Comparison

M. Purdy[1], J. Kawasoe[2], W. Zaidi[2,3], R. Midha[2,4], N. I. Syed[2,3], C. Dalton[1,5]
[1]Biomedical Engineering Program, [2]Hotchkiss Brain Institute [3]Department of Anatomy and Cell Biology,
[4]Department of Clinical Neurosciences [5]Department of Electrical and Computer Engineering
University of Calgary, Alberta, Canada

Introduction

Dissociated rodent sensory neurons are one of the most commonly used neuronal cell models for primary cell culture. Their relative ease of isolation and ability to maintain healthy growth cones *in vitro* allows for investigations of differentiation, electrophysiology, and nerve regeneration.

Sensory neurons are found in dorsal root ganglia (DRGs) within the spine, and are commonly used in *in vitro* nerve regeneration experiments. Unfortunately, protocols for cell isolation and culture vary widely between research groups, and no one method has been accepted as the standard for such experiments. Presented here is a comparison of primary culture protocols as reported in the literature, with a recommendation for future single-cell regeneration experiments.

Methods

Two cell culture protocols that represent common rodent cell techniques [1, 2], and two defined media were compared in their abilities to support rat sensory neurons. In both cases DRG isolation and substrate preparation was performed in the same manner, detailed in [3]. Briefly, the sciatic nerve of a male Lewis rat was transected 3 days prior to cell isolation. The L4, L5, and L6 DRGs, whose axons extend to the pre-injured sciatic nerve, were harvested.

The first protocol examined used a 0.1% collagenase enzyme to dissociate full DRGs for 1 hour, followed by pipette trituration. Debris removal through centrifugation was followed by suspension in media: DMEM/F12 (*Life Tech.*) enriched with nerve growth factor (NGF) and N2 nutrients (*Life. Tech.*). The second protocol placed DRGs into collagenase-papain (0.4% collagenase, 4% papain) for 20 minutes, and DNase for another 10 minutes, agitating periodically. Pipette trituration was followed by debris removal, and suspension in the aforementioned media, or a neurobasal medium enriched with B27 nutrients (*Invitrogen*) and NGF. Cells were plated individually onto substrates by pipette placement, and were allowed to grow for 24 hours before imaging and health assessment of soma and neurite outgrowth.

Results

The percentage of healthy cells following each cell culture is detailed in Figure 1. It is apparent that the culture media is more impactful on cell viability than the culturing technique in this circumstance.

Conclusions

The comparison provided here shows that for axotomized lumbar DRGs, the best cell culture involves the use of collagenase-papain and DNase dissociation media, and a time-reduced enzyme digestion step, in conjunction with an enriched neurobasal culture media. We recommend that this combination become a standard protocol for future rat and mouse nerve regeneration studies when plating individual cells.

References

1. Li R (1998) *Method Cell Biol*; **2.** Malin S + (2007) *Nat. Protoc.*; **3.** Purdy M +, (2015) *BMES Proc.*

Figures

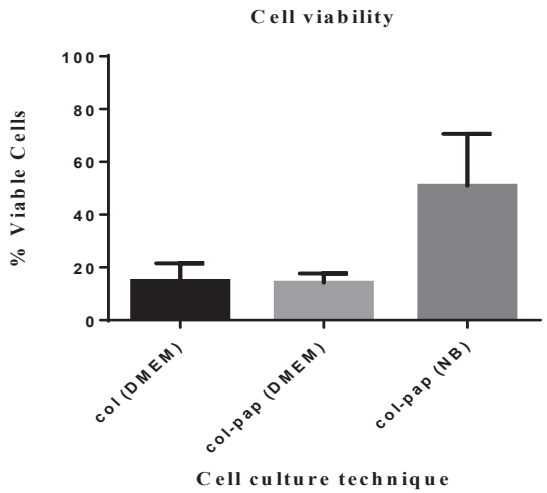

Figure 1 – Percent of viable cells 24 hours after culturing, using collagenase (col), or collagenase-papain (col-pap). The media is in brackets (DMEM/F12 or neurobasal).

Chitosan/Decellularized Cartilage Microcarriers for Chondrogenic Stimulation of Synovial Fluid Derived Mesenchymal Stem Cells

Jolene A. Phelps, Sumrita Bhat, Arindom Sen
Pharmaceutical Production Research Facility, Department of Chemical and Petroleum Engineering
University of Calgary, Calgary, Alberta T2N 1N4

Introduction

The ability of mesenchymal stem cells (MSCs) to create and maintain tissues in the body has generated vast research interest in using them to develop new treatment alternatives for disease and injury. Suspension bioreactors provide a method to scale-up the production of MSCs as they are able to maintain a highly controlled environment. However, MSCs are adherent, and thus, require a surface on which to grow. Small spherical beads called 'microcarriers' are added to the cell culture to provide a surface for cells to attach and proliferate.

The surface characteristics and composition of the microcarriers can determine the extent of cell attachment and growth as well as influence the fate of the cells through both physical and biochemical cues[1]. Providing the cells with an environment similar to that of its native environment has been shown to induce unspecialized stem cells to differentiate into a specific lineage[2]. The extracellular matrix (ECM) of cartilage provides both structural strength to the tissue and serves as a reservoir for growth factors and cytokines. Thus by the incorporation of decellularized cartilage (DC) into microcarriers, it is possible to stimulate MSCs to differentiate towards a chondrogenic lineage.

Methods

Cartilage was attained from bovine knee joints and decellularized through a combination of chemical and freeze thaw processes, as described by Tavassoli[3]. The decellularized cartilage was then digested with pepsin and added at 50/50 volume to chitosan dissolved in acetic acid. An emulsion method modified from Denkba[4] was used to create the microcarriers. The chitosan/DC mixture was added to an emulsion of paraffin oil and petroleum ether (60/40 volume ratio) using Tween 80 as an emulsifier. Glutaraldehyde was added at several time points to crosslink and stabilize the microcarriers. The process was optimized to create consistent spherical particles with a small size distribution by varying the speed and concentrations of both chitosan and glutaraldehyde.

The surface of the microcarriers was characterized using scanning electron microscopy. An experiment was run to determine the effect of DC content on MSC growth. The microcarriers were seeded with synovial fluid derived MSCs (SF-MSCs) cultured in PPRF-MSC6 medium in 24 well plates at 37°C and 5% CO_2 and tested against a control of pure chitosan beads. Samples were taken on day 1, 3, 6 and 8 to study attachment, proliferation and morphology of the cells.

Results

The presence of DC in microcarriers promoted cell growth and influenced the morphology, or differentiation of synovial fluid derived MSCs over 8 days.

Conclusions

Microcarriers incorporating chitosan and decellularized cartilage provide an effective means to support the growth and initial chondrogenesis of SF-MSCs. The biocompatibility and biodegradability of the microcarriers would enable them to be directly used in cartilage repair applications.

References

1. Hatakeyama H, Kikuchi A, Yamato M, Okano T. Bio-functionalized thermoresponsive interfaces facilitating cell adhesion and proliferation. *Biomaterials*. 2006;27(29):5069-5078.
2. Yang Z, Shi Y, Wei X, et al. Fabrication and repair of cartilage defects with a novel acellular cartilage matrix scaffold. *Tissue Eng Part C Methods*. 2010;16(5):865-876.
3. Tavassoli A, Mahdavi-shahri N, Matin MM. Bovine articular cartilage decellularized matrix as a scaffold for use in cartilage tissue engineering. 2012;4(1):1-8.
4. Denkba EB et al. 5-Fluorouracil loaded chitosan microspheres for chemoembolization. *J. Microencapsulation*. 1999;16(6);741-749.

Estimating Dielectric Properties of Biological Tissues at Microwave Frequencies

David C. Garrett, Bryce A. Besler, Jeremie Bourqui, and Elise C. Fear
dgarrett@ucalgary.ca

Introduction

Microwave imaging has been of interest in recent decades, offering the potential of an affordable and non-ionizing medical diagnostic modality. One approach is microwave radar imaging, which creates images by focusing signals caused by reflections at material interfaces. To improve the images from radar approaches, patient-specific dielectric property (DP; permittivity and conductivity) estimations have been used to determine the speed of wave travel within the tissue [1]. Methods such as local rod probes exist to estimate DPs, but are of limited use for *in vivo* measurements due to their shallow sensing depth. We have previously developed methods of permittivity estimation with a custom antenna, however this approach requires two measurements at different separation distances and is unable to estimate conductivity. This study aims to improve on methods of estimating permittivity and to add an estimate of conductivity of *in vivo* biological tissue by incorporating an antenna calibration method.

Methods

In order to remove the influence of the antennas on measurements, a previously developed calibration method [2] was adapted to be used with a custom antenna system [3], allowing DPs to be estimated over a range of frequencies. The antennas are characterized as 2x2 matrices at each frequency, determined from two calibration measurements: one with the antennas separated by an electrical conductor, and one with the antennas in direct contact with one another. Samples were placed between the two antennas, with their surfaces in contact with the antenna apertures. Measurements were quickly performed using a commercial vector network analyzer. DPs were then estimated from the calibrated transmission signal. To validate this method, DPs of several liquids were estimated and compared with literature.

Results

A general agreement was seen between the estimated and literature DPs of several liquids. For example, the estimated permittivity of distilled water is shown in Figure 1. Literature values were obtained using local rod probes which are reliable for homogenous liquids. Biological tissues such as the human calf and heel were then assessed. Literature for these tissues is limited, since noninvasive *in vivo* measurements using local rod probes are generally restricted to surfaces such as the skin and tongue.

Conclusions

A calibration method has been adapted to enable an antenna system to estimate the DPs of *in vivo* tissues at microwave frequencies. The estimated properties of the tested liquids align closely to literature, providing confidence in the estimates of biological tissues with limited literature.

References

[1] Bourqui, J et al. *IJBI*. 2012

[2] Bartley, PG and Begley, SB. *IMTC*. 372-375, 2005.

[3] Bourqui, J and Fear, EC. *IEEE AWPL*. **11:**1614-1617, 2015.

Figures

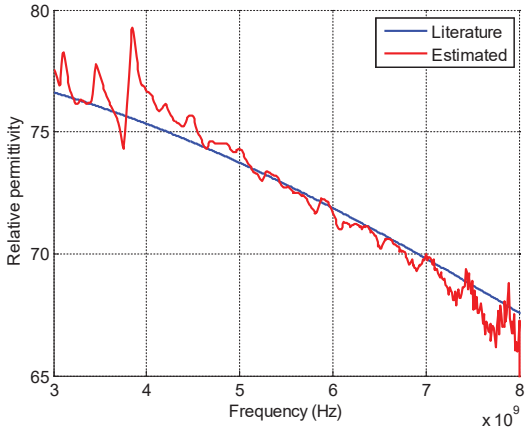

Figure 1: Estimated and literature values of relative permittivity as a function of frequency for distilled water.

Serum Cytokine Profiles are Distinct between Patients with Hip or Knee Osteoarthritis and Associated with Hip Pain

Guomin Ren, Ian lutz, Pam Railton, J. Preston Wiley, Jenelle McAllister, James Powell, Roman J. Krawetz
HRIC 3C41, 3330 Hospital Drive NW, Calgary, Alberta, Canada T2N 4N1

Introduction

Osteoarthritis (OA) is a prevalent musculoskeletal disease that can affect any synovial joint in the body[1]. OA of knee and hip are very common and are the major cause of chronic disability in older populations[2]. Although a number of biochemical markers have shown promising potentials for early OA diagnostic[3], current diagnostics are only able to identify patients with advanced OA, when extensive and irreversible deterioration of joint has already occurred. While, many studies have been undertaken in regard to biomarkers for both knee and hip OA, only a few have comparisons between knees and hips. In addition, cytokines play an important role in the pain signal pathway[4], but very few human studies have reported correlations between cytokines and OA pain.

Methods

250 patients (100 knee OA, 50 hip OA, 100 control) were recruited. Inflammatory profiles in serum samples were analyzed using the Multiplex Human Cytokine Panel (Millipore) on the Luminex 100 platform (Luminex Corp., Austin, TX). The pain, physical function and activity limitations of hip OA cohort were scored using the WOMAC, SF-36, HHS and UCLA scores.

All cytokine levels were compared between cohorts individually using Mann–Whitney–Wilcoxon (MWW) test with Bonferroni multiple comparison correction. Within hip OA cohorts, the effect of hip alignment (impingement and dysplasia) and radiographic grade (Kellgren and Lawrence grade, K/L grade) on cytokine levels were accessed by MWW test. Spearman's rank correlation test used to assess the association between cytokines and pain levels.

Results

The three cohorts showed distinct inflammatory profiles. Specifically, EGF, FGF-2, MCP-3, MIP-1a, IL-8 were significant different between knee and hip OA; FGF-2, GRO, IL-8, MCP-1, VEGF were significant different between hip OA and control; Eotaxin, GRO, MCP-1, MIP-1b, VEGF were significant different between knee OA and control (p-value < 0.0012). For hip OA cohorts, cytokines do not differ between K/L grade 3 and K/L grade 4 or between impingement and dysplasia. Three cytokines were significant associated with pain: IL-6 (p-value = 0.045), MDC (p-value = 0.032) and IP-10 (p-value = 0.038).

Conclusions

We have demonstrated that differences in serum inflammatory profiles exist between hip and knee OA patients. These differences suggest that OA may include different inflammatory subtypes according to affected joints. We also identified that the cytokine IL-6, MDC and IP-10 are associated with pain level in hip OA patients. These cytokines might help explain the inconsistent of pain presentations and radiographical severity of OA joints. Future studies are needed to validate our findings and then to understand the following questions: (1) how different affected joints reflected in systematic biomarkers; (2) how cytokines are involved in OA pain.

References

1. Lawrence, R.C. et al. Estimates of the prevalence of arthritis and other rheumatic conditions in the United States. Part II. *Arthritis Rheum* **58**, 26-35 (2008).
2. Sandell, L.J. Etiology of osteoarthritis: genetics and synovial joint development. *Nat Rev Rheumatol* **8**, 77-89 (2012).
3. Hunter, D.J., Nevitt, M., Losina, E. & Kraus, V. Biomarkers for osteoarthritis: current position and steps towards further validation. *Best Practice & Research Clinical Rheumatology* **28**, 61-71 (2014).
4. Miller, R.E., Miller, R.J. & Malfait, A.M. Osteoarthritis joint pain: the cytokine connection. *Cytokine* **70**, 185-93 (2014).

Functional Measures of Muscle Loading and Strength and its Relation to Bone Volume.

Aleen Pangka[1], Shannon Giorgini[2], David A. Hanley[3], Steve K. Boyd[2,3,4] and W. Brent Edwards[2,3]
[1]Biomedical Engineering Graduate Program, [2]Faculty of Kinesiology, [3]Cumming School of Medicine, and [4] Schulich School of Engineering, University of Calgary

Introduction

The human skeleton is required to withstand high magnitudes of repetitive loading. This loading also influences bone composition to ensure the structural competence of bone [1]. Muscles attach to bone and the largest loads applied to bone during habitual activity come from voluntary muscle contractions [2]. In this study, we examined maximal muscle contractions (i.e., muscle strength) and habitual muscle contractions (i.e., joint moments), and quantified their relationship with bone volume.

Methods

Ten healthy post-menopausal women (age 65.4 ± 6.23 yrs, height 162.26 ± 6.9 cm, weight 67.03 ± 8.22 kg) were recruited to participate in this study. Isokinetic and isometric muscle strength for each participant's right ankle plantarflexor and dorsiflexor muscles were measured using a Biodex Dynamometer (System Pro 3, Biodex Medical Systems Inc., USA). Isokinetic testing was performed at both 60°/s and 120°/s. Isometric testing consisted of maximum contractions held for six seconds. Plantarflexor strength was tested with the ankle at 0° and dorsiflexor strength was tested with the ankle at 25° plantarflexion.

Retroreflective markers were placed on anatomical landmarks of the right lower extremity. Participants were asked to walk over ground at a self-selected (1.46 ± 0.21 m/s) and prescribed (1.40 ± 0.07 m/s) pace. Motion analysis (Motion Analysis Corporation, USA) and force platform (Advanced Mechanical Technology Inc., USA) data were collected at a sampling frequency of 240 Hz and 1200 Hz, respectively. Three dimensional inverse dynamics using Newton Euler equations of motion were used to calculate ankle joint moments.

A high resolution peripheral quantitative computed tomography scan (XtremeCT2, Scanco Medical, Switzerland) of the participant's right distal tibia was obtained (nominal isotropic resolution = 61 μm). Bone volume was segmented from the surrounding soft tissue using Mimics software (Materialise, Belgium). Pearson product-moment correlations were used to assess the relationships between muscle strength, joint moments and bone volume.

Results

Peak plantarflexion moment at preferred walking speed was the only parameter that significantly correlated with bone volume ($r=0.700$, $p < 0.05$; Table 1); prescribed walking speed approached significance ($r= 0.583$, $p = 0.077$).

Conclusions

These results suggest that individuals with stronger muscles may not necessarily have larger bones. Rather, the results suggest that larger habitual muscle contractions are associated with larger bone volume. Future work will examine the relationship between measures of muscle loading and muscle strength with other measures of bone quality (e.g., bone stiffness and strength).

References

[1] L. E. Lanyon, *J. Biomech.*, vol. 20, 1987;
[2]H. M. Frost. *J. Bone Miner. Res.*, vol. 12, 1997.

Table 1. Pearson correlation coefficients and p-values between bone volume and isokinetic and isometric muscle strength as well as peak plantarflexion moment at preferred and prescribed speed.

	Plantarflexion			Dorsiflexion			Peak Plantarflexion Moment	
	60°/s	120°/s	Isometric	60°/s	120°/s	Isometric	Preferred	Prescribed
r	0.368	- 0.256	0.539	- 0.19	0.276	0.179	0.700	0.583
p-value	0.259	0.475	0.108	0.959	0.440	0.621	0.024	0.077

Pipeline for an Atlas-based Analysis of Mouse Brain MRI's Obtained with a Helium Cooled RF Coil

Hamilton A.M.[1,2,3], Forkert N.[1,2,3], Dunn J.F. [1,2,3,]
Department of Radiology[1], Hotchkiss Brain Institute[2], Cumming School of Medicine[3], University of Calgary

Introduction

Magnetic resonance imaging (MRI) has become a powerful tool for studying brain morphology in mouse models of human disease. In order to compare MRI images between subjects in a quantitative fashion, it is ideal if an operator independent method to obtain regional volumes can be applied. This abstract describes a recently developed processing pipeline optimized for studies of mouse brain volumetrics.

Brain images must be normalized to correct for variations in brain anatomy. This includes differences in brain size and shape as well as the location and size of anatomical structures [1]. Using a minimum deformation atlas, we can create an average brain image from a group of subjects by averaging multiple MRI images [2,3]. Individual images can be compared to this average image to study changes to the brain as a result of disease or altered phenotypic expression.

When analyzing images in this way, it is important that RF sensitivity be uniform. The high sensitivity cryoprobe used in these studies is a surface coil, which has significant RF inhomogeneity. There is predictable signal decline as you move away from the coil. [4]. We will correct for intensity variation and normalize brain images against a mouse atlas, allowing us to compare and measure differences between anatomical structures.

Methods

Imaging was conducted using a 9.4T MRI with a helium cooled Bruker cryoprobe. Female C57BL/6 mice were imaged using a FLASH sequence (TR=2000ms, TE=6.5ms, Flip angle=60^o). Image intensity was normalized using the N3 algorithm [4], to correct for signal drop-off associated with surface coils. A previously generated atlas was used for image registration [2]. Using the program Niftyreg, individual images underwent non-linear co-registration against the atlas. The atlas was overlaid over the individual images segmenting and labeling anatomical structures.

Results

An example high-resolution image, pre-processed, is shown in Fig 1. The N3 algorithm, based on visual assessment, successfully corrected for any intensity bias. The images were segmented into 62 structures.

Conclusions

By constructing this pipeline we were able to take individual MRI images, correct for intensity biases, and normalize them to match an average representation of a mouse brain. This allows for anatomical segmentation and labeling in the individual brains, as well as comparisons between specimens. We will use this pipeline to study the volumetric changes in long-term EAE mice.

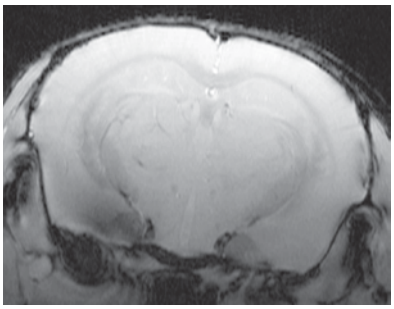

Fig. 1. MRI of a C57BL/6 mouse brain. Resolution = 39x78x500μm.

References

[1] Mackenzie-Graham A., Tinsley MR., Shah KP., Aguilar C., Strickland LV., Boline J., Martin M., Morales L., Shattuck DW., Jacobs RE., Voskuhl RR., Toga AW. Neuroimage. 2006; 32(3): 1016-23.
[2] Dorr AE., Lerch JP., Spring S., Kabani N., Henkelman RM. Neuroimage. 2008; 42(1): 60-69.
[3] Kovačević N., Henderson JT., Chan E., Lifshitz N., Bishop J., Evans AC., Henkelman RM., Chen XJ. Cereb Cortex. 2005; 15(5): 639-45.
[4] Sled JG., Zijdenbos, AP., Evans, AC. IEEE T Med Imaging. 1998; 17(4): 87-97.

Determining In-Vivo Human Tibiofemoral Cartilage Stiffness Mechanics using High-Speed Dual-Fluoroscopy and Magnetic Resonance Imaging

Brodie Ritchie, Gregor Kuntze, Gulshan Sharma, Jillian Beveridge, Jessica Küpper, Janet Ronsky
Mechanical and Manufacturing Engineering, University of Calgary, Calgary, AB, Canada

Introduction

Anterior cruciate ligament deficiency (ACLD) dramatically increases the risk of knee osteoarthritis (OA). Currently there is no clinical diagnostic to predict the risk of joint degeneration in pre-radiographic OA. Early changes to tibiofemoral (TF) cartilages include tissue swelling and softening, which may increase the risk of mechanical damage. This research group investigates in-vivo cartilage stiffness, the resistance to deformation in response to an applied force, in pre-radiographic OA using high-speed dual fluoroscopy (DF) and magnetic resonance (MR) imaging. Current evidence supports the feasibility of measuring in-vivo cartilage deformation during standing weight bearing. The purpose of this MSc research is to develop methods to combine deformation and joint force estimates to determine changes in mediolateral cartilage stiffness in pre-radiographic OA.

Methods

Preliminary data were collected for ACLD (n=4, >5 year history) and healthy control (n=5, CON) subjects. Bilateral ankle, knee, hip MR data were obtained (GE 3T Discovery 750, USA). 3D bone and resting state cartilage models (triangular surface mesh) were created in Amira (FES, Germany). Standing weight bearing DF data (Fig. 1) were collected (6 Hz for 60 sec). TF bone kinematics were determined in Autoscoper (Brown University, USA) using undistorted and calibrated DF images. Resultant bone transformations were applied to co-registered tibial and femoral cartilage models respectively. Cartilage deformations were quantified as the change in median proximity of all model faces (surface normal distance to opposing surface) within 4mm of the apposing surface (Matlab 2015b, MathWorks, USA).

Results

Median proximity data for one CON and two ACLD subjects are shown in Fig 2. Cartilages deformed more in ACLD (10 year history) compared to the CON subject. Greater deformation indicates a reduced ability to resist compressive load.

Conclusions

These results provide a proof of concept that TF cartilage stiffness changes in pre-radiographic OA and that the in-vivo DF / MR measure is sensitive to detecting alterations in load deformation response. The aim of this MSc is to advance and validate current methods for mediolateral cartilage deformation estimates and material models of cartilage/meniscus compressive behavior. This will involve addition of novel inverse dynamics approaches to estimate resultant knee joint forces. Curve fitting approaches will be used to determine exponents of material behavior models for cartilage compression. This work supports the development of new clinical diagnostics of pre-radiographic OA.

References

[1] Lohmander et al. 2007 *Am. J. Sports Med.* 35(10): 1756–1769. [2] Calvo et al. 2004 *OA Cart.* 12(11): 878–86.

Figures

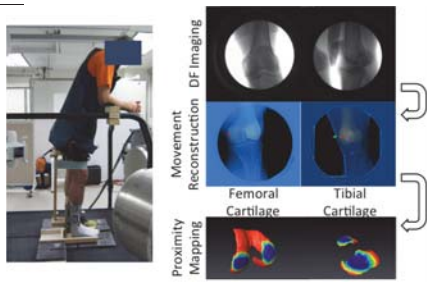

Fig 1. In-vivo compressive stiffness setup and data analysis workflow.

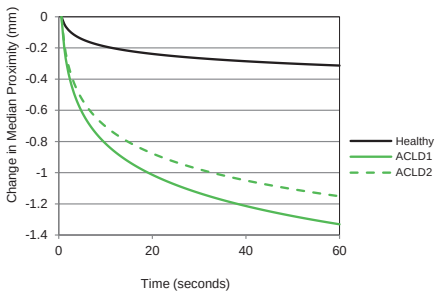

Fig 2. Δ median proximity for one healthy and two ACLD subjects.

THE INFLUENCE OF LOADING DURATION AND LOADING CYCLES ON COMPRESSIVE FATIGUE FAILURE OF BOVINE CORTICAL BONE

Lindsay Loundagin[1], Tannin A. Schmidt[1,2], W. Brent Edwards[1]
[1]Faculty of Kinesiology and [2]Schulich School of Engineering, University of Calgary

Introduction

Fatigue fractures associated with repetitive loading are often studied using *in vitro* mechanical testing of cadaveric bone. It is well documented that fatigue life is inversely proportional to applied stress [1]. Previous studies have also illustrated that tensile fatigue of bone is dependent on the duration of loading as opposed to the number of loading cycles [2,3]. However, the highest stresses in long bones are compressive [4] and it would be useful to characterize the importance of time versus cycles in compressive fatigue failure. The purpose of this study was to use the effects of loading frequency to determine if compressive fatigue in bone is a function of loading duration or loading cycles.

Methods

Twenty-two cylindrical cortical bone samples, 7 mm in diameter, were cored out from skeletally mature bovine femora (n=6) and tibiae (n=6). A gauge length of 7 mm was turned down with a lathe to a diameter of 5.25 mm. Brass ends caps were placed on the samples which were secured in custom grips in an 858 Mini Bionix test frame (MTS, Eden Prairie, MN). Uniaxial compression testing was performed under displacement control with a sinusoidal waveform. Samples were cyclically loaded at 3 and 0.5 Hz with displacements corresponding to stress ranges between 70-130 MPa. Fatigue failure was defined as complete catastrophic fracture as evidenced by the force-displacement curve or a stiffness degradation greater than 10%. Time to failure was calculated by dividing cycles to failure by loading frequency.

Results

Samples loaded at higher stresses failed within fewer cycles, with the slopes of the *S-N* curves for both frequencies being similar to previously reported values [1]. An effect of loading frequency was not observed as a function of loading cycles (Figure 1), but differences were observed as a function of loading duration (Figure 2). In other words, for a given stress range the number of cycles to failure was not affected by loading frequency suggesting cycle-dependent rather than time-dependent fatigue behavior.

Conclusions

Compressive fatigue failure of bone was dependent on the number of loading cycles regardless of loading frequency. This result experimentally confirmed the theory of cycle-dependent fatigue behavior previously proposed using mathematical modeling [2]. Our future work will continue to characterize the effects of loading frequency, strain magnitude and strain rate on the fatigue failure of bone.

References

[1] Lafferty (1979). J Biomech Eng. 101;112.
[2] Caler (1989). J Biomech. 22:(625-35).
[3] Zioupos (2001). J theor Biol. 210:389-99.
[4] Carter (1981). Acta Orthop Scand. 52:481-90.

Figures

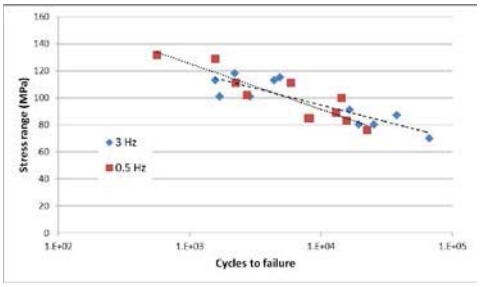

Figure 1: Stress range as a function of cycles to failure. There is no change in the cycles to failure associated with loading frequency.

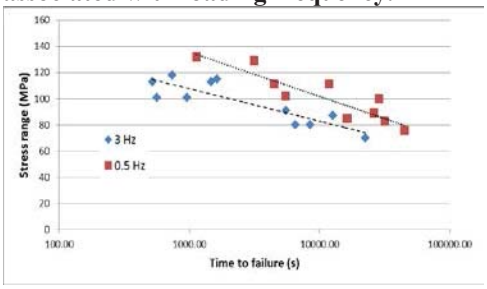

Figure 2: Stress range as a function of time to failure demonstrating the visual separation of the two frequency groups.

Dissociation of Synovial Membrane in Preparation for Single Cell Sorting

Nedaa Al-Jezani[1, 3], Asmaa Affan[2, 3], Pam Railton [3], Jim Powell[3], Roman Krawetz [1,2,3]

1 Medical sciences, Cumming school of Medicine, University of Calgary, 2 Biomedical engineering, University of Calgary, 3 McCaig Institute, University of Calgary

Introduction

Synovial Mesenchymal Stem Cells (SMSCs), which are found in the synovial membrane, are a promising cell source for articular cartilage repair in osteoarthritis (OA) patients [1]. In this study, we optimized the protocol for synovial membrane dissociation to prepare cells for single cell index sorting.

Methods

Synovial biopsies (2mm or 5mm) were obtained from patients undergoing total joint replacement. The biopsies were digested in either collagenase type I, IA, IV (Sigma) or II (Gibco) at a concentration of 0.5 or 1.0 mg/mL. Digestion was conducted at 37^{o}C for 30, 60, 90 or 120min. To assay for the number of MSCs obtained, the cell suspension was stained with CD90 (a synovial MSC marker) and magnetically purified (BD Bioscience). The purified cells were then assayed by flow cytometry (Co-stained with a live/dead cell marker, BV510, BD Biosciences) or bright-field microscopy.

Results

Biopsy size optimization: Synovial biopsies of 5mm produced a greater number of live CD90+ cells than 2mm biopsies (Figure 1).

Collagenase digestions optimization: It was observed that type II collagenase treatment for 120 min, type IV collagenase for 90, or 120min at either 0.5 or 1mg/ML resulted in a single cell suspension that contained viable CD90+ cells (Figure 2). Flow cytometry results (a summery of the results in Table 1) suggests that type II collagenase at lower concentration (0.5 mg/ml) for 2 hours and type IV collagenase at higher concentration (1 mg/ml) for 90 minutes released the greatest number of CD90 positive MSCs from the synovial membrane

Conclusions

We now have the optimized conditions to obtain viable CD90+ MSCs from the synovial membrane. In future studies, I will be charactering the MSCs from normal and osteoarthritic (OA) knee joints to determine what cell surface markers correlate with cells that have the greatest chondrogenic potential for use in novel cell therapies for OA.

References

[1]. Fan, J., Varshney, R.R., Ren, L., Cai, D., and Wang, D.-A. (2009). Synovium-derived mesenchymal stem cells: a new cell source for musculoskeletal regeneration. Tissue Eng. Part B. Rev. *15*, 75–86.

Figures

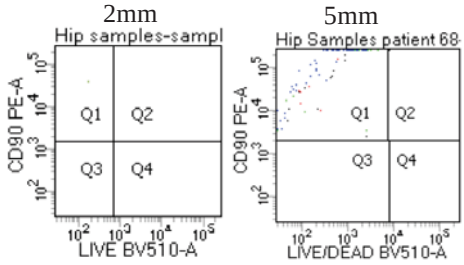

Fig1:Number of live CD90+ cells sorted from 2mm and 5 mm biopsy.

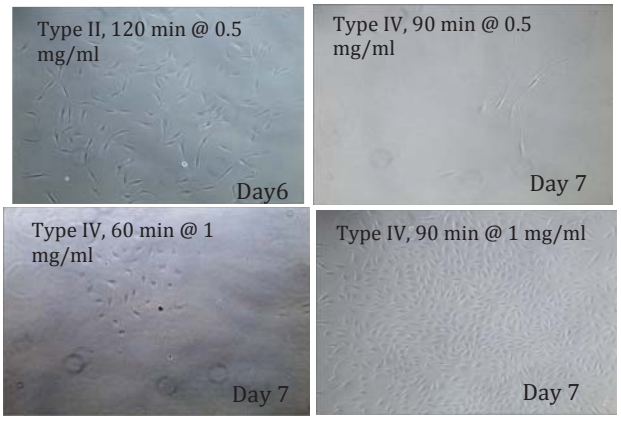

Fig 2: Shape and the size of the proliferated cells. Type IV collagenase digestion at 1 mg/ml for 90 minute

Condition	Number of CD90+ cells
Type I (90 min @ 1mg/mL)	222
Type II (90 min @ 1 mg/mL)	1015 (cells from two wells)
Type II (120 min @ 0.5 mg/mL)	766
Type II (120 min @ 1mg/mL)	439
Type IV (60 min @ 1mg/mL)	724
Type IV (60 min @ 0.5 mg/mL)	188
Type IV (90 min @ 1mg/mL)	1072
Type IV (90 min @ 0.5 mg/mL)	715
Type IV (120 min @ 1mg/mL)	1091 (cells from two wells)
Type IV (120 min @ 0.5 mg/mL)	348 (cells from two wells)

Table:1 A summery of flow cytometry experiment which highlights the most suitable conditions for digestion.

On the Mechanical Properties of 3D-Printed Scaffolds for Cartilage Tissue Engineering

Jennifer Si[1], Adeola Olubamiji[2, 3], Daniel Chen[2], Brian Eames[2, 3]
1: College of Engineering, University of Alberta;
2: Division of Biomedical Engineering, University of Saskatchewan;
3. Department of Anatomy and Cell Biology, University of Saskatchewan

Introduction

Three-dimensional (3D) printing techniques have emerged recently to fabricate scaffolds for various tissue engineering applications. One important barrier is the inability to fabricate scaffolds with the mechanical properties that match those of the tissue at the site of implantation, which is particularly true for cartilage tissue engineering [1]. It was reported, for example, that the compressive moduli of scaffolds made from polycaprolactone (PCL) have the values many times greater than the moduli of the cartilage in the human body, in a range of 0.45-7.75 MPa [2]. This difference in elasticity can significantly vary the transfer of oxygen, nutrients, and waste to and from the cells in comparison to the environment *in vivo* [3]. This research was aimed to fabricate scaffolds with appropriate mechanical properties for cartilage tissue engineering, with emphasis on identifying the influence of pore-size and strand orientation of scaffolds on their mechanical properties.

Methods

On a 3D Bioplotter (EnvisionTEC), six types of PCL scaffolds were biofabricated with a spacing of 1.0mm, 1.5mm, or 2.0mm between strands and the strand (with a diamater of 200µm) orientation of 45^o or 90^o between the adjacent layers. Once fabricated, each scaffold was cut to have an overall size of 5 x 5 x 2.5mm for the following tests. Specifically, scanning election microscopy photo were taken to examine the scaffold structure, while compression tests were performed to characterize the mechanical properties of scaffolds.

Results

Figure 1 shows the measured compressive moduli of the six types of scaffolds. It was found that the mechanical properties of scaffolds depend on their pore-size and strand orientation, and that scaffolds with largest pore size (i.e., 2mm) at 90^o intersections between layers had lowest elasticity. Through SEM imaging, the scaffolds appear to have the structure as designed with respect to orientation and strand spacing. Furthermore, it is found that, if the strand orientation is of 45^o apart from the strand directly underneath it, the area of overlap between layers is larger, which suggests higher elastic modulus. The opposite can be observed from two strands 90^o apart, as the interconnectivity is significantly less.

Conclusions

Our results show that the larger the spacing and the smaller the area of interconnectivity between layers will result in a lower Elastic Modulus. The test yielded the lowest result of 6.91MPa from the 0-90^o/2.0mm scaffold, matching the one of natural cartilage. Further experiments will be conducted so as to characterize the biological properties of the scaffolds as applied to cartilage tissue engineering.

References

[1] Shor L, et al. *Biofabrication*, 2009
[2] Chen SS, et al. *Osteoarthritis Cartilage*, 2001
[3] Woodfield TB, et al. *Tissue Eng.* 2005

Figures

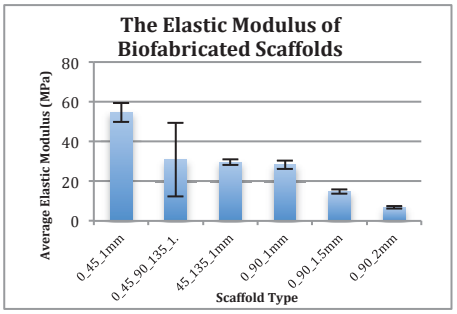

Fig. 1 Measured elastic modulus of scaffolds with varying structures.

Accounting for spatial variation of anisotropy does not improve finite element prediction of local stiffness at the proximal tibial subchondral surface

S. Majid Nazemi[1], David M. L. Cooper[1], Saija A. Kontulainen[1], Bassam A. Masri[2], David R. Wilson[2], James D. Johnston[1]

1) University of Saskatchewan, Saskatoon, SK, Canada

2) University of British Columbia and Centre for Hip Health and Mobility, Vancouver, BC, Canada

Introduction: The role of altered subchondral bone stiffness on cartilage degeneration and development of osteoarthritis is still unclear [1]. We previously developed Quantitative Computed Tomography-based Finite Element (QCT-FE) modeling of proximal tibia for non-invasive prediction of stiffness at the subchondral surface [2]. QCT-FE explained 75% of the variance in measured stiffness with 19.4% error using Goulet, [3] and Snyder and Schneider [4] with isotropic density-modulus relationships for trabecular and cortical bones [2]. Tibial trabecular bone has, however, been shown to be at least orthotropic in anisotropy [5]. The objective of this study was to investigate the effect of accounting for spatial variation of anisotropy on the accuracy of QCT-FE for predicting local stiffness at the proximal tibial subchondral surface.

Methods: Stiffness was measured at the subchondral surface of 13 media/lateral tibial compartments using *in situ* macro indentation testing (total of 47 indentation sites) [6]. The samples were then imaged using QCT and converted to FE models as described in detail elsewhere [2]. Image voxels were differentiated into trabecular and cortical using a threshold density of 0.5 g/cm^3. A uniform elastic modulus of 19.8GPa was initially assigned to cortical voxels. Fabric was calculated using grey-scale structure tensor (GST) for trabecular voxels [7]. Fabric eigenvalues together with imaged density were converted to orthotropic stiffness entries using Cowin's fabric-elasticity equations [8], and mapped to the corresponding FE models using custom algorithms. Local stiffness was calculated at each indentation site in the corresponding FE models. Cortical elastic modulus was scaled until the minimum error between FE-predicted and measured stiffness was obtained. The accuracy of QCT-FE was then evaluated in terms of linear regression and normalized root mean squared error (RMSE%) between QCT-FE predicted and measured stiffness.

Results: When accounting for bone's spatial variation of anisotropy, QCT-FE explained 75% of the variance in measured stiffness (Fig 1). The slope and intercept of the linear regression were not significantly different from unity and zero, respectively (Fig 1). RMSE% was 11.7% with an effective cortical modulus of 7.86GPa.

Conclusions: Accounting for spatial variation of trabecular anisotropy did not markedly improve prediction of local stiffness at the proximal tibial subchondral surface using QCT-FE. Improved predictions may be achieved by accounting for cortical bone heterogeneity.

References: [1] Goldring S R, 2009. [2] Nazemi S M et al, 2015. [3] Goulet R W et al, 1994. [4] Snyder S M and Schneider E, 1991. [5] Ashman R B et al, 1989. [6] Johnston J D et al, 2011. [7] Tabor Z and Rokita E, 2007. [8] Cowin S C, 1985.

Figures

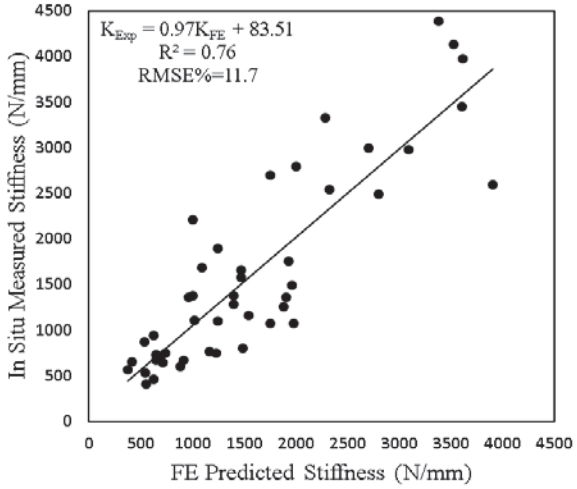

Fig 1. Linear regression between FE-predicted and measured stiffness

3D Printing's Application to Surgical Simulation and Animal Prosthetics

Douglas Kondro, Mark Ungrin, Daniel Pang, Carolyn Anglin
University of Calgary 3330 Hospital Drive N.W
Calgary, AB, T2N 4N1

Introduction

The emergence of 3D Printing has given rise to the ability of creating complex 3D objects from computer models. Though 3D printing faces notable limits on size, materials, structure and production time, its uses are numerous. In particular two applications of 3D printing were investigated: 3D printings use in Teaching Simulators and Animal Prosthetics.

Traditionally practitioners gain experience of a surgical procedures through practice on cadavers and in the operating room which is expensive and dangerous respectively[1]. Some procedures, such as an epidural, are not practiced in the clinic as often as they could despite veterinarians being authorized to do the procedure. The first project worked to develop a dog epidural model. It is hypothesized that 3D printing could play a large role in the production of teaching simulators by capturing essential geometrical data and reproducing them with materials of similar properties to tissue.

During the course of the summer a side project was developed in response to contact from the Calgary Bylaw Services who had received a rooster who had lost his toes from frostbite. The goal of this project was to create personalized prosthetics for the rooster that would allow him to walk. This project received international publicity.

Methods

To create the teaching simulators and prosthetics the following steps were followed:

- Obtain a 3D virtual model
- Print the model
- Utilize the 3D printed model, directly or through casting processes.

For the dog epidural model, the first step was done using a CT scan of a dog that was segmented for the bone and soft tissue and rebuilt into a 3D model. For the rooster project the stumps of the rooster were moulded, cast then 3D scanned. Once the 3D models were printed the dog epidural model required the print to be moulded and cast in a different material. The rooster project used the 3D prints directly.

For both of these project the success was measured subjectively through feedback from veterinarians and the ability to make the rooster walk, for the epidural model and rooster project, respectively.

Results

A dog epidural model was created that worked to mimic the geometry and feel of a real dog. The 3D prints were used indirectly. The lumbosacral space was made accessible in the model and provided the necessary physical characteristic i.e. negative pressure. Positive feedback was given on the model.

The rooster project was successful in creating a custom prosthetic that allowed the rooster to walk once again.

Conclusions

3D Printing has a strong potential for application in surgical simulators and animal prosthetics. Further research will need to be done on each project.

For the dog epidural model quantification of the materials used to prove that they exhibit tissue properties is being studied. A further study will be completed to investigate if and to what extent do these surgical simulators enhance the ability of a practitioner to complete an epidural.

A universal rooster prosthetic is being developed and its performance will be compared to that of the custom prosthetic. Quantification of the improvement of the quality of life of the rooster will also be completed.

References

1. A.M Nowitzke, Assessment of the learning curve for lumbar microendoscopic discectomy, Neurosurgery. 56 (4), 2005

Optimization of a Monopolar Surface EMG Current-Amplifier

Daniel Comaduran Marquez[1], Kartikeya Murari[2], Vinzenz von Tscharner[3], and Benno M. Nigg[3]
[1]Biomedical Engineering Graduate Program, [2]Schulich School of Engineering and [3]Faculty of Kinesiology,
University of Calgary

Introduction

The principle of bipolar potential electromyography (EMG) has been the same for decades. The signals are acquired in either a monopolar or bipolar configuration with a high impedance differential amplifier [1]. In contrast, previous research describes a new method to detect muscle activity [2]. The new method relies on currents instead of potentials to monitor muscle activity. Von Tscharner et al. states that the current-amplifier configuration is essential to quantify the synchronization of the muscle activity [2]. The electronic design of the current-amplifier uses passive filters and feedback loops to diminish frequencies outside of the range of interest (10 to 500 Hz); however, the rejection of these undesired components is not enough. This causes the amplification of signals outside of the range of interest, leading to an inaccurate EMG. In this work we present a new design for the current-amplifier that improves the rejection of frequencies outside of the range of interest.

Methods

System design and simulations were done with the use of Multisim 14.0 (National Instruments, Austin, US). The new amplifier uses a 4th order high pass filter with a cutoff frequency of 10 Hz and a 2nd order low pass filter with a cutoff frequency of 1 kHz. Both filters were designed using a Sallen-Key topology with a Butterworth response. Following frequency response simulations, the new and original amplifiers were prototyped on a breadboard for further characterization.

The amplifiers' ability to reject low frequency signals (drift) was investigated on one subject. The amplifiers were connected to the subject's *biceps brachi* muscle after proper skin preparation. The subject was asked not to contract the muscle for 15 minutes and EMG was recorded.

Results

Simulation of the frequency response of the original and the new amplifier are shown in figure 1. The new design possesses a more constant amplification of the signal in the range of interest. The active filters in the new design reduce the signals below and above the region of interest with a steeper slope. A different gain in the passband region has been selected for future projects (i.e. recording from the *vastii* muscles).

For the drift test, the new design maintains a constant signal throughout the test while the original amplifier is affected by the drift (figure 2).

Conclusions

With the implementation of active filters the frequency response and drift resistance of the original current-amplifier were improved. These design changes lead to the acquisition of a more reliable EMG.

References

[1] P. Konrad, "The abc of emg," *A Pract. Introd. to Kinesiology*, pp. 1–60, 2005.
[2] V. von Tscharner, C. Maurer, F. Ruf, and B. M. Nigg, *J. Electromyogr. Kinesiol.*, vol. 23, no. 5, pp. 1044–1051, 2013.

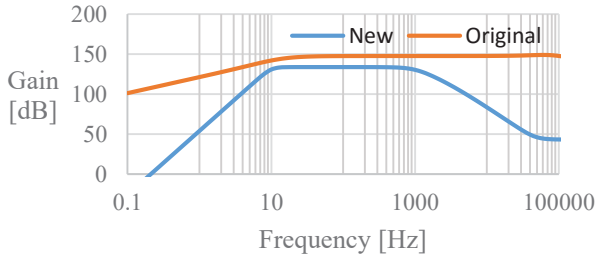

Figure 1. Magnitude frequency response of the original and new current-amplifiers.

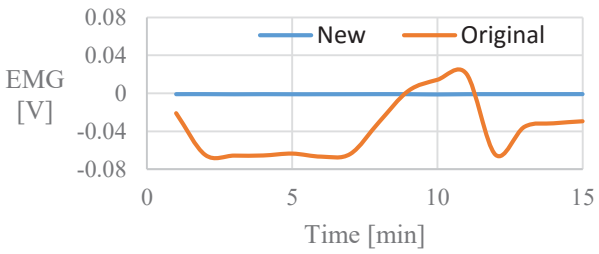

Figure 2. Response to skin drift of the original and new current-amplifier

Investigation of Toe Tip Necrosis Syndrome Using Biomechanical Testing and High Resolution Imaging

Dustin Eichhorn[1], James D. Johnston[1, 2], Murray Jelinski[3], Alex Sacher[2]
1-Biomedical Engineering Department, University of Saskatchewan, Saskatoon, SK, Canada
2-Mechanical Engineering Department, University of Saskatchewan, Saskatoon, SK, Canada
3-Western College of Veterinary Medicine, University of Saskatchewan, Saskatoon, SK, Canada

Introduction

Lameness in Feedlot cattle is a major concern in Western Canadian beef industry and associated with both animal welfare and economic loss. Toe Tip Necrosis syndrome (TTNS) is a disease that causes lameness in feedlot cattle by infecting the soft tissue and the P3 pedal bone [1,5,6]. The literature contains little information about TTNS. It has been described in both dairy cattle [5] and in feedlot cattle [6]; however, the cause is unknown. One hypothesized cause is a weakness in the claw capsule along the 'white line' – the region in which the claw horn meets the sole of the hoof [4] - which separates due to mechanical abrasion or fatigue failure, leading to foreign material entering the claw (aka 'pathway' hypothesis)[1].

Using mechanical testing and high resolution imaging, the objective of this research is to test whether mechanical abrasion and fatigue loading lead to pathway development, thereby encouraging TTNS.

Methods

Overview: This research will consist of two main approaches: (1) static and fatigue loading of a bovine claw while imaging the 'white line'; and (2) high resolution imaging of a claw under load.

Approach 1: A testing system was designed using a MTS material testing system (BIONIX) to test static, fatigue, and shear loading scenarios on the bovine claw while simultaneously imaging underneath the claw (Logitech webcam C270) through an acrylic loading platform.

Mechanical testing: The testing apparatus was designed to handle multiple tests at a maximum 6 kN -testing load for bovine claw [2, 3]. Static testing will include infected and healthy specimens at different contact angles, different degrees of damage, and combined loading to simulate bovine gait. Fatigue testing will be performed to evaluate the effect of fatigue damage on pathway development. Shear loading will mimic bovine gait and activity.

Imaging**:** Using the underside camera, video will be captured of the claw during mechanical testing. The video will be analyzed in Matlab in single frames to evaluate pathway development.

Approach 2: A radiolucent testing apparatus was developed [7] and adapted for compressive testing of the bovine claw in a high resolution peripheral quantitative computed tomography (HR-pQCT) scanner (XtremeCT, 42micron isotropic voxel size).

Mechanical Testing: the Zwick actuator is capable of applying up to a 6 kN load to the bovine claw in compressive stepwise increments to evaluate pathway formation.

HR-pQCT Imaging: High resolution imaging will create 3D images of the bovine claw under load. This will allow visualization of any micro cracks that occur. These micro cracks can then be classified by force applied and size of the crack to evaluate whether TTNS potentially occurs due to pathway development

Results to Date

The work is currently ongoing. Testing methods have been developed and apparatuses are being constructed.

Anticipated Conclusions: This research will prove/disprove the 'pathway' hypothesis regarding the development of TTNS. As well, this research will provide new insight regarding TTNS and potentially identify preventative measures.

References

[1] Jelinski M. Investigation of "P3" necrosis in feedlot cattle. ADF. August 2014. University of Saskatchewan.
[2]Franck A, Verhegghe B, De Belie N. The effect of concrete floor roughness on bovine claws using finite element analysis. J Dairy Sci, 2007; 91:182-192.
[3]Hinterhofer, C. et. al. A finite element model of the bovine law under static load for evaluation of different flooring conditions. New Zealand Veterinary Journal, 53:3, 165-170. Feb. 18th 2011.
[4]Collis V. et. al. Testing White line strength in the Dairy Cow. J.Dairy Sci. 87:2874-2880.
[5]Dewes, H.F. Transit-related lameness in a group of Jersey heifers. 1979. New Zealand Veterinary Journal. 27:4
[6] Sick, L. et al. Toe abscesses in recently shipped feeder cattle. Veterinary Medicine / Small Animal Clinician, 1982; 77, 1385-1387.5.
[7] Sacher A. et al. Validating FE-derived internal bone strain using high resolution imaging and material testing. AB BME conf. 2015.

Micro-tissue engineering for Retinal Transplants

Abdullah Al-Ani, Kayla Giles, Yacine Touahri, Derek Toms, Eko Raharjo, Shabaan Abdo, Jeff Biernaskie, Carol Schuurmans, and Mark Ungrin
University of Calgary, Calgary, AB

Introduction

Over 100 million people worldwide are visually impaired due to retinal degenerative diseases such as age-related macular degeneration. This group of diseases leads to irreversible loss of light sensitive photoreceptors. Current treatments primarily aim to slow photoreceptor loss. In contrast, cell replacement therapies promise to regenerate diseased retinas; however, a major challenge is minimal survival and engraftment of transplanted photoreceptors. The absence of healthy retinal pigment epithelium (RPE), the layer responsible for providing trophic support to photoreceptors under physiological conditions, is likely to play a significant role. To address this, we are employing micro-scale tissue engineering techniques to develop an effective retinal cell delivery system that improves transplant survival and integration. **We hypothesize that co-culturing immature cone photoreceptor with RPE cells as retinal sheets (2D) and aggregates (3D) will enhance *in vitro* photoreceptor survival, maturation, polarization and axonal outgrowth, compared to single cell suspension**

Methods

Photoreceptors from P4 $NRL^{-/-}$ Ccdc136-GFP mice are co-cultured with $mCherry^{+}$ RPE cells as 2D and 3D micro-tissues, and are characterized for: (1) interactions between RPE and photoreceptors using live-cell imaging; and (2) cone survival, maturation, and axon outgrowth using immunocytochemistry, RT-PCR and confocal microscopy. Moreover, the effect of RPE maturation on photoreceptor survival was tested by seeding photoreceptors over RPE with various maturation stages. The effect of RPE conditioned media on photoreceptor survival was also examined using Alamar Blue assay.

Results

I have created 2D and 3D transplantable micro-tissue containing RPE and cone photoreceptor. Cone photoreceptors are isolated from genetically modified (transgenic) $NRL^{-/-}$ mice that have cone enriched retinae, increasing the percentage of cones from 1% to 70% of the overall retinal cells. We have shown that these micro-tissue constructs are able to significantly improve the survival of photoreceptors *in vitro.* Moreover, we have partially isolated agents secreted by cultured RPE that are responsible for this improved photoreceptors survival, and are in the process of identifying whether this activity is due to known factors or a novel mechanism. These micro-tissue are currently being further evaluated *in vitro* to define the best culturing conditions for optimal cone survival and function. Subsequently, the optimized micro-tissue will be transplanted to blind mice to determine their therapeutic potential by evaluating their capacity to restore vision in blind mice.

Conclusions

We were able to successfully construct 3D and 2D retinal micro-tissue. Our results suggest that culturing photoreceptors over mature RPE significantly improve their survival. This is of a great significance as one of the biggest obstacle facing cell replacement therapy is keeping transplanted cells alive. Overcoming this obstacle is an essential step in the road of correcting the presently irreversible vision loss associated with retinal degenerative diseases.

Image Analysis Of Tissue Alignment For Assessing Injury and Repair in Multiple Sclerosis

Shrushrita Sharma[1 2 4], Yunyan Zhang[1 3 4]
[1]Biomedical Engineering Program, Schulich School of Engineering, [2]Departments of Radiology and [3]Clinical Neurosciences, [4]Hotchkiss Brain Institute, University of Calgary

Introduction

Multiple Sclerosis (MS) is an autoimmune neurodegenerative disorder in the central nervous system with significant loss of nerve sheath (demyelination) and nerve fibers [1]. Remyelination is believed to have the potential to protect neurons and nerve fibers; however, neither demyelination nor remyelination can be identified using conventional analysis in magnetic resonance imaging (MRI) [2]. MRI has been the mainstay for assessing outcomes of MS. MR-based lesion activity and lesion burden are often used as primary outcomes of treatments in clinical trials of MS, although the severity of pathology in these lesions is subject to confirmation. To accurately evaluate disease activity, I am developing quantitative measures to assess the alignment of tissue structure based on image processing and analysis strategies [3]. I hypothesize that changes in tissue pathology will lead to changes in the directionality of MRI signal intensity; specifically, demyelination will interrupt the alignment of nerve fibers that can be restored by remyelination or repair.

Materials and Method

1) Technique: I am developing a new measure of tissue directionality based on fast Fourier Transform (FT). The FT calculates the entire frequency content enclosed in an image. For this study, I computed the power spectrum of the FT, performed polar conversion of the power spectrum after normalization and thresholding to improve quality and reliability, and plotted the orientation and entropy of the images using the software program I built. Lower angular entropy refers to higher directionality.

2) Validation: a) I used two sets of simulation images: the first set with visible directionality and the second set with no dominant orientation; b) I assessed MRI scans from healthy subjects participated in a clinical study of MS. Here, I focused my testing on the corpus callosum, which is the largest interhemispheric white matter structure with highly organized nerve fibers. I selected six regions of interest (ROIs) that were located at the left, center and right aspects of the anterior (genu) and posterior (splenium) parts of corpus callosum.

Results

I found that the directional outcomes derived from the power spectrum of the FT corresponded to the alignment of structures shown in the simulated images. That is, highly aligned structures appeared more elongated in the shape of power spectrum indicating more anisotropic than the structure with random orientations. In the corpus callosum of human brain, the left and right ROIs of both genu and splenium demonstrated alignment at 135 and 45 degrees, corresponding to their physical orientations at respective locations; no clear alignment information was identified in the central ROIs of the corpus callosum. Quantitative orientation indices including angular entropy confirmed these findings.

Conclusions and Discussions

Our results show that measures of orientation and its entropy using the power spectrum of FT can identify structural alignment in an image. The FT has been used widely to study structure composition but not so much in assessing tissue anisotropy. Through testing with both simulated and MR images, I found that quantitative assessment of the power spectrum could be a promising means to identify tissue property based on clinical MRI. I will test the utility of this approach to evaluate de- and re-myelination in patients with MS and other similar disorders.

References

1. Ge. Y., (2006). *Am. J. of Neuroradiology, 1165-1176.*
2. Begin, S., (2013). *Biomedical Optics EXPRESS, 4(10).*
3. Bayan, C., (2009). *J. of Applied Physics, 105(10).*

An Increased Proportion of Weakly Bound Cross-bridges Contribute to the Age-related Maintenance of Eccentric Strength

Nordan Flaaten[1], Geoffrey A. Power[1,2],Walter Herzog[1]
[1]Faculty of Kinesiology, Human Performance Laboratory, University of Calgary, Calgary, Alberta, Canada
[2]Department of Human Health and Nutritional Sciences, College of Biological Sciences, University of Guelph, Guelph, Ontario, Canada
nordan.flaaten@gmail.com

Introduction

Despite a clear age-related reduction in force during shortening muscle actions (1-2), the ability to produce force during active lengthening contractions (i.e., eccentric) is well-maintained with natural adult aging (3, 4). This maintenance of eccentric force is well-characterized across various muscle groups (5-6). However, the mechanisms contributing to this phenomenon are unclear. In this study we altered muscle temperature, thereby changing cross-bridge kinetics and the ratio of weakly to strongly bound cross-bridges in an attempt to study cross-bridge-based mechanisms of age-related maintenance of eccentric strength.

Methods

Electrical activation of the adductor pollicis was administered during lengthening (20-320°·s^{-1}) contractions in 24 young (~24years) and old (~72years) males across muscle temperatures (Cold;~19ºC, Normal;~30ºC, Warm;~35ºC).

Results

Old were 20-30% weaker for the normal and cold conditions ($P<0.05$) with no difference for the warm condition compared to young ($P>0.05$). Half-relaxation time did not differ across age for the normal and warm temperatures ($P>0.05$), but slowed significantly for old in the cold condition compared with young (~15%; $P<0.05$), as well, there was an increase in stiffness. There was no difference in ECC:ISO across age for normal and warm conditions ($P>0.05$), but for the cold, the old exhibited a 20-35% higher ECC:ISO than young for velocities above 60°·s^{-1} ($P<0.05$). Further, ECC:ISO was 50-60% greater for the cold condition than the normal and warm.

Conclusions

We confirm here that the eccentric to isometric force production ratio is maintained with adult aging in an electrically activated muscle *in vivo*. We contest that this maintenance is not entirely owing to the adult aging process, but that changes in the ECC:ISO ratio can be explained, in part, by a strong positive relationship between ECC:ISO and muscle contractile speed. We suggest that the slowing of muscle contractile properties and a greater proportion of weakly bound cross-bridges (i.e., increased stiffness and lower force in the cold condition) may be key contributors to an elevated ECC:ISO, particularly for old adults.

References

1. Power et al. (2013). *Journal of sport and health science*.
2. Power et al. (2014). *Exp Gerontol*.
3. Vandervoort. (2002). *Muscle Nerve*.
4. Roig et al. (2010) *Exp Gerontol*.
5. Porter et al. (1997). *J Gerontol A Biol Sci Med Sci*.
6. Poulin et al. (1992). *Can J Sport Sci.*

Figures

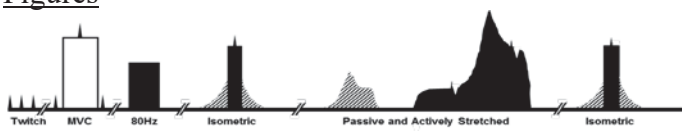

Fig. 1 Experimental Timeline

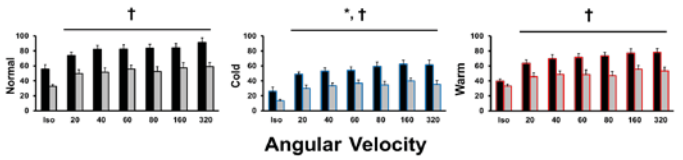

Fig. 2 Eccentric strength in young and old across lengthening velocities and temperatures

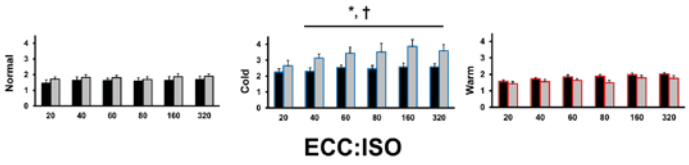

Fig. 3 Eccentric to Isometric Force Ratio in young and old across lengthening velocities and temperatures (* denotes temperature difference, † denotes age difference.

Calgary Vitamin D Trial 12 Month Pilot Data: Increased 25(OH)D is Associated with Improved Bone Density as Measured by HR-pQCT, but not DXA

Erin M. Hildebrandt [1,2], David A. Hanley [2], Steven K. Boyd [1,2]
1 Department of Radiology, Cumming School of Medicine, University of Calgary, Calgary, Alberta, Canada.
2 McCaig Institute for Bone and Joint Health, University of Calgary, Calgary, Alberta, Canada.

Introduction

The beneficial effects of vitamin D have been widely investigated, including its role bone health.[1] The 2011 Institute of Medicine report identified a Recommended Dietary Intake for skeletal health of 600 IU vitamin D/day (from all sources; dietary sources average 2-300 IU/day) and a Tolerable Upper Limit of 4,000 IU/day for adults under 70 years.[2] Benefits of higher doses of vitamin D have not been systematically explored or identified, perhaps because of safety concerns. Very high doses of vitamin D have been associated with hypercalciuria and hypercalcemia, although toxicity is usually associated with doses above 40,000 IU/day.[3-4]

Typically, clinically bone health is assessed by dual X-ray absorptiometry (DXA) estimation of bone mineral density (BMD). However, this 2D measure provides little information about bone architecture. The latest technology that is used to assess bone quality and architecture is 3D high-resolution peripheral quantitative computed tomography (HR-pQCT). This proven, reliable clinical research tool provides 3D *in vivo* images of bone architecture providing the ability to assess cortical (Ct) and trabecular (Tb) bone separately.

The present study was designed to evaluate the relationship between increased serum 25(OH)D and bone health as part of an ongoing controlled trial in Calgary by assessing changes in bone parameters measured by HR-pQCT after 12 months of supplementation in a pilot cohort.

Methods

Healthy men and women with normal parameters of calcium metabolism between 55-70 years (N=362) were recruited for a three year, randomized, double blind trial of 400, 4,000 or 10,000 IU vitamin D daily. Participants had baseline 25(OH)D levels between 30-120 nmol/L and were excluded if they had osteoporosis, medications or other conditions affecting calcium metabolism. A subset of participants (N=62; 18 M, 44 F; age 63.2 ± 4.1 yrs) formed a pilot cohort, for which we report first year parameters of bone health.

Participants were assessed at baseline, 3 months, 6 months and 12 months. Assessments included blood work, HR-pQCT scans of the non-dominant radius and tibia and DXA scans. Relationships between relative change over 12 months in 25(OH)D and all bone parameters were evaluated using linear regressions.

Results

Four participants withdrew from the study for reasons unrelated to vitamin D supplementation. At baseline average 25(OH)D was 76.2±17.4 nmol/L (min: 38.5, max: 110.0) and at 12M was 144.4±69.3 nmol/L (min: 61.1, max: 325).

At the radius and tibia, change in total BMD was not significantly associated with 25(OH)D. Change in CtBMD and TbBMD at the radius were positively correlated with change in 25(OH)D (p=0.014, r^2=0.11; p=0.02, r^2=0.11). At the tibia, change in CtBMD had no significant relationship, and change in TbBMD had a positive correlation with 25(OH)D (p=0.02, r^2=0.093). There were no significant associations between change in DXA parameters and 25(OH)D.

Conclusions

At one year, pilot participants had increased 25(OH)D, and this correlated with improvements in CtBMD and TbBMD as measured volumetrically by HR-pQCT, whereas 2D DXA imaging did not capture these changes.

References

[1] Yoshida T et al., Endo Metab Clin N Am. 2012
[2] IOM 2011. The National Academies Press. 2011
[3] Jones G. Am J Clin Nutr. 2008, 88
[4] Kimball SM et al., Am J Clin Nutr. 2006, 98(3)

LONG TERM *IN VIVO* KINEMATICS OF THE OVINE STIFLE JOINT FOLLOWING ANTERIOR CRUCIATE LIGAMENT TRANSECTION

[1,2]Norman, J L; [1]Barton, K I; [1]Atarod, M; [1,2]Shekarforoush, M; [1]Heard, B; [1,2]Sevick, J, [1]Achari, Y; +[1,2]Shrive, N G
3456 24th Avenue NW, Calgary, Alberta, University of Calgary, BME Program

Introduction

Osteoarthritis (OA), a degenerative joint disease involving the breakdown of articular cartilage, is common after injury or with aging[1]. Sheep develop trauma-induced OA at a slightly accelerated rate compared to humans but with similar patterns[2]. In an ovine knee injury model[3,4], altered gait mechanics and degradation of the cartilage have been observed 20 weeks post anterior cruciate ligament (ACL) transection (Tx) surgery. Gait alterations at 40 weeks post ACL Tx surgery remain unknown. Therefore, the objective of this study was to investigate the *in vivo* kinematics of the ovine stifle joint over time following ACL Tx.

Methods

Force Plate Testing. Three skeletally mature 3 to 4-year-old female Suffolk-cross sheep (average weight 77.1kg) were led across an embedded force platform (Kistler Instrumente, Winterthur, Switzerland) until 20 hind limb hoof strikes were recorded at 1200 Hz. Peak vertical ground reaction force was determined prior to surgical plate implantation, and then serially prior to data collection. ***Surgical Procedure.*** Bone plates were implanted onto the proximomedial aspect of the tibia and the distolateral aspect of the femur of the right hind limb, four weeks prior to kinematic testing. ***Kinematic Collection and Bone Digitization.*** A post was attached to each plate and an instrumented spatial linkage (ISL) mounted between them. The ISL consisted of six rotational encoders providing a measurement of position and orientation in six degrees of freedom (6-DOF). The *in vivo* kinematics of the stifle joint were measured while the sheep walked on a treadmill at 2 mph (0.89 m/s). Each sheep then underwent arthroscopic ACL Tx surgery on their right hind limb. The *in vivo* gait kinematics were measured again at 20 and 40 weeks post ACL Tx. The animals were euthanized after kinematic testing at 40 weeks. A coordinate measuring machine was used to measure anatomic landmarks on the bone with respect to the ISL in order to create an anatomically relevant coordinate system. ***Analysis.*** Data are presented as mean ± SD.

Results

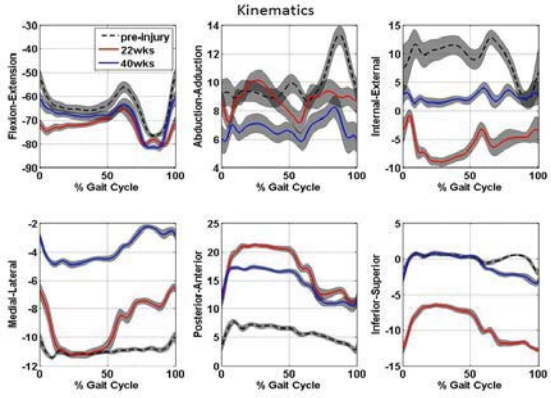

Figure 1: The 6-DOF *in vivo* gait kinematics of the ovine stifle joint, intact (black), 22 weeks post ACL Tx (red), and 40 weeks post ACL Tx (blue).

The medial-lateral as well as posterior-anterior translation of the joint is progressively altered post ACL Tx over time (Figure 1). Rotationally, the internal-external kinematic curve at 22 weeks is unlike the intact motion, however by 40 weeks recovery towards the intact measurement is seen as the animal compensates. These data indicate that the *in vivo* kinematics of the ovine stifle joint change over time following ACL Tx.

Conclusions

ACL transection causes long-term changes in the *in vivo* kinematics of the joint. ACL Tx leads to compensatory gait changes, and these altered gait kinematics may result in more rapid degradation of cartilage due to abnormal loading and repetitive wear.

References

Lohmander et al. *AJSM.* **35**(10): 1756-69, 2007.
Frank et al. JOR. **30**(3): 384-92. 2012.
Tapper et al. JOR. **26**(5): 660-72. 2008.
Atarod et al. JOR. **32**(3): 431-8. 2013.

METABOLIC EFFECTS OF DIET INDUCE OBESITY

Graham MacDonald, Paul Riek, & Walter Herzog
Human Performance Lab, University of Calgary, Alberta, Canada

Introduction

Obesity is generally defined as a condition where excess body fat has accumulated to a point where it can cause detrimental health effects [1]. Obesity in children and teenagers is becoming more common, with worldwide rates increasing by 50% in the last 30 years [2]. The purpose of the present study was to investigate how inducing obesity through a high-fat/high-sugar (HFHS) diet affects a variety of metabolic, physical, and behavioral factors when utilizing a rat model to study dietary-induced obesity. To our knowledge, an in depth analysis of metabolic parameters using this model has not been conducted based on the current literature. Expected observations included an increased caloric intake for the obese animals and no change in caloric expenditure between groups, accompanied by a decrease in activity for the obese animals once the animals began to show signs of increased fat mass.

Methods

Twenty male Sprague Dawley rats were randomly divided into two groups of ten at three weeks of age (post-weaning). The control group (CON) was fed regular rat chow and the experimental group (DIO) was fed a custom HFHS diet in order to induce obesity. Both groups were provided with food ad libitum.

From weaning until 17 weeks of age, each rat spent one 24 hour period in a metabolic chamber per week. The metabolic chambers were set up to monitor a variety of parameters. These included gas exchange (caloric expenditure), food consumption, and activity levels. At 17 weeks of age, each animal's body composition was analyzed using DEXA. Surgery was then performed, isolating the medial gastrocnemius in order to analyze muscle mechanical properties (Force-Length, Force-Velocity, & Force-Frequency Relationship). Data collection will be completed by the end of next, there for statistics have not been run on the data at this time.

Results

After 8 weeks (5 weeks on diet) the DIO group began to gain mass at a faster rate than the control group. DIO group had substantially higher activity levels in comparison to the CON group up until 8 weeks of age, at which point activity levels were similar between groups for the remainder of the experiment. Although activity levels were similar among groups after 8 weeks, caloric expenditure remained substantially higher for the DIO group for the entirety of the study. Food intake (g/day) for the entirety of the experiment were similar between groups, although caloric intake was substantially higher for the DIO group due to the caloric density of the food they were consuming. No between-group difference in RER were observed at any time point.

Conclusions

Based on the preliminary analysis of the data (statistical analysis has yet to be run) it seems as though the HFHS diet successfully induced obesity in the rat model after 17 weeks. It seems as though this is not due to excessive food consumption but due to the increased caloric density in the food being consumed by the DIO group. It is interesting to note that activity levels were substantially higher for the DIO group from weeks 5-to-8, but then leveled off and were similar among groups for the remainder of the study. It seems that once the rats had gone through puberty (rats: after ~7 weeks), substantial between group differences began to occur.

References

1. Navaneelan and Janz. *Health at a Glance*. **4**:1-10, 2014.
2. World Health Organization. *Obesity and Overweight Fact Sheet 311.* 2011.

In Situ Chondrocyte Viscoelasticity Following Static and Dyanmic Compressions

Svetlana Kuznetsova[1], Isabelle Villemure[2], Ziad Abu Sara[1], Eng Kuan Moo[1], Yasir Al-Saffar[1], Walter Herzog[1]
[1]Human Performance Lab, University of Calgary, [2] Ecole Polytechnique de Montreal

Introduction

Articular Cartilage (AC) is a thin layer of connective tissue covering bony surfaces of joints [1]. AC allows joints to move smoothly during load transmissions, and plays an essential part in the joints overall health [2]. Chondrocytes maintain the extracellular matrix of AC, the integrity of which depends largely on compressions applied to the tissue. Past studies used strain control protocols to apply static or short term dynamic compressions to AC and observed changes in chondrocyte morphology [1]. The purpose of this study was to use three different loading protocols in order to see how chondrocytes behave when undergoing static and cyclic loading at walking and running frequencies.

Methods

Patellae from New Zealand white rabbits (N=12) were isolated and randomly assigned to one of three loading protocols [2]; (i) static loading with a constant strain level of 10%, (ii) dynamic sinusoidal loading oscillating at 1 Hz (walking frequency) and an average strain magnitude of 10%, (iii) dynamic sinusoidal loading oscillating at 2 Hz (running frequency) and the same average strain level. Compression was applied for 45 min, followed by 15 min recovery. Cells were stained and tracked using laser scanning microscopy (Zeiss) during the loading protocol.

Results

For the loading period, cellular width and depth (perpendicular to the tissue thickness axis) for static loading increased on average by 10%, while cellular height (along the tissue thickness axis) decreased by approximately 20% with respect to the unloaded state (Figure 1a). Similar results were observed for width and depth for dynamic loading at 1 Hz frequency. However, unlike static loading, cellular height did not fully recover to its original state (Figure 1b). For the loading period of dynamic loading at 2 Hz, an increase in cellular depth of approximately 15% was observed along with an average increase in cellular width by 20%, while cellular height was decreased by almost 25% (Figure 1c).

Conclusions

The lack of variation between static and dynamic compressions at 1 Hz suggests that the cellular mechanical response is similar when an individual walks or stands. The cellular mechanical response for 2 Hz frequency is different from static and 1 Hz loading protocols, thus suggesting that greater changes in cellular morphologies compensate for the increase in frequency.
In the future, more studies can be conducted to evaluate how cells respond at the same frequencies but under various strain levels.

References

1. Han S, et al. *JBiomech.* **45**:2450-2456,2012.
2. Madden R, et al. *JBiomech.* **46**:554-560, 2013.

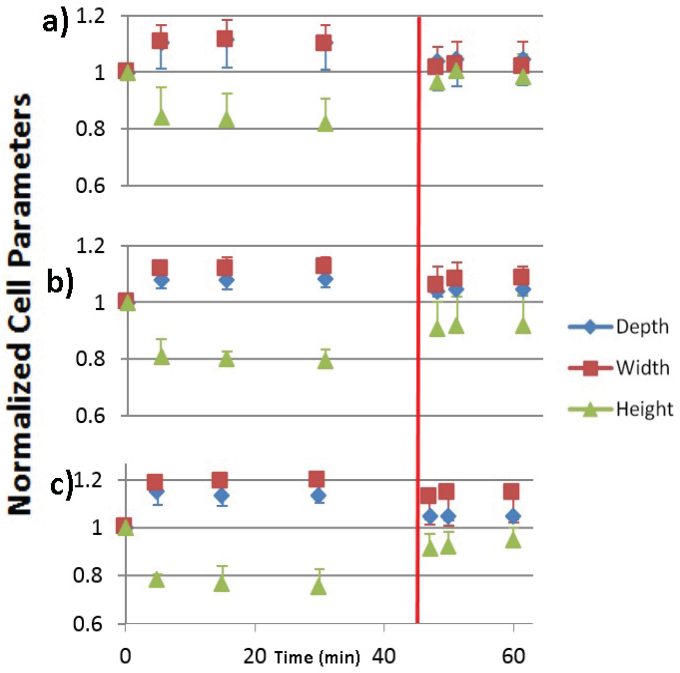

Figure 1: Normalized cell morphologies for (a) static loading (n=51), (b) dynamic loading at 1 Hz (n=35), and (c) dynamic loading at 2 Hz (n=66). Red line separates loading and recovery periods. Mean±1SD

Analysis of the Watershed Tie-zone Influence on the Skull-stripping

Roberto Souza,[1,2] Letícia Rittner,[1] Richard Frayne,[2] Roberto Lotufo[1]
[1]School of Electrical and Computer Engineering, University of Campinas, Campinas, Brazil
[2]Calgary Image Processing and Analysis Centre (CIPAC), Foothills Medical Centre, Calgary, Canada

Introduction

The watershed transform is a segmentation technique that has been applied in many problems, such as the skull stripping in MR images [1]. In skull-stripping, the goal is to extract the brain from the surrounding tissue. It is an important and frequently encountered segmentation problem with only two labels: brain and not brain. Tie-zones are a phenomenon that occur with the watershed transform where there are segmentation regions that associate the same "cost" to more than one label, but receive an arbitrary label due to implementation details of the algorithm. For instance, using the same watershed algorithm, the results can be different, if the watershed is applied to the same image rotated by 90 degrees.

Tie-zones have not been well studied. In this work, we specifically analyze the influence of tie-zones in the common skull-stripping problem. Our goal is to demonstrate that tie-zones have considerable impact on the segmentation results and, therefore, should be considered when developing biomedical image segmentation applications.

Methods

Ten T1-weighted MR images, collected at the University of Campinas, Brazil, were used in these experiments. Positive (brain) and negative (not brain) markers for the watershed transform were chosen based on the max-tree results. Then, the tie-zone watershed [2] was run using these markers. The max-tree and the watershed threshold algorithms were applied directly to the 3D volume.

We visually analyzed the resulting images. In order to better evaluate the tie-zones, we considered two scenarios: the tie-zones were assigned the brain label or non-brain label, leading to a maximal brain volume or minimal brain volume, respectively. For quantitative assessment, we computed the average, the maximum and the minimum deviation of the maximum brain volume with respect to the minimum brain volume.

Results

Brain extraction was successful in all cases. The brain volume deviation (Table 1) showed that the tie-zones have a significant influence on the segmentation results. Fig 1 provides examples of that influence.

Table 1: Average, maximum and minimum deviation of the maximum brain volume normalized by minimum volume.

Average (std dev)	8.40% (0.92)
Maximum	10.08%
Minimum	6.80%

(a)

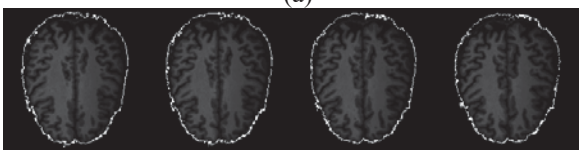

(b)

Figure 1: Influence of the tie-zones in the brain extraction. (a) Slices closer to the top of the brain, (b) central slices of the brain. The white regions are the tie-zones.

Conclusions

We have shown that the tie-zones of the watershed transform have considerable influence on skull-stripping results. As future work, we intend to further investigate solutions to the tie-zone problem. One option would be to assign the tie-zone pixels to brain/non-brain based on local criteria near the tie-zone and surrounding regions.

References

[1] Hahn and Peitgen. The Skull Stripping Problem in MRI Solved by a Single 3D Watershed Transform. In Proceedings of the Third International Conference on MedicalImage Computing and Computer-Assisted Intervention, 2000.

[2] Audigier, Lotufo, and Couprie. The tie-zone watershed: definition, algorithm and applications. IEEE International Conference on Image Processing, 2005.

Factors Affecting Cell Viability and Recovery Under Shear Stress

Jingxuan Zhao[1], Liqun Ning[1], Arthur Guillemot[2], Georges Kipouros[3], and Xiongbiao Chen[1]
1. Department of Mechanical Engineering, University of Saskatchewan; 2. ICAM School of Engineering, France; 3. Department of Chemical and Biological Engineering, University of Saskatchewan

Introduction

Based on three-dimensional printing technology, cell-encapsulated gels can now be dispensed layer by layer to create scaffolds for tissue engineering [1]. This process offers greater encapsulation of cells in scaffolds, allowing closer replication of the structure of native tissue; however, cells may be damaged during dispensing due to process-induced forces, such as shear stress [1,2]. Current research has shown that the mechanical strength of the gel affects the cell viability, and that an alginate gel with lower molecular weight results in higher cell viability, upon injection through a syringe [2]. Although effects of the dispensing process on cell viability have been reported [1,2], rarely are the recovery and proliferation of the encapsulated cells examined. The objectives of our research were to examine the factors affecting the recovery and proliferation of cells under shear stress, with emphasis on the influence of alginate concentration, exposure time, and cell density.

Methods

The samples were prepared by encapsulating cells from the cell lines L8 (myoblast), RSC96 (Schwann cell), and 3T3 (fibroblast) in DMEM-dissolved alginate, respectively. A rheometer applied shear stress on the cells, as experienced in the dispensing process, at a constant rate of 40 RPM and temperature of 21°C. When used as a constant, alginate concentration was 2.0% w/v, exposure time was 60 s, and cell density was 1×10^6 cells/mL. For testing, alginate concentration was 1.5% or 2.5% w/v; exposure time was 30 or 120 s, and cell density was 5×10^5 or 1×10^7 cells/mL. Three runs were repeated for each of the aforementioned conditions. Upon being sheared in the rheometer, the samples were transferred to 12 well plates and incubated over 3, 6, and 48 hours for testing. MTT Assay was used to measure the proliferation of cells. Live/Dead Assay was performed using calcein-AM and propidium iodide (PI) to determine the cell viability. Hoechst and PI were used to stain the cells for fluorescent plate reading in order to verify the Live/Dead Assay results.

Results

For all cell lines used, the exposure time of 120 s resulted in lower total cell count (Fig.1) and higher dead cell percentage after 48 hours, as compared to 30 s of exposure time. The samples encapsulated in 2.5% w/v alginate also resulted in lower total cell count and higher dead cell percentage as compared to 1.5% w/v. The cell density of 1×10^7 cells/mL resulted in higher total cell count and lower dead cell percentage after 48 hours than 5×10^5 cells/mL. Also, the sheared samples demonstrated lower total cell counts (Fig.1) and higher dead cell percentages as compared to the controls that were not sheared.

Conclusions

Higher exposure time and alginate concentration resulted in lower cell viability and proliferation after the recovery period of 48 hours, while higher cell density produced higher cell viability and proliferation. Furthermore, the proliferating ability of the cells was lower in the sheared samples. When dispensing cell-seeded gels, the dispensing time and gel viscosity should be minimized, and a high cell density should be used, in order to achieve high cell viability and recovery.

References

[1] Li, M G et al. (2009) Biofabrication. 1:1-10.
[2] Aguado, BA et al. (2012) Tissue Eng. 18:806-15.

Figures

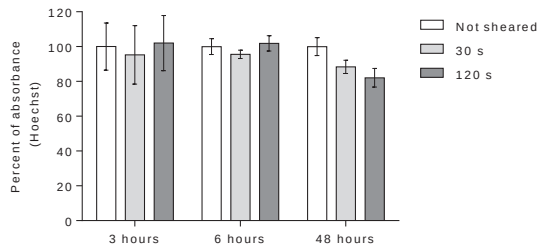

Figure 1. % Absorbance of Hoechst in L8 for 30 and 120 s exposure times; Hoechst stains live and dead cells.

Evolution of Helmet Strain Energy in Linear Impacts with Helmet Accessories

Henry Y. Yu, Christopher R. Dennison
Biomedical Instrumentation Laboratory, Department of Mechanical Engineering, University of Alberta, Edmonton

Introduction

In 2010-2011, cycling injuries were 22.5% of all major sports and recreational injuries in Canada [1]. Head injuries are one of the greatest risks to cyclists, accounting for 1/3 of emergency department visits, 2/3 of hospital admissions, and 3/4 of deaths [2]. Helmets reduce the likelihood of injury by redistributing impact loads and reducing peak forces. With increasing use of helmet accessories (e.g. cameras), the effect these accessories could have on head injury risk has become a concern for standards and biomechanics communities. In our first studies investigating the effects of helmet accessories on head injury risk [3], it was found that presence of a camera accessory did not appear to increase risk of skull fracture. However, helmets with camera accessories experienced significantly more damage, localized in the region of the accessory [3]. The next stage of our studies will quantify the dissipation of strain energy during impact within the shell and liner. We hypothesize that the helmet is managing more strain energy when fit with a helmet accessory, and knowledge of this energy will lead to understanding material failure modes in the helmet and could be of interest to manufacturers and certifying organizations.

Figure 1: Helmets after impact without accessory (left) and with camera accessory (far right) at 4m/s impacts [3].

Methods

Bicycle helmet impacts will be simulated with and without camera accessories using the University of Alberta impact test-bed. Direct frontal impacts to the accessory will be simulated. The HybridIII (Hy3) headform and associated instrumentation will be used to measure impact kinematics. Miniature in-situ optical fibre strain sensors will also be integrated into the helmet shell and liner adjacent to the helmet accessory.

Results

In our previous investigations of effects of camera accessories, helmet damage was localized around the accessory with significant liner fracture and reduction in thickness. Force transducers integrated with the Hy3 [3] showed that skull forces were decreased despite the presence of a camera (Figure 2).

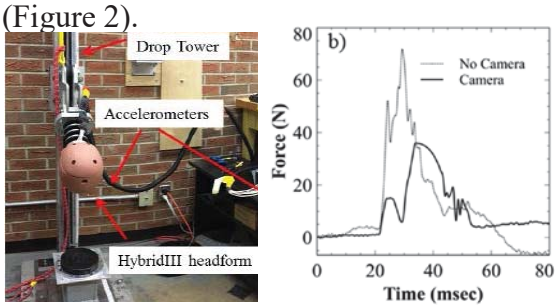

Figure 2: (left) test-bed; (right) impact force versus time of force transducer for a single helmet for 6m/s impacted helmets. Sum of peak helmet forces were reduced from 335.0 N to 221.9 N ($p<0.02$) without a helmet. [3].

Discussion

Hypothesizing that helmets with camera accessories absorb more energy in a localized area, it is expected that these helmets will fail at lower velocity impacts (compared to a helmet without an accessory) and possibly expose the head to increased risk of focal head injury. This difference in failure velocity will be determined. Furthermore, the implementation of strain sensors in the helmet will allow for the evolution of strain to be understood in helmet impacts. This understanding could inform both helmet manufacturers and certifying organizations of the key mechanics that should be considered when assessing head protection in impacts involving accessories.

References

[1] National Trauma Registry Report 2013: Hospitalizations for Major Injury in Canada, 2010-2011. CIHI.

[2] Thompson, D.C., et. Al. 1999. In: The Cochrane Collaboration, Rivara, F. (Eds.), Cochrane Database of Systematic Reviews.

[3] Butz RC et al. (2015) Effects of external helmet accessories on biomechanical measures of head injury risk: an ATD study using the HybridIII headform. (in-press) J Biomech.

Increasing serum 25(OH)D improves balance after one year: Pilot results

Ghazavi, N.[1,2]; Hildebrandt, E.M.[2,3]; Burt, L.A.[2,3]; Hanley, D.A[2,3]; Boyd, S.K.[2,3]
1. Schulich School of Engineering, University of Calgary, Calgary, AB; 2. McCaig Institute for Bone and Joint Health, University of Calgary, Calgary,AB; 3. Department of Radiology, Cumming School of Medicine, University of Calgary, Calgary, AB

Introduction

Osteoporosis is a common bone disease, caused by a reduction in bone density, increasing the risk of fracture, [1] which is associated with increased mortality and financial cost [2]. It has been shown that 80-90% of hip fractures are associated with falls [3]. Effective strategies to prevent fall related fractures include increasing femoral bone density, balance and muscle improvements [4]. Aging negatively affects sensory systems (vision, somatosensory and vestibular), which leads to balance impairment in elders [5]. It has been suggested that vitamin D supplementation could improve these balance impairments in older adults; however, the current results are mixed [6, 7]. This research displays preliminary data from the pilot study of a double-blind randomized control trial (RCT), investigating dose-dependent longitudinal effects of vitamin D supplementation on bone health. The objective of this research was to assess the relationship between serum 25(OH)D concentration on balance.

Methods

This study assessed pilot participants from a three-year double blind RCT after one year. At baseline 62 healthy participants (18 M, 44 F, mean age 63.2 ± 4.1 years) were assigned to one of the three daily doses of 400, 4,000 or 10,000 IU vitamin D3. Serum 25(OH)D was measured at baseline, 3, 6 and 12 months. Change was measured as the difference between 12 months and baseline. A Biosway machine (950-460, Biodex, New York, United States) was used to assess postural sway under a variety of sensory conditions. Center of Pressure (COP) movement was measured on firm and foam surfaces with eyes open and closed in 30 seconds at a rate of 20 Hz. Time and frequency domain sway measures based on COP movements were computed with a MATLAB code in Medial-Lateral (ML), Anterial-Posterial (AP) and Resultant (RD) directions [8]. Relationships between serum 25(OH)D and sway measures were evaluated using Pearson correlation coefficients (SPSS 22).

Results

Serum 25(OH)D level was negatively associated with 95% power frequency-AP (p=0.046, r=-0.255) and centroidal frequency-AP (p=0.029, r=-0.277) on the firm surface with eyes open at baseline. Change in serum 25(OH)D level was negatively associated with the change in 95% power frequency-AP on the firm surface with eyes open (p=0.048, r=-0.266) and closed (p=0.013, r =-0.329), 50% power frequency-AP on the foam surface with eyes open (p=0.009, r=-0.344) and closed (p= 0.004, r=-0.383), mean frequency-ML on the foam surface with eyes open (p=0.039, r=-0.276) and closed (p=0.004, r=-0.375) and centroidal frequency-AP on the foam surface with eyes closed (p=0.007, r=-0.359).

Conclusions

The results suggest a significant association between serum 25(OH)D level and balance. With an increase in 25(OH)D, sway measures were negatively associated, suggesting better balance. This study is the first to assess the relationship between vitamin D and balance based on time and frequency domain COP-based measurements.

References

[1] Tuchendler et *al*., Thyroid Research.2014, **7**(1); [2] Annweiler et al., Neuroengineering and Rehabilitation. 2010, 7(50); [3] Baker et al., Clinics in geriatric medicine, 1985, 1(3); [4] Nguyen et al., BMJ, 1993, 307(6912); [5] Keller et al., Muscles, Ligaments and Tendons Journal, 2013, 3(4); [6] Muir et al., American Geriatrics Society, 2011, 59(12); [7] Uusi-Rasi K et al., JAMA Intern Med ,2015 , 175(5); [8] Prieto et al., Trans Biomed Eng, 1996, 43(9)

Is titin responsible for force enhancement in skeletal muscle?

Shuyue Liu, Venus Joumaa and Walter Herzog
University of Calgary, Human Performance Laboratory, Calgary, Alberta, Canada

Introduction

Force enhancement is the force increase observed at the steady state after active stretch of muscles compared to the purely isometric force at the corresponding length [1]. The mechanism responsible for force enhancement is still unknown. It has been proposed that force enhancement might be associated with the passive force produced by titin. Titin is a large sarcomeric protein that connects the Z line to the M line in each half-sarcomere and it is the structure responsible for most of the passive force in skinned skeletal muscle fibres. It has been suggested that titin's stiffness might increase, or characteristic length decrease, with activation resulting in the force enhancement observed when muscles are actively stretched [2].

The purpose of this study was to investigate the role of titin in force enhancement by testing force enhancement in titin-intact skinned fibres and skinned fibres in which titin had been partially degraded using trypsin. Our hypothesis was that force enhancement would be greater in titin-intact fibres compared to titin-partially-degraded fibres.

Methods

Skinned fibres were isolated from NZ white rabbit psoas muscle. Force enhancement was measured at average sarcomere lengths (SLs) of 3.0 μm and 3.4 μm in two groups of fibres. The first group consisted of titin-intact skinned fibres (n=18). The second group was formed of fibres that had been incubated for 3 minutes in a solution containing 0.25 μg/mL of trypsin (n=17). Trypsin at very low concentrations (0.25 μg/ml) has been shown to selectively degrade titin [3]. Titin degradation was assessed by investigating the decrease in passive force observed after a stretch from a SL of 2.4 μm to a SL of 3.0 μm.

Results and Discussion

The reduction in passive force due to trypsin treatment in titin-partially-degraded fibres was 31.2%. Titin degradation did not affect purely isometric active force. No difference in force enhancement was observed at a SL of 3.0 μm between the titin-intact fibres (5.2±1.2%) and titin-partially-degraded fibres (5.9±1.1%). At a SL of 3.4 μm, force enhancement was greater in the titin-intact fibres compared to the titin-partially-degraded fibres (12.6±1.9% versus 6.7±1.0 %).

Force enhancement at a sarcomere length of 3.0 μm was not affected by the partial degradation of titin, thereby suggesting that titin's contribution to force enhancement at this sarcomere length is minimal. Because passive force in rabbit psoas fibres is small at short sarcomere lengths (SL< 3.0 μm) [4], we might suggest that titin is not essential for regulating force enhancement at relatively short SLs and thus its partial degradation does not affect force enhancement. On the other hand, titin partial degradation of 31.2% dramatically reduced force enhancement at a SL of 3.4 μm by 47% suggesting that titin plays a major role in force enhancement at long SLs.

Conclusions

Titin degradation by 31.2% reduced force enhancement by 47% at a SL of 3.4 μm and had no effect on force enhancement at a SL of 3.0 μm, suggesting that titin plays a major role in force enhancement at long sarcomere lengths.

References

[1] W. Herzog. Eur J Sp Sc. 2001.
[2] T.R. Leonard, W. Herzog. Am J Physiol Cell Physiol. 2010.
[3] H. Higuchi. J Biochem. 1992.
[4] V. Joumaa et al. Am J Physiol Cell Physiol. 2008.

Finite element bone strength at the distal radius and tibia predict vertebral yield load

Ryan Plett, Andres Kroker, Niloofar Ghazavi, Steven Boyd
Schulich School of Engineering, McCaig Institute for Bone and Joint Health, Department of Radiology, Cumming School of Medicine, University of Calgary

Introduction

Osteoporosis is a skeletal disease characterized by a loss in bone mass which results in increased bone fragility and risk of fracture[1]. Dual energy X-ray absorptiometry (DXA) is the most widely used clinical assessment tool for assessing osteoporosis[2], as it measures areal bone mineral density (aBMD) at the hip and spine[2]. It is known that bone strength is dependent on bone microarchitecture and not just aBMD[4]. However, the low spatial resolution and 2D imaging of DXA does not capture bone microarchitecture, only providing 60-70% of bone strength parameters including aBMD[2].

High-resolution peripheral computed tomography (HR-pQCT) can resolve bone microarchitecture in 3D *in vivo* at distal sites (distal radius and tibia)[3] and can be used to assess bone strength using finite element modeling (FEM). Central sites that are important osteoporotic fracture sites such as the spine are not accessible to this modality. Therefore, the purpose of this study is to determine if FEM-based bone strength estimates at distal sites are predictive of bone strength at the lumbar spine.

Methods

The left and right distal radius and tibia of 10 cadavers were imaged with HR-pQCT using standard *in vivo* settings[5]. FEM was performed to estimate bone strength based on failure load. The lumbar spines (L4) were imaged using a clinical DXA protocol to classify each cadaver in accordance with the clinical osteoporosis definition[1,2]. The L4 vertebrae (N=10) were cleaned, and mechanically tested on a Mini Bionix II testing device (MTS) via uniaxial compression (simulating vertical loading as in upright posture)[6]. The vertebrae were compressed to failure[7] at a rate of 0.5 mm/min allowing for quantitative analysis of the bone strength at this point[8]. The failure load (FL) and stiffness (K) was determined for each mechanically tested vertebra and compared to FEM-based estimates for the distal radius and tibia.

Results

aBMD measures correlated well with vertebral yield load (r=0.76). Most biomechanical parameters were significantly correlated between the distal sites and vertebra. Specifically, tibial FEM yield load correlated well with vertebral yield load (r=0.90). The yield load of the radius also correlated well with vertebral FL (r=0.70).

Conclusions

The strength of the correlations between the biomechanical parameters of the L4 vertebra and particularly the tibia suggests that the bone strength at central sites could be predicted from estimates of FEM-based bone strength at the distal skeletal site. Interestingly, both tibia and L4 are weight bearing bones, which may explain the strong relation. These data suggest that FEM-based bone strength estimates from HR-pQCT measurements at the distal tibia may contribute to improved bone strength prediction at the spine and the estimate of fracture risk over clinical aBMD measures.

References

[1] (Kanis, 1994) [2] (Adams, 2013). [3] (Frost, 2000). [4] (Nishiyama, 2013). [5] (Boyd, 2008). [6] (Feldman, 2007). [7] (Balabaud et. al., 2003) [8] (Mirzael et. al., 2009).

Figures

Figure 1: L4 Yield Load vs. Tibial Yield Load

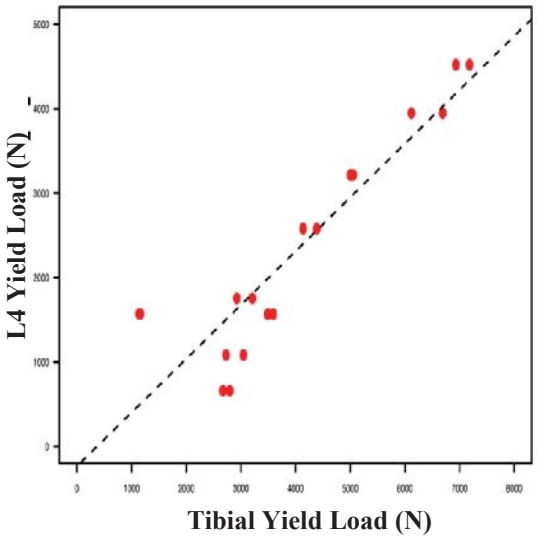

Hip Derived Synovial Mesenchymal Progenitor Cell Surface Markers *In Vivo* as Indicators for Differentiation Potential

Asmaa Affan, Nedaa Aljezani, Pam Railton, Jim Powell, Roman Krawetz
aaffan@ucalgary.ca

Introduction

Osteoarthritis (OA) is a chronic degenerative joint disease that is characterized by the degeneration of cartilage, inflammation, and pain[1]. There is currently no cure for OA, although there are ways to treat it, but most require quite invasive surgeries. Interestingly, there is a resident mesenchymal progenitor cell (MPC) population within the synovial membrane and the synovial fluid of the joint that have the ability to differentiate into bone, fat, and cartilage[2].

We hypothesize that *in vivo* and *in vitro* cell surface marker expression comparisons of the MPCs can potentially determine which population has the highest chondrogenic capacity and is best suited for clinical trails.

Methods

The synovial membrane and synovial fluid were digested in type IV collagenase for two hours in order to obtain a single cell suspension. The cells were subsequently stained with mesenchymal stem cell markers, including CD 90, CD 271, CD 44, CD73, and CD105, a macrophage marker, CD68, and a cell viability marker, FVS 510. The macrophages were excluded and the remaining cells were index sorted into 96-well plates. The cells were expanded, and underwent 21-day chondrogenic, adipogenic, and osteogenic differentiation. Differentiation was assayed using RT-qPCR and histological methods. Additionally, the cells were re-analyzed for marker expression after culturing.

Results

Hip synovial membrane from OA patient #15 data will be discussed. A single cell was isolated and was positive for the markers CD90, CD44, CD73, and negative for the markers CD68, CD271, CD105. Following differentiation, PCR analysis suggested that the cell line was able to differentiate into chondrocytes and adipocytes, but not osteoblasts. Histology data agreed with the PCR data with the adipocytes and chondrocytes having positive staining, whereas the osteoblasts were negative for the stain (Figure 1). FACS analysis following proliferation showed that they are positive for the markers CD90, CD44, CD73, and CD105, and negative for the markers CD68 and CD271. This comparison of the FACS data *in vivo* versus *in vitro* shows that the cells became CD105 positive after proliferation *in vitro*.

Conclusions

These tissue resident synovial MPCs may express cell surface markers that can give information as to which of the specific populations have the best cartilage regeneration abilities. By determining the properties of the synovial MPCs in osteoarthritic hips that allow for better chondrogenic differentiation abilities *in vitro*, selecting the optimal cells for regenerating cartilage can be done more efficiently and may ultimately use for a more efficient and less invasive treatment for osteoarthritis.

References

[1] Harris Q,*et al*. (2013) Monocyte chemotactic protein-1 inhibits chondrogenesis of synovial mesenchymal progenitor cells: An in vitro study. Stem Cells 31(10): 2253-65

[2] De Bari C, *et al*. (2001) Multipotent mesenchymal stem cells from adult human synovial membrane. Arthritis Rheum 44(8): 1928-42

Figures

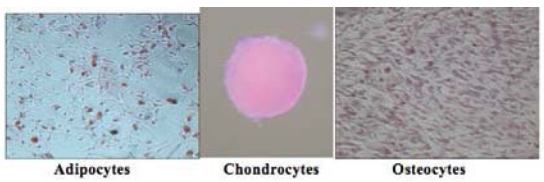

Figure 1. OA patient #15. Histological staining of the differentiated proliferating cells from a single cell into bone, cartilage, and fat. Magnification X20.

EFFECT OF PEG COATING ON NANOPARTICLE DIFFUSION THROUGH TUMOR EXTRACELLULAR MATRIX

Jacob Kennard[1], Wayne Ngo[1], Kaisha Terefe[1], Hagar I. Labouta[1], Trinh Nguyen[2], Christopher D. Sarsons[1], David Cramb[2], Kristina D. Rinker[1]
[1]Biomedical Engineering Program, University of Calgary
[2]Department of Chemistry, University of Calgary
jjkennar@ucalgary.ca

Introduction

Nanoparticle drug delivery systems have the potential to improve current cancer treatments through encapsulating cytotoxic agents and delivering them to specific sites in the body. One such class of particle, liposomes, has already found some commercial success [1]. Liposomes are vesicles composed of a lipid bi-layer surrounding an aqueous solution.

Poly(ethylene) glycol (PEG) surface coating is commonly used to improve the liposomes' stability in aqueous solutions. Furthermore, PEG limits the binding of blood antigens, which minimizes opsonisation and phagocytosis, extending circulation time in the blood stream. When applied to the surface of liposomes at lower molecular weights and surface densities, PEG adopts a "mushroom" conformation, in which adjacent chains of PEG do not interact laterally, therefore portions of the bi-layer remain exposed [2]. However, at higher molecular weights and surface densities, the "brush" conformation is adopted; where lateral interactions occur between neighboring PEG strands and provide complete coverage of the lipid bi-layer [2]. This study will investigate the effect of varying PEG molecular weight and surface density on liposome transport through tumour extracellular matrix.

Methods

Seven different formulations of liposomes were synthesized using a modification of the lipid extrusion method described in [1]. Molecular weight and surface density values were chosen to include both PEG conformations.

The Type I collagen hydrogel was prepared with a collagen concentration of 2.5mg/mL. Confocal Microscopy was used to track the liposome transport into the gels via the bilayer incorporated Rhodamine dye. While simple collagen hydrogels may not capture the complexity of tumour ECM, they allow for more carefully controlled conditions than *in vivo* models. Images were taken every 30 minutes until the 900 minute mark.

Results

As shown in Figure 1, the liposomes with a lower PEG loading (DOPC, 5, 10% PEG 1000, 5, 10% PEG 2000), all accumulated at the interface of the hydrogel, and had identical diffusion coefficients. The 5% and 10% PEG 5000 however, accumulated significantly less and therefore had a much greater diffusion coefficient.

Conclusions

The liposomes with low PEG surface density, and DOPC control liposomes shown in Figure 1, are all within the "mushroom" conformation of PEG [2] and therefore would all have exposed bilayer which is not shielded by the PEG strands. The formulations that penetrated deeply were notably only higher PEG surface densities (5 and 10% PEG 5000) which literature suggests would have been in the "brush" conformation [2]. This suggests that the high PEG surface densities sterically shielded the liposomes, and reduced the electrostatic interactions between the hydrogels and the liposomes, allowing increased diffusion.

References

1. Akbarzadeh A, et al. *Nanoscale Res Lett.* **8**:102, 2013.
2. Kenworthy A K, et al. *J Biophys.* **68**:1921-1936, 1995

Figures

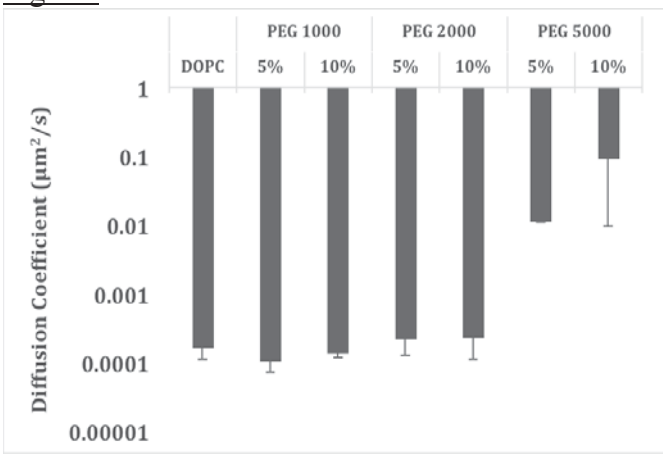

Developing 9.4T MRI to detect brain tumor treatment response with immuno-stimulating therapies

Runze Yang, Susobhan Sarkar, Daniel J. Korchinski, Ying Wu, V.Wee Yong, Jeff F. Dunn
Hotchkiss Brain Institute, Cumming School of Medicine, University of Calgary, Calgary AB, T2N-4N1

Introduction

Glioblastoma multiforme (GBM) is one of the most aggressive cancers. Despite surgery and chemoradiation, the prognosis is abysmal[1]. It is believed that the poor prognosis is due to a population of stem-like cells called brain tumor initiating cells (BTIC). These cells are responsible for chemoradiation resistance and tumor recurrence[1]. It has been shown that monocytes can be activated to suppress BTICs using Amphotericin B (Amp B)[1]. Monocytes are important in the Amp B mediated anti-tumor response. They can be labeled using ultra-small iron oxide nanoparticles (USPIO). We hypothesized that the efficacy of Amp B can be visualized by tracking monocytes using USPIO-MRI.

Methods

10,000 BTICs (line BT048) were implanted into the right striatum of severe combined immunodeficient mice (SCID). Treatment with Amp B (0.2mg/kg) or vehicle (sodium deoxycholate) were initiated 35 days after tumor implantation (n=5 vehicle; n=4 Amp B) and continued until the animals were sacrificed. MRI was performed 42-45 days post implantation. Initially, a multiecho gradient echo scan was acquired (TR = 1500ms, TE = 3.1, 7.1, 11.1, 15.1, 19.1 ms, voxel size =0.15 mm x 0.15 mm x 0.75 mm, Flip Angle = 30^{o}). A cannula was then placed into the tail vein, and Ferumoxytol (30mg/kg) was injected as a 100 uL bolus. The multiecho gradient echo was repeated 24 hours post Ferumoxytol injection.

Results

Changes in T2* was calculated from the pre-iron and the 24 hr post iron image. Animals in the vehicle group showed no significant changes in T2* ($p>0.05$), while the Amp B treated animals showed significantly decreased T2* compared to baseline ($p<0.01$) (Figure 1). The Amp B animals had a significant decline in T2* compared to vehicles ($p<0.05$).

Conclusions

There were no significant difference in tumor volume after 7 days of treatment; previous work with AmpB[1] had utilized a longer and earlier treatment regimen. We observed a significant decrease in T2* 24 hours after UPSIO injection in the tumor of the Amp B, but not vehicle animals. This is consistent with our hypothesis that monocytes are engulfing USPIO particles and then migrating to the site of the tumor. Using UPSIO-MRI, we were able to observe the pharmacological activities of Amp B after only 7 days of treatment. This is a promising method of monitoring immune-activating treatments.

References

1. Sarkar et al. Nat Neurosci. 2014. 17(1):46-55

Figures

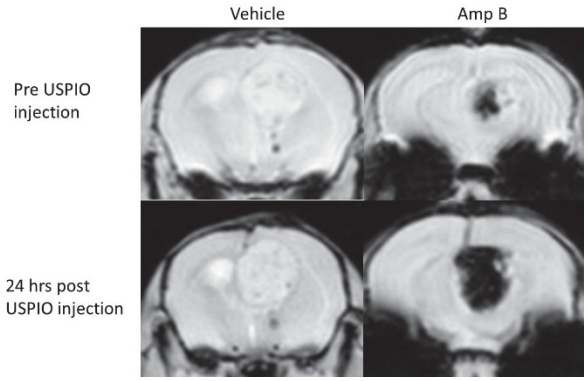

Figure 1: Change in T2* 24 hrs after USPIO injection. There was no obvious T2* darkening in vehicle animals (left column), but prominent darkening exclusively in the tumor can be seen in Amp B treated animals (right column).

Validating FE-derived internal bone strain using high resolution imaging and material testing

A. Sacher[1], D. Eichhorn[2], S.A. Kontulainen[2, 3], D. Cooper[4], S.K. Boyd[5], J.D. Johnston[1,2]
1. Department of Mechanical Engineering, University of Saskatchewan, Saskatoon, Canada
2. Division of Biomedical Engineering, University of Saskatchewan, Saskatoon, Canada
3. College of Kinesiology, University of Saskatchewan, Saskatoon, Canada
4. Department of Anatomy and Cell Biology, University of Saskatchewan, Saskatoon, Canada
5. Department of Radiology, University of Calgary, Calgary, Canada

Introduction

Degenerative bone diseases such as osteoarthritis are a growing problem in North America. Osteoarthritis (OA) is marked by morphological and mechanical alterations to bone which are thought to change overall mechanical behaviour, resulting in distorted joint mechanics and accelerated cartilage degeneration [1]. Trabecular bone, in particular, is believed to play an important role mediating overall mechanical behaviour, pain initiation and potentially OA development [2, 1].

Subject-specific finite element modelling (FEM) has potential to improve our understanding of OA pathogenesis [3]. With FEM, models of human bones and joints are created from computed tomography (CT) images and evaluated computationally to assess mechanical properties such as internal strain distributions. However, there are discrepancies in the literature on the methods of assigning material properties to the bone being modeled. Specifically, it is unclear what density-modulus equation(s) should be used for converting CT imaged bone mineral density (BMD) to elastic modulus (E) (i.e., E-BMD equation) [4]. This is a crucial aspect of FEM as inaccuracies in the material properties will alter the final output.

To address this issue, the objective of this work was to develop an experimental testing system for assessing the *in situ* mechanical behavior of cortical and trabecular bone, which would be used to validate FEM assessments of bone strain and displacement.

Methods

Overview: A testing system was created with the purpose of delivering step compressive loads to a specimen while simultaneously imaged using high resolution imaging.

Mechanical Testing: The testing system was composed of a radiolucent end-piece for holding the specimen during imaging and loading. The testing system can support a 10 kN load for a sample 10cm in diameter.

High Resolution Imaging: A high resolution peripheral quantitative computed tomography (HR-pQCT) scanner (Xtreme CT) was used to acquire multiple high resolution 3D images of the specimen with multiple loading conditions (unloaded, increasing step-loads). Imaging was performed when the load normalized (i.e., stress was relaxed).

Image Processing: Digital Volume Correlation (DVC) (Matlab) was used to track the displacement of individual 3D voxels in deformed loaded images [5]. Preliminary efficacy of DVC was evaluated via simulations with artificially deformed images of known strain.

Preliminary Results

DVC software was able to determine internal strains of the mechanically loaded synthetic bone specimens. The next step is to perform tests with synthetic and cadaveric tissues in the mechanical testing system. These tests will allow direct comparison between DVC acquired displacement and strain with FE-derived displacement and strain.

Anticipated Conclusions

Outlined methods will provide insights into the mechanical behaviour of bone, particularly trabecular bone. These insights will be used to validate existing FE models. This research has important implications for understanding bone mechanics, musculoskeletal disease as well as improving arthroplasty design.

References

[1] Amini et al., Med Eng Phys, 2015
[2] Burnett et al., Osteoarthritis Cartilage, 2015
[3] Poelert et al., Proceedings of the Institution of Mechanical Engineers, Part H: Journal of Engineering in Medicine, 2012
[4] Nazemi et al., Clinical Biomechanics, 2015
[5] Bar-Kochba et al., Experimental Mechanics, 2014

Non-invasive characterization of degradation profile of 3D-printed hybrid constructs for cartilage tissue engineering using synchrotron-radiation-inline-phase-contrast CT

Adeola D. Olubamiji[1], Zohreh Izadifar[1], Ning Zhu[3], Frank B. Eames[2] and Daniel X.B. Chen[1]

[1] Department of Biomedical Engineering, University of Saskatchewan, Saskatoon, SK S7N 5A9, Canada

[2] Department of Anatomy and Cell Biology, University of Saskatchewan, Saskatoon, SK S7N 5E5, Canada

[3] Canadian Light Source Inc., University of Saskatchewan, Saskatoon, SK S7N 2V3, Canada

Introduction

Three-dimensional (3D)-printed hybrid constructs fabricated from polycaprolactone (PCL), alginate hydrogel and living cells have shown great potential for cartilage tissue engineering (CTE) applications [1]. However, the biomaterials used to fabricate these constructs have properties such as low X-rays attenuation, low density, high water content and different degradation profile [2]. Thus, it is often difficult to characterize architecture, degradation profile and functionality of the different components of the hybrid constructs using conventional imaging techniques. This raise a big challenge especially for non-invasive assessments of the functionality of these hybrid constructs. Synchrotron-radiation-based inline phase contrast imaging (inline-PCI) offers great potential for non-invasive characterization and 3D visualization of details of weakly absorbing biomaterials such as those present in our hybrid constructs [2].

Methods

In this study, hybrid constructs for cartilage tissue engineering were fabricated from PCL, alginate and cells. Inline-PCI combined with computed tomography (CT) was optimized by investigating three sample-to-detector-distances (0.25m, 1m and 3m) for characterization of the 3D-printed hybrid constructs. Then, the most suitable sample-to-detector-distance (SDD) was utilized to visualize and characterize the architecture of the multi-density constructs and structural changes associated with degradation of the different components of the hybrid constructs at different time points *in vitro* and *in vivo.*

Results

The results showed that the edge enhancement property of inline-PCI-CT becomes more prominent at the longest SDD and this consequently caused better visualization of the different components of the hybrid constructs. In addition, inline-PCI-CT enabled visibility of the minute variations and fine details due to evidence of degradation of the components of the hybrid constructs as the time point increased both *in vitro* and *in vivo*.

Conclusions

Based on these findings, synchrotron-radiation-based inline-PCI-CT technique showed potentials for longitudinal monitoring of degradation profile of constructs over long period of time. In addition, due to its ability to delineate minute details of different low X-rays attenuation biomaterials in soft tissues, this technique is promising for longitudinal visualization of cartilage tissue growth associated with the hybrid constructs over different time points *in vivo*.

References

1) Schuurman W, Khristov V, Pot MW, van Weeren PR, Dhert WJ, Malda J. 2011. "Bioprinting of hybrid tissue constructs with tailorable mechanical properties." Biofabrication 3 (2): 021001-021008.

2) Zhu N., A. Rajaram A., Olubamiji A., D.J. Schreyer D.J.,Wysokinski T.W. ,Belev G., Chen X.B. 2015. "Optimization of in-line phase contrast imaging setup for in vivo visualization of hydrogel scaffolds in nerve tissue engineering applications." 4th TERMIS 2015 World Congress . Boston.

Changes in the relative velocity of joint following anterior cruciate ligament transection leading to osteoarthritis in a sheep model

S. M. M. Shekarforoush, D. A. Hart, N. G. Shrive
McCaig Institute for Bone and Joint Health, Cumming School of Medicine, University of Calgary

Introduction

Post Traumatic OsteoArthritis (PTOA) can develop after injury to a joint. It is widely accepted that alterations to joint biomechanics following injury are one of the main causes of subsequent cartilage damage, and the development of OA. Recently, it has been suggested that changes in joint relative surface velocity correlate more consistently with cartilage damage after joint injury than other measures of joint motion [1-2]. The details of the correlation between any change in relative surface velocity and the development of PTOA have not been clarified but this idea can be explained by the fact that the surface shear stress is related to the direction of relative motion of the surfaces, and that a change in the direction of the relative surface velocity could therefore disrupt the cartilage surface. An objective of this study was to determine the relative surface velocity (both magnitude and direction) of the tibio-femoral compartments of the knee joint before and after ACL transection. We hypothesize that ACL transection in sheep causes small but significantly abnormal variation in tibio-femoral relative surface velocity leading to damage of the cartilage surfaces.

Methods

Five skeletally mature female Suffolk-cross sheep were trained to walk on a standard treadmill. The highly accurate Instrumented Spatial Linkage (ISL) was used to measure the complete six degrees of freedom motion of the joint. Stifle joint kinematics were measured before injury and 20 and 40 weeks after the ACL was transected through arthroscopic surgery. Software was developed to calculate the relative velocity of the joint surfaces by defining an appropriate joint coordinate system.

Results

The results showed that at the stance phase of the gait (around the first 60% of the gait cycle), the components of the angular velocity of the joint were low about all directions, as expected. In the swing phase of the gait cycle, the joint has sinusoidal motion in all directions, which is compatible with the pattern of gait (i.e. flexion-extension, abduction-adduction and external-internal rotation). The magnitude of angular velocity about the abduction-adduction axis is much lower than the magnitude of angular velocities about other directions. Also, the magnitude of angular velocities were decreased for all directions of the joints 20 and 40 weeks after ACL-transection and there were little phase changes between the intact time point and 20 and 40 weeks after injuries.

Conclusions

The mechanism by which cartilage degenerates after ligament injuries has not been established. Using the results of this research, we can examine a new mechanical mechanism for PTOA progression. Since the direction of the shear forces between cartilages defined by the relative surface velocity of the joint, changes in the relative surface velocity can consequently lead to cartilage damage and development of PTOA. Our preliminary results have supported this idea that the joint relative surface velocity -and consequently shear forces- changes after ACL injury. Further studies need to be carried out in order to define the distribution of the relative velocity of the joint surfaces and to find any correlation between the surface velocity changes and the sites of cartilage damage.

References

[1] Jillian E. Beveridge, et al., J Orthop Res. 31(11):1745-56, 2013.
[2] William J. Anderst, et al., Inc. J Orthop Res. 27:71–77, 2009.

Cell Impedance Alteration: Promising Biomarker for Monitoring Neuronal Differentiation

Mohsen Janmaleki[1], Sara Abasi[2], Mohammad Abdolahad[3], Reza Shahghadami[2], Amir Sanati-Nezhad[*1]
[1] BioMEMS and Bioinspired Microfluidic Laboratory, Department of Mechanical and Manufacturing Engineering, University of Calgary, [2] Department of Medical Physics and Biomedical Engineering, Shahid Beheshti University of Medical Sciences, Tehran, Iran, [3]Nano Electronic Center of Excellence, School of Electrical and Computer Engineering, University of Tehran, Iran

Introduction

Developing a non-invasive, label-free, real-time, and inexpensive technique for monitoring differentiation process is a demanding in tissue engineering. It has been demonstrated that cell impedance alters during several cell behaviors. Interestingly, neurons have unique electrical properties, vital for signal transmission; which can be a convincing feature for evaluating the quality of neuronal differentiation. In this study, a special gold interdigitated electrode (IDE) was designed to measure impedance alterations of rat bone marrow mesenchymal stem cells (rBMSCs) induced to be differentiated into neurons.

Methods

The IDEs were developed through patterning of gold on glass substrate by UV-photolithography technique. Each IDE consisted of 40 paired fingers or digits with width and length of 40 µm and 7 mm, respectively. The spacing between digits was 60 µm. To measure electrical properties of the cells, a 20 mVp-p sinusoidal waveform (10 Hz to 200 KHz) was applied to the IDE, meanwhile the voltage drop over and current passing through the IDE were recorded by a data acquisition device controlled by self-developed software in LabVIEW. The rBMSCs isolated from 6-8 week-old rat were cultured in basic medium (αMEM medium supplemented with 20% FBS and 1% Pen/Strep). At passage 5 and before neuronal induction, the cells were transferred to a test chamber coated with gelatin to grow overnight (**Fig. 1**). A fresh basic medium added with 10 ng/ml basic fibroblast growth factor (bFGF) was provided to cells 24 h before neuronal induction. Then, neural induction medium (basic medium plus bFGF, butylated hydroxyanisole, Forskolin, KCL, Valproic acid, and human regular insulin [1]) was introduced to initiate differentiation. To verify correlation between obtained results and genes expressions, quantitative amount of neural markers including microtubule-associated protein2 (MAP2), glial cell line derived neurotrophic factor (GDNF), ciliary neurotrophic factor (CNTF), brain-derived neurotrophic factor (BDNF), and developmental pluripotency associated 5A (Dppa5a) comparing with a housekeeping gene were quantified by Real-time PCR.

Results

Impedance analysis revealed a significant difference between the impedance of rBMSCs and differentiated neuronal cells. **Fig. 2** shows the behavior at 6 h. From **Fig. 3**, the expressions of neural genes were at the maximum level, while pluripotency related gene (Dppa5a) had a decreasing tend.

Conclusions

Alterations of Cells impedance were monitored during neural differentiation. Differentiated cells mainly presented lower impedance in comparison with stem cells. Real-time PCR showed strong association between electrical properties and neural gene expressions. To sum up, the results are convincing to consider the proposed technique as a proper biomarker for evaluation of neuronal tissue engineering.

References

[1] D. Woodbury et al. Adult rat and human bone marrow stromal cells differentiate into neurons. J Neurosci Res 2000, 364–70

Figures

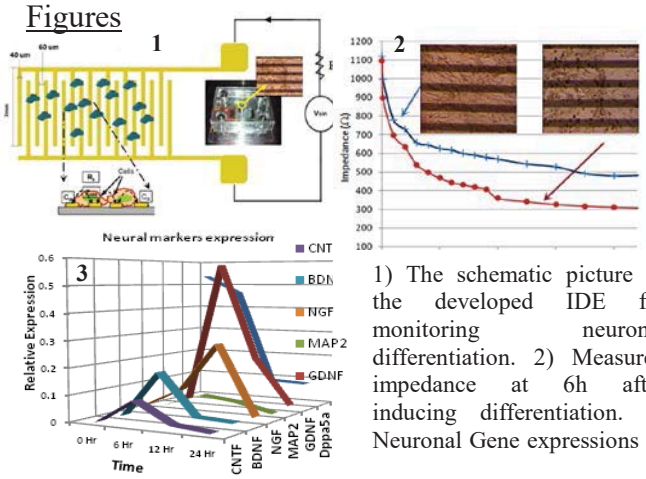

1) The schematic picture of the developed IDE for monitoring neuronal differentiation. 2) Measured impedance at 6h after inducing differentiation. 3) Neuronal Gene expressions of

Multicomponent T2 Analysis of Glioblastoma in a Mouse Model

Pandey, S.[1,2,3], Ali, T.[1,2,3], Sarkar, S.[1,2,3], Yong, V.W.[1,2,3], and Dunn, J.F.[1,2,3]
[1]Hotchkiss Brain Institute, [2]Faculty of Medicine, [3]University of Calgary

Introduction

Soft tissue contrast in Magnetic Resonance Imaging (MRI) is obtained from the distribution of hydrogen protons from water-filled biological tissues. T2, the spin-spin relaxation time, is affected by the water environment and will increase with edema and specific changes in cell type. Hence, unique T2 times reveal distinctive tissue characteristics [1].

To date, T2 analysis of tumors has largely used monoexponential fitting. However, this method is not sensitive to the multicomponent nature of tissues within a voxel. Therefore, multiexponential T2 analysis can allow for superior differentiation between tissues within the mouse gliobastoma [1,2]. We will use novel visualization software to determine how the multicomponent T2 can improve our sensitivity to specific tumor microenvironments. A study showing proof of principle was published using SCID mice implanted with patient-derived brain tumor initiating cells (BTICs) [1]. This study will use human derived glioblastoma cells in mice models to examine whether T2 can be used to detect treatment response.

Methods

Anesthetized NOD-SCID mice (with invasive gliomas and controls) were imaged on a 9.4 Tesla scanner using a modified Carr-Purcell-Meiboom-Gill sequence. An in house software program was used to analyze and visualize the multiecho T2 decay from axial brain slices [1]. Multicomponent T2 will be visualized to show regional heterogeneity and quantified within specific regions.

Results

Distinguishing between tissues is possible from T2 properties of mouse brain tissues in the scanned slices. Quantitative T2 analysis shows subtle differences from the T2 ranges of interest; these ranges are usually undetermined using the traditional ROI based approach [1]. Using the histology of brain tumors, the relationship between voxel-based T2 values and water microcompartment alterations is studied.

Conclusions

Changes in the tissue environment result in an increase in free water, which in turn increases the T2 relaxation time. Previously, T2 relaxation time distribution maps have been created to differentiate between glioblastoma and metastatic brain tumors in patients [3]. By producing a quantitative T2 map in adjunction to the multiexponential T2 analysis conducted, one can show the varying T2 distributions in the same mouse gliobastoma. This will allow for a clearer distinction of tumor margins and may provide a sensitive metric of treatment response.

References

[1] Ali T., Bjarnason T., Senger D., Dunn J., Joseph J., Magliocco A., Mitchell J., Assessment of Mouse Glioblastoma with Improved Voxel-Based Quantitative T2 MRI. 2015; 2:1-13
[2] Tolxdorff T., Handels H., Bohndorf K., Advantages of Multiexponential T2 Analysis. 1990; 1:75-80
[3] Nakai K., Nawashiro H., Shima K., Kaji T., An Analysis of T2 Mapping on Brain Tumors. 2013; 118:195-199

Figures

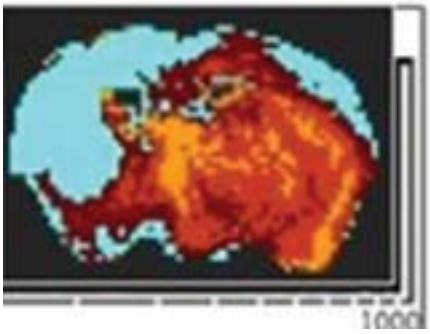

Figure 1. Visualization of a multiexponential decay in a mouse brain tumor. T2s in the range of 30.4 ms to 149.2 ms are shown above, however any T2 range can be displayed to help with differentiating tissue heterogeneity [1]. (Adapted from Reference [1]).

Surface modified screen printed graphene biosensor for electrochemically diagnosing and manage Spinal Cord Injury (SCI)

Sultan Khetani, Amir Sanati Nezhad
2500 University Dr. N.W., EEEL 455B, Calgary, AB T2N 1N4, Canada

Introduction

Approximately 500,000 people suffer spinal cord injury every year and people surviving spinal cord injury are around 130,000.[1] It is also a massive drag on the Canada's economy costing nearly $3 billion a year[2]. We report a novel screen printed graphene biosensor for the diagnosis and management of Spinal cord injury (SCI).

Methods

Electrode geometry was engraved out from Maskease® sheet using a Versa CO_2 Laser cutter to fabricate electrodes on the ceramic surface. Electrodes of the microchip were fabricated using silver and graphene (20% w/w) and incubated on a hot plate at 80ºC. (Fig. 1). GFAP was selected as SCI indicators. Electrografting(Fig.1) of the sensor's surface was performed by pipetting 50µl of 10mM 4- nitrophenyl Diazonium (4-NPDS) solution in PBS and performing chronoampeometry (CA) followed by washing cycle using DI water. 100µl of 0.1M KCl was pipetted on the sensor's surface and Cyclic Voltammetry (CV) was performed to generate nitrophenyl film on it. Electrode surface was washed using PBS and incubated for 60mins in 2.5% Gluteraldehye (GA) in PBS (200mM pH7.0). After 60mins, 50µl GFAP antibody (1% v/v) in PBS was pipetted on it and incubated for 30mins. Electrode was washed with PBS and 100µl of blocking agent (0.25% of BSA in PBS buffer pH7.0) was pipetted and electrode was incubated for another 30mins. Electrochemical analysis was performed using 100µl of 5mM $K_3Fe[Cn]_6$ redox pair under Differential Pulse Voltammetry (DPV).

Results:

We observed reduction peak at 85mV and average peak ferrocyanide current of the five CV scans was observed at 17.05 ± 1.54 (Std. dev) µAmp for the negative control (Fig. 2). The peak current validates characterization curves (not shown) and confirms Electrografting of the electrode.

Conclusions:

We have developed an alternate method to diagnose and manage spinal cord injury using electrochemical sensing of the injury marker that can be used along with imaging techniques. The aim of this research is to propose an alternate technique for the diagnosis and management of SCI injury. Preliminary characterization data have revealed promising result which validates the need of continuing this research to ultimately propose an alternate tool that is equally effective to the conventional imaging method and inexpensive so that it decreases the burden of public finance. Our next effort will be on the antibody (Ab) alignment, to evaluate if their orientation effects on the sensor and use SCI marker.

References:

1. International Perspective on Spinal Cord Injury,http://apps.who.int/iris/bitstream/10665/94190/1/9789241564663_eng.pdf, 2013

2. Gwynedd E., Pickett, Mauricio Campos- Benitez., Jana L. Keller., and Neil Duggal., "Epidemiology of Traumatic Spinal Cord Injury in Canada" Spine; 31(7):799-805.

Figures

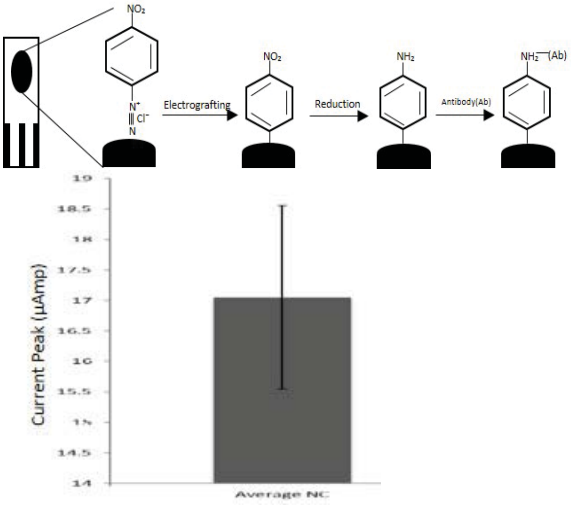

Development and Validation of New CAD/CAM System for Spinal Orthosis

Kirsten Svidal, Doug Hill, Edmond Lou
10105 112 Avenue, Edmonton, AB T5G 0H1

Introduction

Scoliosis is a three-dimensional lateral curvature of the spine which affects 2-3% of adolescents. The most common non-surgical treatment is to use spinal orthosis to stop curve progression. To build a spinal orthosis, the body shape of the patient needs to be captured. Manual method or a computer aided design/computer aided manufacturing (CAD/CAM) system has been used to build spinal orthosis for patients. Although the CAD/CAM method is preferable[1], the initial cost (US$150K) and the annual maintenance cost (US$30K/year) are high. The objectives of this study were to develop a low-cost stationary CAD/CAM system and to validate the accuracy of the developed system.

Methods

Four Microsoft Kinects and a custom built wooden frame were used and configured (Figure 1) to capture the body shape. Subjects standing inside the frame are scanned by the Kinects within 20 seconds. Scanning time is critical because subjects' motion may cause data alignment errors. Prior to scanning a subject, the system must be calibrated to obtain the appropriate transform, so the data can be properly integrated and the resulting reconstruction is the correct size. Algorithms to instantly capture and reconstruct the body shape were developed in C#, utilizing the Microsoft Kinect Fusion framework.

To validate the system, a spinal torso foam model was scanned by the system. Four sets of the Kinect data were acquired and the 3D reconstruction was automatically obtained. To validate the accuracy, small dot stickers were selectively placed on the foam model as landmarks, so measurements could be taken on the foam model and the reconstructed computer model.

Results

Figure 2 shows the foam model compared to the reconstructed model. The measurement differences between the foam model and the reconstructed model for cross-sectional measurements between A and B, and C and D were 1.0cm and 3 mm, respectively. Although the overall measurement error exceeded ±5mm, key factors that influenced the accuracy were camera positioning and software tuning to merge data. Optimization could be done after my research work is completed.

Conclusions

This preliminary result showed the developed low cost Kinect system was able to capture a body image and the system accuracy might be optimized after more research has been done.

References

[1] Sankar WN et al.: Scoliosis in-brace curve correction and patient preference of CAD/CAM versus plaster molded TLSOs, J Child Orthop 1:345-349, 2007

Figures

Figure 1: Kinect System set-up with model torso.

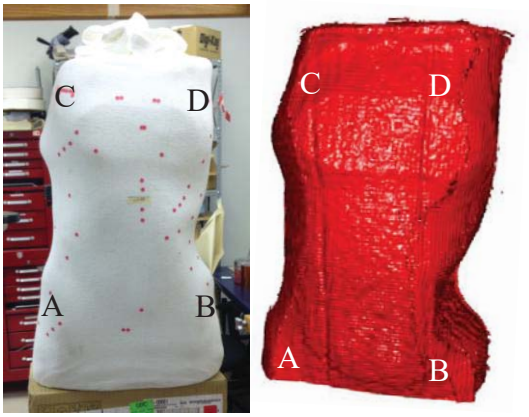

Figure 2: Foam model and reconstructed model

Evaluation mechanical properties of the bioabsorbable polymers as a material in designing flow-diverter stent

Mehdi Jamshidi, Soheil Sadeghi, Uttandaraman Sundararaj, Alim Mitha
University of Calgary

Introduction

Bioabsorbable stents have received recent attention because they mitigate the need for lifelong anti-thrombotic drugs and reduce the risk of late stent thrombosis and restenosis [1-2].

The most important mechanical traits of the candidate material for designing a stent are appropriate levels of Young modulus (E), yield stress (σ_y) and elastic strain (ε_e) to imply enough radial force and to resist plastic deformation in a process of crimping [3-5].

In this study, mechanical properties of the different types of bioabsorbable fibers were evaluated for flow-diverter stent for treatment of intracranial aneurysm. Blends of biocompatible polymers may have advantages over pure polymers.

Methods

Three grades of Poly-L-lactic acid (PLLA: 10, 32, 38) with different molecular weights (MW) and one grade of Polycaprolactone (PCL) were obtained from Corbion Purac and Sigma-Aldrich, respectively. Blends of PLLA 32-PCL were prepared by solution mixing in chloroform ($CHCl_3$) at 50 °C with different composition ratios (A1: 95/5, A2: 90/10, A3: 85/15, A4: 80/20, A5: 75/25 and A6: 70/30). Samples were left under the hood for 12 hr and then dried in an oven for 48 hrs at 50 °C.

Polymer fibers were produced using a Kayeness Capillary Rheometer with the manufacturing process conditions of 220 °C, 0.2 in/min ram speed, and 1:4 draw ratio. PLLA 32 fiber was produced by a 1:8 draw ratio to evaluate the effect of draw ratio in the fiber structure. Five samples with length of 30 mm were randomly selected over the whole length of each polymer fiber. Mechanical properties of fibers were tested by a Bose tensile test machine with a 5 mm/min speed rate.

Differential scanning calorimetry (DSC) experiments were done isothermally at 120°C. Samples with an average weight of 10±1mg were heated up to 220°C to erase the thermal history and then quenched to the test temperature.

Results

Although PLLA 38 has the highest MW compared to other polymers in this study, results indicate that PLLA 32 has a higher E and σ_y than other polymers. This maybe because of the difference in molecular architecture of the PLLA 38 which has a linear structure while PLLA 32 has some content of long chain branching.

Doubling of draw ratio in producing fiber of PLLA 32 results in higher E and σ_y. Based on non-isothermal first heating DSC traces, PLLA 32 fibers has negligible degree of crystallinity due to its relatively long half-time of crystallization. Furthermore, it illustrates that by increasing the content of PCL in the matrix of PLLA, crystalline content will dramatically decrease. It can also be seen that by increasing the content of PCL in the matrix of PLLA σ_y and E decreases notably and ε_e extends slightly.

Conclusions

MW, draw ratio and molecular architecture are important factors in designing a stent. Moreover, in this study, no significant improvement was observed in mechanical properties of PLLA by blending with PCL without compatibilization.

References

1. Ron Waksman, Catheterization and Cardiovascular Interventions, 2007, 70: 407–414.
2. Kuizhong Wang et al., Neuroradiology, 2013, 55: 621-628.
3. Jianting Dong et al., Polymer Engineering and Science, 2013, 54: 1418-1426.
4. A. García et al., Journal of the Mechanical Behavior of Biomedical Materials, 2012, 10:166-175.
5. Yaru Han et al., macromolecular materials and engineering, 2012, 297: 128–135.

An Investigation into the Feasibility of using Microwave Imaging to Monitor Bone Health

Bryce A. Besler, David Garrett, Steven K. Boyd, Elise C. Fear
babesler@ucalgary.ca

Introduction

Assessing bone health is of particular interest in age-associated disease such as osteoporosis. Having tools that can safely and accurately assess bone health allows for the screening, diagnosis, and monitoring of disease or injury. High-resolution peripheral quantitative computed tomography (HR-pQCT) is a developed tool capable of direct three-dimensional (3D) visualization of bone. Recent evidence suggests microwave imaging can be a complementary medical imaging tool to HR-pQCT for dynamic assessment of full bone health [1] showing that microwave properties are sensitive to physical changes in bone. However, the study was purely exploratory and provided no direct evidence or mechanism.

In this study, we aim to understand the interaction of electromagnetic waves with bone as a composite material, specifically the material anisotropy. Such information would be crucial to understanding how microwave measurements relate to the physical characteristics of the bone.

Methods

Image data for the right and left tibia and radius of one female and two male subjects was acquired from HR-pQCT (XtremeCTII, Scanco Medical). The 3D image data was smoothed with a Gaussian filter ($\sigma = 1.6$) and segmented using histogram-based segmentation. Cubes (edge length 82 voxels, 5.002 mm) were extracted from the segmented images. The extracted cubes were imported into electromagnetic simulation software (SEMCAD X, Schmid & Partner Engineering AG). A parallel plate waveguide filled with air was excited with a Gaussian pulse polarized in the z-axis (f_0 = 6.5 GHz, BW = 11 GHz) and material properties were assigned from literature [2]. Three simulations were performed per image such that the electromagnetic wave was polarized in each of the three anatomical directions: anterior-posterior, medial-lateral, and proximal-distal.

Results

Effective permittivity, ε'_r, was calculated for each of the anatomical directions and plotted across the frequency range of the input signal. A representative plot for all images is shown in Figure 1. The effective permittivity for each orientation tends to vary around a common permittivity.

Conclusions

The results presented here provide a rudimentary but novel insight into the anisotropic behavior of bone at microwave frequencies. Furthermore, it presents a technique for 3D model acquisition and simulation of bone not yet present in literature. This technique will allow further exploration of the electromagnetic properties of bone such as the development of models for the effective medium of bone as a composite material. With such information, the microwave measurements of bone could be directly related to the bone's physical properties. This would prove the potential of microwaves to assess bone health and allow the development of *in vivo* imaging tools for assessing disease and trauma.

References

1. Meaney et al. *IEEE Trans. Biomed. Eng.* **59**:3304-13, 2012.
2. Peyman et al. *Dielectric Properties of Tissues at Microwave Frequencies.* 2005.

Figures

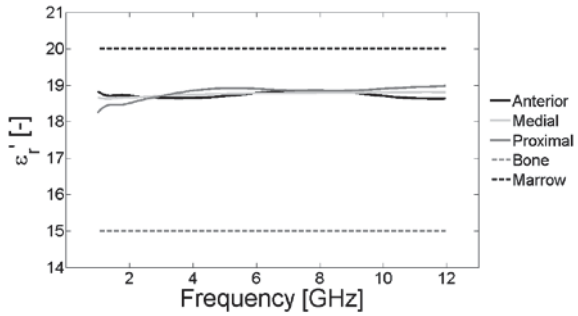

Figure 1: The assigned relative permittivity (dashed lines) to the bone and marrow and the effective permittivity (solid lines) in each anatomical direction (bone volume fraction of 25.6%).

Damage Model for Biological Tissues

Amir Hamedzadeh and Salvatore Federico
Department of Mechanical and Manufacturing Engineering, University of Calgary

Introduction

From the engineering point of view, a biological tissue is an extracellular matrix that embeds the cells, is composed of several types of macromolecules, is reinforced by collagen fibres, and is permeated by water. The failure and damage mechanisms of soft biological tissues strongly depend on the tissue's microstructure, but the irreversible phenomena related to the failure of soft tissue have not been fully understood.

The purpose of this work is to establish a model of damage of the collagen fibres embedded in a biological tissue, as these are the main load-bearing structural elements.

Methods

We assume that: *a*) the non-collagenous matrix and the collagen fibres are both non-linearly elastic; *b*) each fibre is a one-dimensional element bearing only tension along its axis; *c*) each fibre is comprised of bundle of fibrils that are connected by means of proteoglycan (PG) cross-bridges. These bridges transmit the load between fibrils, forming an integrated structure, which can elongate significantly. The fibrils are crimped in the) configuration and each of them is recruited at different stretch denoted λ_s. All fibrils fail at the same stretch λ_f calculated with respect to its straightened configuration, so that, with respect to the reference configuration, the failure stretch of each fibril is λ_f λ_s. In order to describe progressive recruitment and failure in a fibre, we use a triangular distribution function [1], and derive an expression for both recruitment and damage processes (Figure 1). To find the nominal stress in the fibre, we adopt a linear constitutive relation for each fibril between the nominal stress and the logarithmic strain. Using this constitutive relation, we can find the stress in the fibre by integration over the distribution functions. For the unloading part, we neglect the portion of fibrils that have already failed and integrate over the remaining portion of the probability distribution functions.

Results

Figure 2 shows a typical stress-stretch curve for a single fibre, as well as the unloading profiles for different unloading stretches (λ_u). The overall behaviour of the stress-stretch curve is consistent with that observed in the absence of damage soft biological tissues [2].

Conclusions

We proposed a one-dimensional constitutive model for a single fibre using triangular probability distribution functions in order to account for the progressive recruitment and damage of individual fibrils. The model is able to predict the behaviour of the fibre in both loading and unloading. We plan to extend the model to three dimensions by accounting for the statistical orientation of the collagen fibres [3].

References

1. Martufi G, Gasser, TC, 2011, J Biomech, 44, 2544-2550
2. Fratzl P, 2008, Collagen: structure and mechanics. Springer Science & Business Media.
3. Federico S, Grillo A, 2012, Mech Mat 44, 58-71

Figures

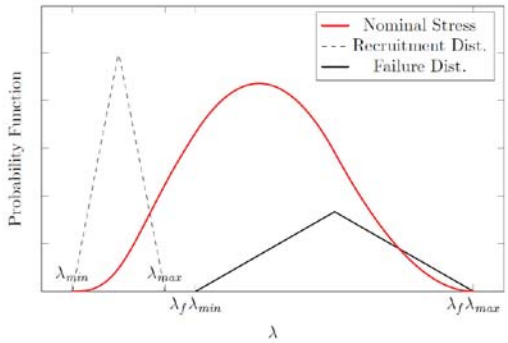

Figure 1 Probability for recruitment and failure

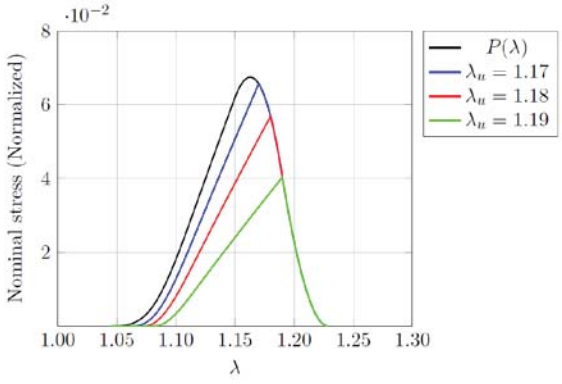

Figure 2 Stress-stretch curve for a single fibre

Increased cerebral metabolic rate for oxygen in a mouse model of multiple sclerosis

Thomas W. Johnson[1,2], Linhui Yu[2], Kartikeya Murari[2], Jeff F. Dunn[1]
1: Faculty of Medicine 2: Schulich School of Engineering, University of Calgary, Alberta

Introduction

Multiple sclerosis (MS) has been traditionally thought of as a white matter (WM) disease, but damage grey matter (GM) correlates better with physical and cognitive deficits in later stages of the disease and holds promise as a complementary explanation. GM changes can be accompanied by metabolic changes in the tissue due to the increased energetic demands damaged tissue can create, and can be quantified with cerebral metabolic rate for oxygen ($CMRO_2$); it is a direct measure of aerobic metabolism occurring in the brain. Previous methods of measuring $CMRO_2$ are extremely expensive as they require short-lived radioisotopes. To counter this, we constructed a multimodal broadband near-infrared spectroscopy (NIRS) / magnetic resonance imaging (MRI) system that allows for inexpensive and rapid $CMRO_2$ measurement in mice. We then used the system to measure GM $CMRO_2$ in mice with the experimental autoimmune encephalomyelitis (EAE) model of MS.

Methods

C57BL/6 mice were used in this study. 8 control and 3 long-term EAE mice were imaged, with EAE mice at 35 days post-induction. $CMRO_2$ was obtained by combining cerebral blood flow (CBF) with arterial and capillary blood oxygen saturation. CBF was obtained with arterial spin labelling (ASL) MRI on a 9.4T Bruker MR system; matrix = 128 x 128, TE=2.66ms, TR=3000ms, FOV=3cm. Blood oxygenation NIRS data were found by transmitting broadband NIR light into the cortex and collecting returning light with another fibre, which is then analyzed via a CCD spectrometer and MATLAB software using the second differential method.[1] Measurement regions of interest (ROIs) were determined using a photon transport modelling software package, NIRFAST,[2] which calculated the brain area of optimal sensitivity for the NIRS system.

Results

Control group $CMRO_2$ was found to be 2.69 ± 0.84 µmol O_2/g/min and 6.09 ± 1.14 µmol O_2/g/min for EAE mice. A two sample t-test was performed, and EAE $CMRO_2$ was significantly increased ($p<0.001$). Control values are also in agreement with previously reported literature $CMRO_2$ values.[3]

Conclusions

We have successfully constructed a multimodal NIRS/MRI system to measure $CMRO_2$ in mice. To our knowledge, this is the first time such a system has been applied to mice. In addition, increased $CMRO_2$ was found in long-term EAE mouse GM, supporting the hypothesis that there is metabolic component to MS, particularly in GM damage and degeneration.

References

1. Matcher, S. J. & Cooper, C. E. *Phys. Med. Biol.* 39, 1295 (1999). **2.** Dehghani, H. *et al. Commun Numer Methods Eng* 25, 711–732 (2008). **3.** Cui, W. *et al. J. Cereb. Blood Flow Metab.* 33, 1846–1849 (2013).

Figures

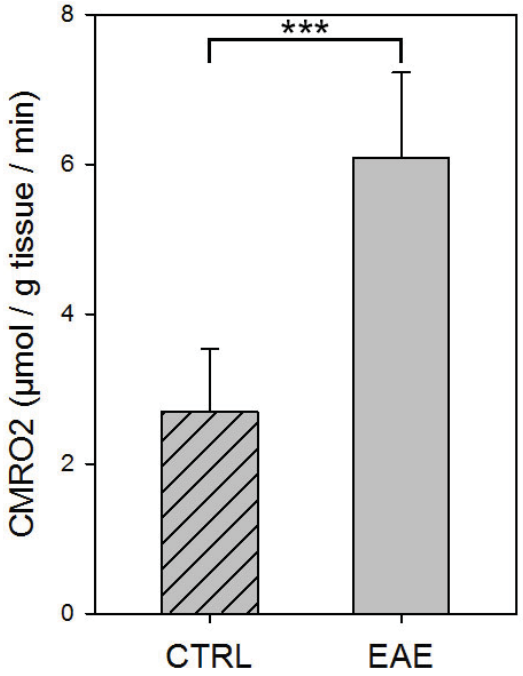

Figure 1: Increased CMRO2 found in long term EAE mice. *CMRO2 for the control group (n=8) was found to be 2.69 ± 0.84 µmol O2/g/min; CMRO2 for the EAE mice (n=3) was found to be 6.09 ± 1.14 µmol O2/g/min, (p < 0.001, mean ± S.D).*

Developing a Model to Predict Distal Radius Fracture During a Fall

Matthew P. M[c]Donald[1], James D. Johnston[1], Geoff Johnston[2], Saija A. Kontulainen[3]
[1] Mechanical Engineering Department, University of Saskatchewan, Saskatoon, SK, Canada
[2] College of Medicine, University of Saskatchewan, Saskatoon, SK, Canada
[3] College of Kinesiology, University of Saskatchewan, Saskatoon, SK, Canada

Introduction

Osteoporosis is a degenerative bone disease where bones undergo a loss in density. This loss of density leads to weakening of the bones, making them more susceptible to fractures.[1] Distal radius fractures (DRF) are the most common form of osteoporotic fracture in women and play an important role in predicting later osteoporotic fractures.[2] Colles' fracture, a type of DRF, typically result from a fall from standing height or less.[3,4] Colles' fractures are important to study because roughly 25% of all bone injuries are Colles' fractures.[5] In Canada in 2010 alone, there were 31 100 osteoporotic wrist fractures.[1] An effective method to diagnose fracture risk is needed in order to reduce the number of DRFs.

Peripheral quantitative computed tomography (pQCT) is a value tool for assessing bone strength.[6] Current models for determining the strength of the radius using pQCT imaging only consider pure compression loading. The forearm is not loaded in pure compression during a fall scenario. The loading pattern is actually an off-axis load which produces a combination of compression and bending moments. When bending is considered in the loading of the radius, the bone is 47% weaker.7

This work seeks to develop a model to estimate overall bone strength using pQCT imaging and mechanical testing that represents a falling scenario.

Methods

Specimens: Twenty cadaveric forearms, with the hand intact, will be scanned using pQCT at 4% of the length of the radius away from the distal end. This is site where Colles' fractures occur. Additionally, the samples will also be scanned using a QCT scanner. The samples will then be potted midshaft and have five tri-axial strain gauges placed at the 4% site. Three placed around the radius and two more placed on the ulna. The ulna has been shown to carry about 17% of the total force through the forearm during axial loading.8-10 The ulna has been neglected previously so this study will consider its effects.

Mechanical Testing: Potted samples will be placed in a material testing system (MTS Bionix) with 15° of dorsal inclination and 3-6° of radial inclination in order to more accurately represent hand positon during a fall. The locations of the strain gauges will be determined using a 3D digitizer, which will be used to precisely locate the strain gauges on the scan images. Failure testing will be performed at 180mm/min in order to attempt to replicate the high rate of loading involved in a fall. Strain, displacement and final failure load will all be recorded during testing.

pQCT Imaging Analysis: Custom Matlab image processing algorithms will be used to model the porous cortical and trabecular bone as pure cortical. The line of action will be determined relative to the centroid in terms of principal axes from the strain data. The distance to the line of action will be used for deriving the applied bending moments resulting from off-axis loading. A model for predicting whole bone failure load will be developed from the equation:

$$Failure\ Load = \frac{Bone\ Strength}{\left[\frac{1}{Area} + \frac{y_{force\ vector} * y_{point\ of\ interest}}{I_x} + \frac{x_{force\ vector} * x_{point\ of\ interest}}{I_y}\right]}$$

where bone strength is the local strength determined from engineering failure theory.

Results & Anticipated Conclusions

This work is currently on going, samples are on hand to begin testing but some equipment is still on order. The strength indices developed will be able to be used in a clinical setting or in research about bone strength to estimate failure load.

References

1.Osteoporosis Canada 2014, 2.Cuddihy et al. 1999, 3.Wagner et al. 2012, 4.Edwards & Troy 2012, 5.Varga et al. 2010, 6.Muller et al. 2003, 7.Troy & Grabiner 2007, 8.Hsu et al. 1993, 9.Trumble et al. 1987, 10.Werner et al. 1992

Does the Treatment of Organophosphate Exposure Cause Physiological Changes in the Brain? An MRI Study

Lee S[1, 2,3,4], Bohnert S[5,6], Dunn JF [1,2,3,4]
[1]Department of Radiology, [2]Hotchkiss Brain Institute, [3]Cumming School of Medicine, [4]University of Calgary,
[5]Defence Research and Development Canada, [6]Department of National Defence

Introduction

Organophosphate (OP) exposure is an ongoing public health concern as they are widely used in agriculture and chemical warfare. Nerve agents (NA) used in chemical warfare are categorized as weapons of mass destruction and include soman, sarin, tabun, and VX [1]. In August of 2013, during the Syrian civil war, sarin gas was released on Syrian civilians [2]. These compounds are potent irreversible inhibitors of acetylcholinesterase (AChE) that causes cholinergic overstimulation. Excess acetylcholine in the neuronal synapse induces glutamate release [3], which has excitotoxic effect by activating a calcium-mediated neuronal necrosis pathway [4]. The treatment for OP poisoning involves oximes, reactivators of AChE, and atropine, which blocks acetylcholine in the muscarinic receptors [5].

It is important to characterize whether treatments themselves produce neuro-pathological effects when administered in the absence of an organophosphate. Oxime HI-6 and atropine methyl nitrate (AMN) will be used. We hypothesize that rats treated with oxime HI-6 and AMN will not show pathophysiology as measured using a combination of MRI and oxygenation measurements.

Methods

Oxygenation: Male adult Sprague-Dawley rats will undergo surgery to implant a fiber-optic pO_2 probe in the hippocampus and cortex. A fluorescent lifetime measurement is used to quantify pO_2 at the tip of the implant using an Oxylite (Oxford Optronics). Values collected are digitized and analyzed using MATLAB. pO_2 will be measured before HI-6 and AMN treatment, 1 hour post treatment and measured daily for 7 days.

Perfusion Imaging: MR images will be obtained using a 35mm volume coil. Continuous arterial spin labeling will be used to collect cerebral blood flow with a 9.4T Bruker animal MRI system using the Bruker Avance II console. The sequence is as follows: matrix dimensions of 128x128 pixels, FOV= 30x30mm, voxel size= 0.23x0.23x1mm, RARE factor of 36, averages of 16, TE= 2.66ms, TR=3000ms.

Results and Conclusion

Measurement of hippocampal and cortical pO_2 will determine if the combined treatment of oxime HI-6 and AMN produces hypoxia. In conjunction with perfusion imaging, which measures cerebral blood flow, we can determine if the treatment method for NA poisoning produces acute changes in physiology. In a future project, we will determine how NA exposure compares to the exposure to NA-treatments.

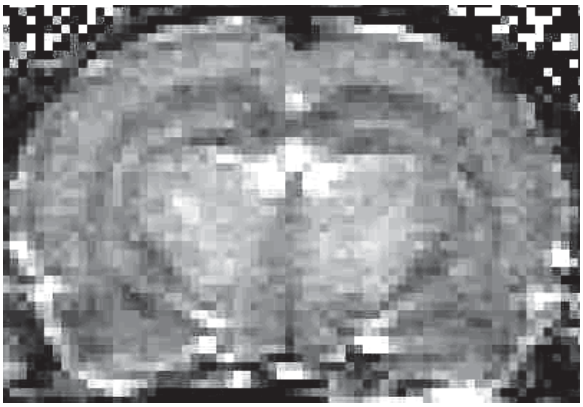

Figure 1. 9.4T MRI perfusion map of a control rat brain.

References

[1] Shih, T. M., S. M. Duniho and J. H. McDonough (2003). Toxicol Appl Pharmacol 188(2): 69-80. **[2]** Dolgin, E. (2013). Nat Med 19(10): 1194-5. **[3]** Collombet, J. M. (2011). Toxicol Appl Pharmacol 255(3): 229-41. **[4]** Fujikawa, D. G. (2015). Comput Struct Biotechnol J 13: 212-221. **[5]** Bajgar, J. (2004). Adv Clin Chem 38: 151-216.

Inertial sensors as a diagnostic tool: Biomedical engineering support of the 2015-16 veterinary independent research project

Ryan Schroeder, John Bertram and John Matyas
HRIC 3C45A - 3280 Hospital Dr. NW, Calgary, AB T2N 4Z6

Introduction

The University of Calgary veterinary school has a tradition of the third year class completing an independent research project (IRP). This year the class is investigating the use of inertial sensors as a diagnostic tool for the gait assessment of canines. Specifically, medium-sized dogs were trained to trot down a trackway composed of force plates (to measure ground reaction forces) and while wearing inertial sensors (to measure body accelerations). The objective of this report is to describe the involvement of biomedical engineering (BME) in helping these clinicians-in-training as they complete this engineering intensive research investigation.

Veterinary medicine has long relied upon clinicians to spot gait pathologies in animals with various subjective measures. However, more subtle issues such as a minor lameness (i.e. limping) can be difficult to assess (Hewetson et al., 2006). As an alternative, a BME approach that relies upon measuring the dynamics of animal locomotion can give a rigorous, quantitative indication of the difference between healthy and pathological gaits.

Methods

During this project, one of the major roles of BME was to help the students understand basic concepts in kinematics, kinetics and locomotion biomechanics. To accomplish this, podcasts were developed as a medium for translating complicated concepts into more palatable real world examples.

Another goal was to introduce the students to important scientific instruments (e.g. force plates, inertial sensors) necessary for measuring relevant gait parameters. To do this, guided exploration sessions were held such that the students were able to interact with the software and hardware directly. This "hands-on" approach has led to an increased comfort and confidence whilst interfacing with the technology.

Results

The utilization of podcasts outlining relatable real world examples was an effective means to allow the students in the IRP to grasp BME concepts including dynamics and locomotion biomechanics. Additionally, these veterinary students have successfully familiarized themselves with the BME tools necessary to perform quantitative gait analysis while utilizing a suite of diverse instruments. Ultimately, this culminated in the verification of a novel instrumentation system (i.e. inertial sensors) as well as the indication of a robust and flexible diagnostic tool for assessing gait pathologies, not only in the lab or the clinic, but in the field as well.

Conclusions

Interdisciplinary research has gained popularity in recent years largely because of its propensity to tackle difficult problems in creative ways (Sharp and Langer, 2011). By combining a BME perspective with the clinical education of veterinary medicine students we have proven an effective collaboration strategy to look at clinical problems in a more rigorous and quantitative way. This project confirms the feasibility of combining multiple disciplines to create a successful research program for graduate level students and should be embraced in other departments and institutions.

References

Hewetson et al. 2006. Investigations of the reliability of observational gait analysis for the assessment of lameness in horses. *VET REC.* 158(25):852-857.

Sharp and Langer. 2011. Promoting Convergence in Biomedical Science. *Science*. Vol. 333:527

Validating finite element strain predictions using high resolution imaging and experimental testing

M. Hosseini[1], M. Nazemi[1], A. Sacher[1], D. Eichhorn[2], S.A. Kontulainen[2, 3], D. Cooper[4], J. Lanovaz[2,3], S.K. Boyd[5], J.D. Johnston[1,2]
1. Department of Mechanical Engineering, University of Saskatchewan, Saskatoon, Canada
2. Division of Biomedical Engineering, University of Saskatchewan, Saskatoon, Canada
3. College of Kinesiology, University of Saskatchewan, Saskatoon, Canada
4. Department of Anatomy and Cell Biology, University of Saskatchewan, Saskatoon, Canada
5. Department of Radiology, University of Calgary, Calgary, Canada

Introduction: Osteoarthritis (OA) is a degenerative joint disease affecting 10% of Canadians; roughly half exhibiting knee OA [1]. The disease is marked by morphological and mechanical changes to bone which are thought to distort joint mechanics and accelerate cartilage degeneration [2, 3]. Trabecular bone, in particular, is believed to play an important role mediating overall mechanical behaviour, pain initiation and potentially OA development [4, 5].

Subject-specific finite element (FE) modeling has potential to improve our understanding of the role of bone with OA. Quantitative computed tomography (QCT) is commonly used to provide both bone geometry and material properties for FE models (known as QCT-FE). A basic step with QCT-FE is to assign material properties (elastic modulus, E) based upon imaged density (typically via density-modulus relationships). However, it is unclear what equation(s) should be used for modeling cortical and trabecular bone of the knee. Earlier work completed by our research group identified density-modulus relationships which best predicted proximal tibial structural stiffness [6], but it is unclear if the developed model accurately reflects both peripheral surface strain and internal strain distributions within the tibia and femur.

The overall objective of this research is to advance the developed FE-model to predict surface and internal bone strain.

Methods: This research will consist of three main studies: (1) internal strain validation via a novel testing system integrating compressive testing with simultaneous high resolution imaging; (2) surface strain validation during compressive mechanical testing; and (3) surface strain validation during dynamic loading simulating knee flexion/extension.

Specimens: Fifteen cadaveric knee joints will be acquired from the UofS College of Medicine. The joints will be potted (fixated) in PMMA with ~25% of exposed proximal tibia and distal femur.

Finite Element Modeling: Knees will be imaged using (QCT) (0.5mm voxel size) and converted to FE models using established procedures [6].

Internal Strain Validation: Knee joints will be set in a custom material testing system comprised of a high precision actuator (Zwick) and frame made of radiolucent acrylic [7] situated within a high resolution peripheral QCT (HR-pQCT) scanner. Incrementally increasing compressive loads will be applied to the knee joint and HR-pQCT imaging (41μm voxel size) will be performed after the load has relaxed. Digital volume correlation (DVC) [8] will then be applied to incrementally acquired images to calculate internal strain/displacement distributions occurring throughout the proximal tibia, expressed as a function of applied load. Acquired DVC strain/displacement data will then be used to validate FE-derived internal strain/displacement.

Surface Strain Validation – Static Loading: Tri-axial strain gauges will be affixed to the surfaces of the tibia and femur. Knee joints will be placed within a material testing system (MTS) and undergo static compressive loading. Static surface strain data will be used to validate FE-derived surface strain.

Surface Strain Validation – Dynamic Loading: Strain gauged knee joints will be placed within an Oxford Rig Knee Simulator. Knee joints will be subjected to dynamic mechanical loading simulating knee flexion/extension. A motion tracking system (PTI) will track tibia and femur 3D positions, with FE models reconstructed to mimic dynamic positions (e.g., 0//45//90° flexion). Dynamic surface strain data will be used to validate FE-derived surface strain.

Results to date: The research is currently ongoing. Testing apparatuses have been constructed and methodologies are currently being established.

Anticipated Conclusions: Validated FE models can be used to gain information regarding the mechanical role of bone alterations in joint degeneration and pain initiation. These techniques, and related knowledge, can provide bases for developing new *in vivo* diagnostic tools for early joint disease detection. As well, validated FE models have important applications in knee arthroplasty design.

References

[1] Health Canada, 2003 [2] Radin 1972 [3] Radin et al., 1986 [4] Burnett et al., 2015 [5] Amini et al., 2015 [6] Nazemi et al., 2015 [7] Sacher et al., 2015 [8] Bar-Kochba et al., 2014

Enhanced Chondrogenic Phenotype of Tissue Engineered Cartilage Constructs Generated in Stirred Suspension Bioreactors

Leah M. Allen, David A. Hart, Arindom Sen
PPRF, BI-514, University of Calgary, 2500 University Drive NW, Calgary AB, T2N 1N4

Introduction

Traumatic injuries to articulating joints such as the knee can result in the formation of defects within the articular cartilage contained therein. These defects can initiate a degenerative process, eventually resulting in osteoarthritis (OA). Current cartilage repair options are limited and do not result in the regeneration of durable cartilage[1]. Mesenchymal stem cells (MSCs) isolated from the lubricating fluid within joints, have an inherent ability to form cartilage. When placed in large numbers into small, static tissue culture vessels, MSCs can be manipulated to aggregate and form pliable, three-dimensional tissue engineered cartilage constructs (TECCs)[2,3]. TECCs implanted into a defect site have been shown to contribute to cartilage repair in animal models[2,4], thereby illustrating a potential new approach to prevent the onset or the progression of OA. The bioprocess used to generate TECCs needs to be further optimized to improve TECC uniformity and enhance their chondrogenic capacity. Scalable suspension bioreactors provide an alternative platform to facilitate the production of uniform populations of MSC based TECCs. Here the impact of adding growth modulators (TGF-Beta, BMP-2, ascorbic acid, dexamethasone) and maintaining a low-oxygen environment was investigated to assess enhancement of the chondrogenic phenotype of TECCs in bioreactors.

Methods

Human synovial fluid (SF)-derived MSCs were isolated and inoculated into suspension bioreactors under serum-free conditions. In efforts to enhance the chondrogenic phenotype of the TECCs, 3% oxygen tension was employed and compared to 21% oxygen tension. Additionally, the TECCs were treated with TGF-Beta, BMP-2, ascorbic acid and dexamethasone in a suspension environment. TECCs resulting from the suspension culture methods were analyzed for cell proliferation, size distribution and extracellular matrix (ECM) deposition (as evaluated by histochemistry). The surface architecture of the TECCs was visualized using scanning electron microscopy. Regulation of chondrogenic genes was investigated using RT-qPCR.

Results

Production of TECCs under a 3% and 21% oxygen tension showed similar TECC formation and growth of MSCs. Conversely, the low oxygen environment led to increases in overall size of the TECCs formed (see figure) and slightly enhanced their chondrogenic phenotype. Subsequent treatment with TGF-Beta, BMP-2, ascorbic acid and dexamethasone also up-regulated the cartilage characteristics of TECCs.

Conclusions

The production and cartilage-like characteristics of TECCs can be enhanced when generated from SF-derived MSCs in suspension bioreactors under a low oxygen environment and supplementing with growth modulators.

References

1. Matsiko, A. *et al*. *Materials.* **6,** 637–668 (2013)
2. Ando, W. *et al. Biomaterials* **28,** 5462–70 (2007)
3. Ando, W. *et al. TissEng. Part A* **14,** 2041–9 (2008)
4. Ando, W. *et al. Eur. Cell. Mater.* **24,** 292–307 (2012).

Figures

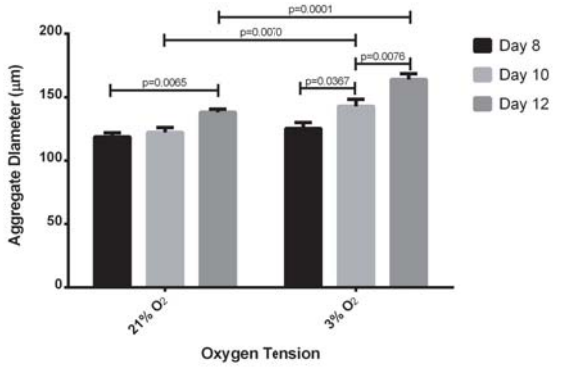

Bench-Testing a Novel Surgical Implant to Stabilize Distal Radial Fractures

Nima Ashjaee[1], Saija A. Kontulainen[2], Geoff Johnston[3], James D. Johnston[1]
[1] Mechanical Engineering Department, University of Saskatchewan, Saskatoon, SK, Canada
[2] College of Kinesiology, University of Saskatchewan, Saskatoon, SK, Canada
[3] College of Medicine, University of Saskatchewan, Saskatoon, SK, Canada

Introduction:

Distal radial fractures are common, especially in older women (~70,000 cases annually in Canada [1]). Unfortunately, surgical outcomes do not re-establish normality. There is a need for an implant which maintains the corrected position (reduction) of the fracture, minimizes soft tissue disruption for its insertion, does not interfere with the natural fracture healing process, does not necessitate hospitalization of the patient nor access to operating room facilities, and which is technically easy to perform.

The objective of this research is to bench-test a novel surgical implant designed to stabilize distal radial fractures and to confirm that it has potential for use in clinical practice.

Methods:

Overview: The novel implant and a "gold-standard" titanium volar locking plate will be applied to cadaveric distal radial fractures, and evaluated in a laboratory setting using mechanical testing and high resolution peripheral quantitative compound tomography (HR-pQCT) imaging.

Specimens: Ten pairs of left:right radius specimens (20 total radii) derived from older female cadavers will be used for the experiment.

Sample preparation: A "worst case" fracture scenario will be simulated by removing a wedge of material from the dorsal (back) side of the distal radius (~10mm wide, centered ~20mm proximal to the tip of the radial styloid). . This simulated fracture neutralizes the load carrying capacity of the cortex and has been widely used in the literature [2-4].

Surgical Approach: The novel implant design and a titanium volar locking plate will be applied according to recommended surgical practices in order to "reduce" the fracture gap. Left/right radii will be randomly separated into either group.

Simulated Loading: The proximal and distal ends of the radii would be fixed (potted) and positioned in a material testing system (MTS 858 Bionix). Each specimen will undergo bending and axial loading simulating a fall onto the outstretched hand. Loading will be applied in a dynamic cyclic manner, with ramped loading (e.g., 0-100N for 10,000 cycles, 0-200N for next 10,000 cycles, etc.), to evaluate mechanical stability. The primary outcome will be stiffness as a function of number of cycles.

Imaging: In order control for potential side-to-side differences (e.g., differing density or morphology between left:right radii), each radii will undergo HR-pQCT imaging prior to mechanical testing [5]. Imaging metrics will be used as potential covariates in the statistical analysis.

Statistical Analysis: The mechanical stability of the system will be assessed by comparing the stiffness of the novel implant with "gold-standard" locking plate using analysis of covariance. Cortical bone thickness and density, measured using HR-pQCT imaging, will be used as potential covariates. A p-value less than 0.05 will be considered significant.

Results to date: The research is currently ongoing. Testing apparatuses are being constructed and methodologies are currently being established.

Anticipated Conclusions: This study has the potential to alter the management of distal radius fractures. This information will be valuable to patients, physicians and orthopaedic surgeons, healthcare systems planners, pharmaceutical companies and patient advocacy groups. As well, the anticipated per case cost of this new technology is ~80-90% less than current costs, a marked savings to the healthcare system.

References

[1] C. M. Court-Brown and B. Caesar, "Epidemiology of adult fractures: a review," *Injury,* vol. 37, pp. 691-697, 2006.
[2] R. J. van Kampen*, et al.*, "Comparison of a new intramedullary scaffold to volar plating for treatment of distal radius fractures," *Journal of orthopaedic trauma,* vol. 27, pp. 535-541, 2013.
[3] F. A. Liporace*, et al.*, "A biomechanical comparison of a dorsal 3.5-mm T-plate and a volar fixed-angle plate in a model of dorsally unstable distal radius fractures," *Journal of orthopaedic trauma,* vol. 19, pp. 187-191, 2005.
[4] A. A. Willis*, et al.*, "Internal fixation of dorsally displaced fractures of the distal part of the radius," *The Journal of Bone & Joint Surgery,* vol. 88, pp. 2411-2417, 2006.
[5] E. Hildebrandt*, et al.*, "What is the bilateral asymmetry of radius and tibia bone microarchitecture by HR-pQCT?," in *JOURNAL OF BONE AND MINERAL RESEARCH*, 2014, pp. S220-S220.

Controlled release of dexamethasone from in situ forming sulfobutyl ether β-cyclodextrin/self-assembling peptide hydrogel

Lei Lu, Larry D. Unsworth*
Department of Chemical and Materials Engineering, University of Alberta, Edmonton, Alberta, T6G 2V4, Canada

Introduction

The self-assembling peptide $(RADA)_4$ is capable of forming bioactive scaffolds in situ for different biomedical applications [1]. However, a universal way to control the delivery small hydrophobic drugs (ie. anti-inflammatory, anti-cancer, anti-bacterial drugs etc.) while maintaining a hydrogel structure is rarely reported. Cyclodextrins (CDs) have a relatively nonpolar cavity and a hydrophilic exterior, and have been used for solubilizing hydrophobic drugs in pharmaceutical applications for many years. Sulfobutyl ether β-cyclodextrin (SBE-β-CD; Captisol®) is a derivatized form of β-cyclodextrin with a range of six to seven sulfobutyl ether groups [2]. In this work, the influence of SBE-β-CD on $(RADA)_4$ peptide nanofiber conformation and the thermodynamic interactions between each molecule have been determined. A new strategy of using anionic SBE-β-CD as carrier to load hydrophobic drug in the peptide self-assembly nanofiber system is investigated.

Methods

The influence of SBE-β-CD on peptide's secondary structure and hydrogel formation was evaluated by AFM, circular dichroism (CD) and zeta potential analyzer. The binding affinities between model drug Dexamethasone (Dex), SBE-β-CD, and $(RADA)_4$ was characterized using isothermal titration calorimetry (ITC). In vitro release of Dex from SBE-β-CD/$(RADA)_4$ hydrogel was measure using UV-Vis.

Results

The ionic interaction between SBE-β-CD and $(RADA)_4$ peptide dramatically affects the nanofiber formation and subsequent gel stability; where gel stability is related to the SBE-β-CD/$(RADA)_4$ ratio. Excessive amounts of SBE-β-CD seem to reduce the β-sheet formation of peptide, resulting in a white precipitation instead of transparent hydrogel. The ITC results suggest that the dissociation of SBE-β-CD/Dex inclusion complexes dominate the overall release rate. The different concentration of SBE-β-CD and $(RADA)_4$ peptide significantly affect the release kinetics. Generally, higher concentration of both SBE-β-CD and $(RADA)_4$ peptide is supposed to perform a slower release of drug. This observed phenomenon may related to the nanofiber cross-linking structure.

Conclusions

This work discussed the basis of the SBE-β-CD/self-assembling peptide based in situ hydrogel and leading to application prospects of other hydrophobic drugs delivery, such as anti-cancer or anti-infection therapies.

References

[1] Gelain F, Horii A, Zhang SG. Designer self-assembling peptide scaffolds for 3-D tissue cell cultures and regenerative medicine. Macromol Biosci 2007;7:544-51.

[2] Lockwood SF, O'Malley S, Mosher GL. Improved aqueous solubility of crystalline astaxanthin (3,3 '-dihydroxy-beta,beta-carotene-4,4 '-dione) by Captisol (R) (sulfobutyl ether beta-cyclodextrin). J Pharm Sci-Us 2003;92:922-6.

Figures

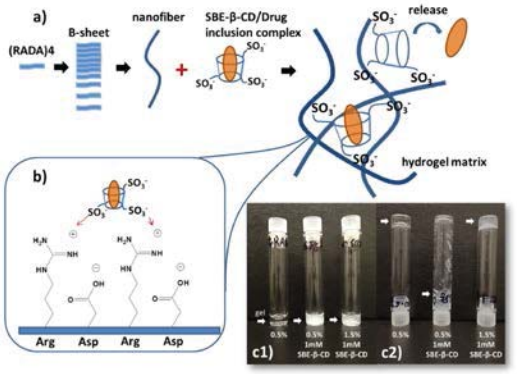

Figure 1. a) Schematic of the self-assembly formation process of the hydrogel matrix. b) The length of the arginine residues and aspartic acid residues are different, which make the electrostatic interaction between SBE-β-CD and nanofiber surface possible. c1) After gelation, pure 0.5% w/v $(RADA)_4$ was still clear (left), however, 0.5% w/v $(RADA)_4$ with 1 mM final concentration of SBE-β-CD was changed into white precipitate (middle), while the same concentration of SBE-β-CD with 1.5% w/v $(RADA)_4$ yields a gel (right). c2). Inverted vials, 0.5% w/v $(RADA)_4$ with 1 mM SBE-β-CD sample (middle) was unable to form a strong gel. The white arrows point to gel positions.

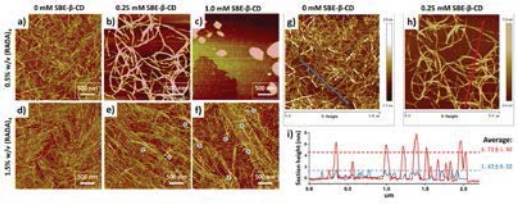

Figure 2. AFM images of hydrogels with 500 times dilution. The hydrogels were made by mixing $(RADA)_4$ peptide with different SBE-β-CD at various ratios ((RADA)4: 0.5 % or 1.5 % w/v; SBE-β-CD: 0. 0.25 and 1.0 mM; a-f); The examples of section height analysis of pure 0.5% w/v $(RADA)_4$ (g, blue arrow) and 0.5% w/v $(RADA)_4$ with 0.25 mM SBE-β-CD (h, red arrow). The section heights difference was shown in i), the average height of nanofibers were collected and analyzed from >50 random points of each sample.